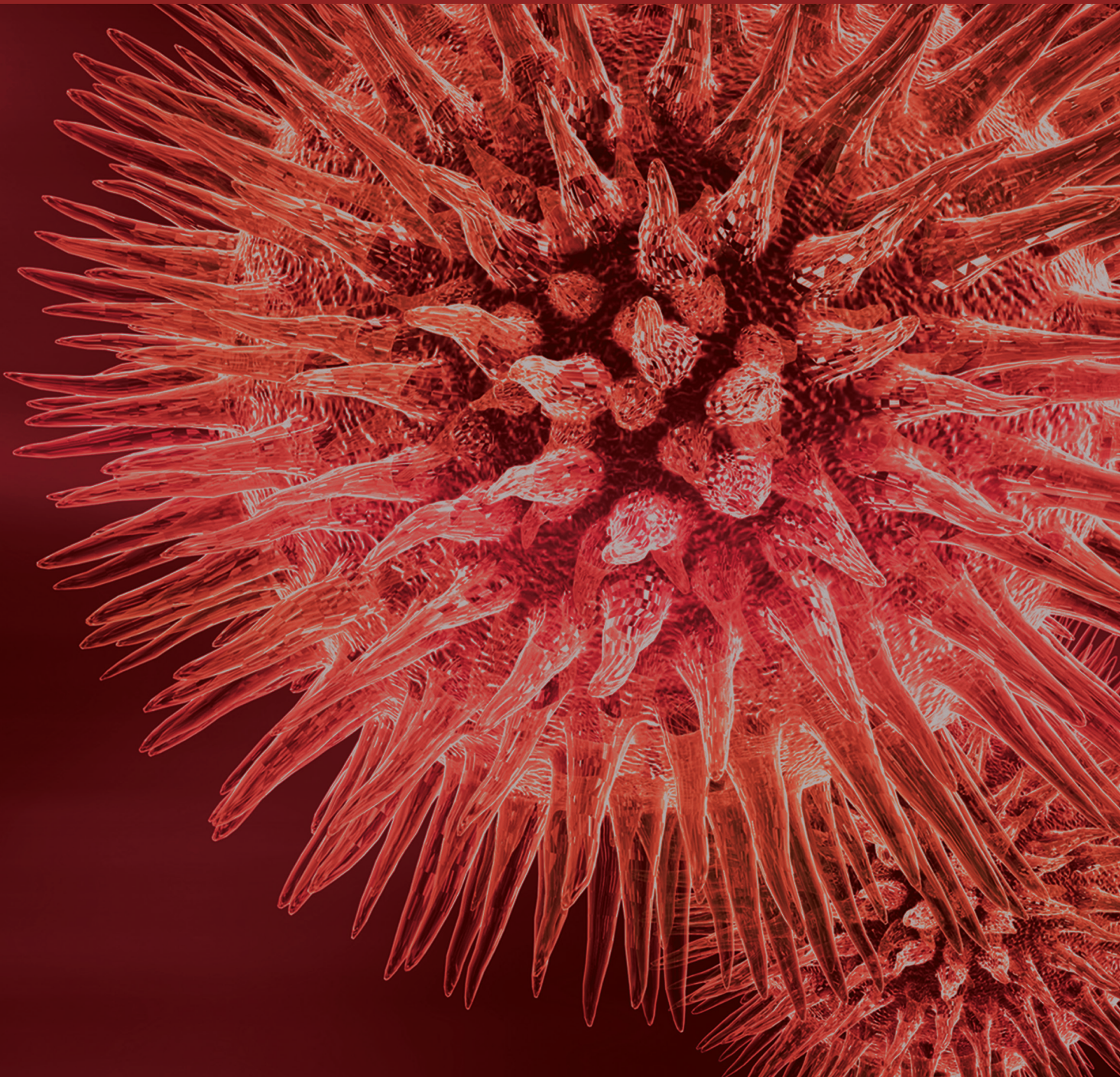


BioMed Research International

Fluorescent Probes for Biological Imaging

Guest Editors: Xuanjun Zhang, Yupeng Tian, Jiangbo Yu, and Zhen Yuan





Fluorescent Probes for Biological Imaging

BioMed Research International

Fluorescent Probes for Biological Imaging

Guest Editors: Xuanjun Zhang, Yupeng Tian, Jiangbo Yu,
and Zhen Yuan



Copyright © 2016 Hindawi Publishing Corporation. All rights reserved.

This is a special issue published in “BioMed Research International.” All articles are open access articles distributed under the Creative Commons Attribution License, which permits unrestricted use, distribution, and reproduction in any medium, provided the original work is properly cited.

Contents

Fluorescent Probes for Biological Imaging

Xuanjun Zhang, Yupeng Tian, Jiangbo Yu, and Zhen Yuan
Volume 2016, Article ID 3730486, 1 page

Sandwich Immunoassays of Multicomponent Subtrace Pathogenic DNA Based on Magnetic Fluorescent Encoded Nanoparticles

Yaxu Liu, Xuanjun Zhang, Yifeng E, Fang Fang, Guangkai Kuang, and Guannan Wang
Volume 2016, Article ID 7324384, 9 pages

MP Resulting in Autophagic Cell Death of Microglia through Zinc Changes against Spinal Cord Injury

Dingding Li, Guannan Wang, Donghe Han, Jing Bi, Chenyuan Li,
Hongyu Wang, Zhiyuan Liu, Wei Gao, Kai Gao, Tianchen Yao,
Zhanghui Wan, Haihong Li, and Xifan Mei
Volume 2016, Article ID 6090316, 14 pages

Nanoparticle Probes for Structural and Functional Photoacoustic Molecular Tomography

Haobin Chen, Zhen Yuan, and Changfeng Wu
Volume 2015, Article ID 757101, 11 pages

A Series of Imidazole Derivatives: Synthesis, Two-Photon Absorption, and Application for Bioimaging

Yingzhong Zhu, Lufei Xiao, Meng Zhao, Jiazheng Zhou, Qiong Zhang, Hui Wang, Shengli Li,
Hongping Zhou, Jieying Wu, and Yupeng Tian
Volume 2015, Article ID 965386, 8 pages

Development of the 1.2 T~1.5 T Permanent Magnetic Resonance Imaging Device and Its Application for Mouse Imaging

Guangxin Wang, Huantong Xie, Shulian Hou, Wei Chen, Qiang Zhao, and Shiyu Li
Volume 2015, Article ID 858694, 8 pages

Expression of HE4 in Endometrial Cancer and Its Clinical Significance

Xiao Li, Yiping Gao, Mingzi Tan, Huiyu Zhuang, Jian Gao, Zhenhua Hu, Huimin Wang, Liancheng Zhu,
Juanjuan Liu, and Bei Lin
Volume 2015, Article ID 437468, 8 pages

Neuroprotective Effect of Simvastatin via Inducing the Autophagy on Spinal Cord Injury in the Rat Model

Kai Gao, Guannan Wang, Yansong Wang, Donghe Han, Jing Bi, Yajiang Yuan, Tianchen Yao, Zhanghui Wan,
Haihong Li, and Xifan Mei
Volume 2015, Article ID 260161, 9 pages

A Pyrene@Micelle Sensor for Fluorescent Oxygen Sensing

Yan-xia Yuan, Hong-shang Peng, Jian-tao Ping, Xiao-hui Wang, and Fang-tian You
Volume 2015, Article ID 245031, 6 pages

Editorial

Fluorescent Probes for Biological Imaging

Xuanjun Zhang,¹ Yupeng Tian,² Jiangbo Yu,³ and Zhen Yuan¹

¹*Faculty of Health Sciences, University of Macau, Taipa, Macau*

²*Department of Chemistry, Anhui University, Hefei 230601, China*

³*Department of Chemistry, University of Washington, Seattle, WA 98195-1700, USA*

Correspondence should be addressed to Xuanjun Zhang; xuanjunzhang@umac.mo

Received 16 September 2015; Accepted 16 September 2015

Copyright © 2016 Xuanjun Zhang et al. This is an open access article distributed under the Creative Commons Attribution License, which permits unrestricted use, distribution, and reproduction in any medium, provided the original work is properly cited.

Owing to the high sensitivity, high resolution, and the wealth of contrast mechanisms, fluorescence imaging is the most versatile and widely used visualization modality to study the structure and function of biological systems and the molecular process in living organisms without perturbing them.

Fluorescence molecular imaging is an evolving field of imaging sciences, which involves the development of microscopic techniques for live cell imaging at super resolution and macroscopic techniques to monitor molecular events in living organism. The breakthrough of super-resolution techniques allows researchers to obtain fluorescence images with a higher resolution than the diffraction limit. On the other hand, fluorescence imaging is also facing important challenges. Because the imaging requires exogenous probes to enhance imaging contrast or provide signal readout, the probe performance largely determines the detection limit and sensitivity. The intrinsic poor penetration of UV and visible light limits their broad applications in biology. Therefore, promising probes that exhibit high photostability, long fluorescence lifetime, strong absorption, and/or emission in the near-infrared (NIR) region are highly desirable.

Nanoparticle is a collection of atoms or molecules with much higher intensity of absorbance and emissions compared to small molecular probes, which can provide strong local contrast in biological imaging. Two-photon fluorescent probe simultaneously absorbs two infrared (IR) or NIR photons. Using IR or NIR light as excitation can minimize the light scattering and suppress the background signal, which allows imaging of living tissue up to about one millimetre in depth.

Applications of fluorescent probes for fluorescence molecular imaging are growing quickly for recording events from single live cells to whole animals with high sensitivity and accurate quantification. Such approaches have immense potential to track progression of metastasis, immune cell trafficking, stem cell therapy, transgenic animals, and even molecular interactions in living subjects, which represent the future and trends of optical molecular imaging technologies.

This special issue compiles several selected original and overview articles that range from design of contrast agents including fluorescent molecules and nanoparticles to biomedical molecular imaging and sensing with various applications. The editors believe that the selected work presented in this issue may provide useful information and promote further investigations on the development of novel fluorescent probes to be used for diagnosis and treatment of disorders and diseases as well as understanding the biological processes.

Acknowledgments

The editors take this opportunity to thank the authors for their contribution to this special issue. They are also grateful to Editorial Board members and reviewers for their great support and cooperation.

*Xuanjun Zhang
Yupeng Tian
Jiangbo Yu
Zhen Yuan*

Research Article

Sandwich Immunoassays of Multicomponent Substrate Pathogenic DNA Based on Magnetic Fluorescent Encoded Nanoparticles

Yaxu Liu,¹ Xuanjun Zhang,² Yifeng E,¹ Fang Fang,¹ Guangkai Kuang,¹ and Guannan Wang¹

¹Department of Chemistry, College of Pharmacy, Liaoning Medical University, Jinzhou 121001, China

²Faculty of Health Sciences, University of Macau, Avenida da Universidade, Taipa, Macau

Correspondence should be addressed to Guannan Wang; chemwangguannan@gmail.com

Received 15 December 2014; Accepted 6 January 2015

Academic Editor: Jinsong Ren

Copyright © 2016 Yaxu Liu et al. This is an open access article distributed under the Creative Commons Attribution License, which permits unrestricted use, distribution, and reproduction in any medium, provided the original work is properly cited.

A novel magnetic fluorescent encoded nanoimmunoassay system for multicomponent detection and separation of the substrate pathogenic DNA (hepatitis B virus surface gene, HBV; hepatitis A virus poly the protein gene, HAV) was established based on new type of magnetic fluorescent encoded nanoparticles and sandwich immunoassay principle. This method combines multifunctional nanoparticles, immunoassay technique, fluorescence labeling, and magnetic separation of multicomponent technology. It has many advantages such as high sensitivity, low detection limit, easy operation, and great potential for development. The results of this work show that, based on nanoimmunoassay system, it could quantitatively detect the multicomponent trace pathogenic HAV and HBV DNA, as well as detection limit up to 0.1 pM and 0.12 pM. Furthermore, with the improvement of the performances of magnetic fluorescent encoded nanoparticles, the sensitivity will be further improved. In this experiment, a new nanoimmunoassay system based on magnetic fluorescent encoded nanoparticles was established, which will provide a new way for the immunoassay and separation of multicomponent biomolecules.

1. Introduction

In recent years, multivariate analysis and separation technology, analysis and separation of multicomponent biological molecular in a single sample, has been a major research for detection of gene expression in genetic and infectious disease [1], drug recognition [2], environmental monitoring [3], and food safety detection [4]. With the development of nanomaterials and nanotechnology, the research and application of multifunctional nanomaterials have attracted considerable attention in multivariate analysis [5–7]. Superparamagnetic nanoparticles, especially Fe₃O₄ nanoparticles, have played a pivotal role among MRI, biomagnetic separation, targeted drug delivery, magnetic hyperthermia, and immobilized enzyme due to their excellent physical properties and biological applications [8–11]. Quantum dots (QDs) have been widely applied to the research of fluorescent hybridization analysis, cell imaging, and living tracking as an outstanding

fluorescent indicator due to their superior properties, such as special optical property, high photostability, and size-tunable light emission [12–16].

Magnetic fluorescent encoded nanoparticles are a kind of novel multifunctional nanoparticle with magnetic and fluorescent encoding properties, being the attractive nanomaterial in multivariate analysis and separation technology due to its excellent characteristics, such as the integration of the advantages of magnetism and fluorescent encoding, multicomponent labeling, and targeted separation [17–20]. Recently, the design, synthesis, functionalization, and application of magnetic fluorescent encoded nanoparticles have attracted much attention. However, the fabrication of this system is complex and rarely reported due to the interaction of various nanoparticles in one final nanoparticle [21–24]; particularly, as far as we know, there are very few reports about the combination of magnetic fluorescent encoded nanoparticles and sandwich immunoassay.

In this work, we prepared magnetic fluorescent encoded nanoparticles based on superparamagnetic Fe₃O₄ nanoparticles and two quantum dots with different emission wavelength by reverse microemulsion method. And then, magnetic fluorescent encoded nanoimmunoassay system was established by combination of the nanoparticles and sandwich immunoassay for multicomponent biological assay and separation. In this work, the subtrace hepatitis B virus surface antigen gene (HBV) and hepatitis A virus Vall7 polyprotein gene (HAV) as pathogenic DNA were successfully detected and separated, respectively. The results show that this new magnetic fluorescent encoded nanoimmunoassay system can be generally used to multicomponent biological immunoassay and separation of other biomolecules based on its high sensitivity, lower cost, easy operation, and time saving.

2. Experimental

2.1. Materials and Instrumentation. Cyclohexane, Triton X-100, *n*-hexanol, acetone, ethanol, cadmium chloride (CdCl₂), sodium borohydride (NaBH₄), iron (III) chloride hexahydrate (FeCl₃·6H₂O), and iron (II) chloride tetrahydrate were purchased from Tianjin Chemical Reagents Factory (China). Tellurium (reagent powder), mercaptosuccinic acid, tetramethylammonium hydroxide (TMA, 25%), tetraethoxysilane (TEOS), 3-aminopropyltrimethoxysilane (APS), poly(diallyldimethylammonium chloride) (PDDA, *M_w* = 70000 g/mol), and 3-(trihydroxysilyl)-propyl methylphosphonate (THPMP) were supplied by Sigma-Aldrich Co., Ltd. (United States). All chemicals were used of analytical reagent grade, and the water used in this study was redistilled water.

The targeted DNA was designed from hepatitis B surface antigen gene (HBV) and hepatitis A virus Vall7 polyprotein gene (HAV). The single-stranded DNA (freeze-dried powder) about HBV was provided by TaKaRa Biotechnology Co., Ltd. (Dalian, China). The base sequences of single-stranded DNA were as follows:

HBV:

Capture DNA: 3'-AACCGAAAGTCAATA-5'.
Target DNA: 5'-TTGGCTTTCAGTTAT-ATGGATGATGTGGTA-3'.
Complement DNA: 3'-TACCTACTACAC-CAT-FITC-5'.

HAV:

Capture DNA: 3'-AATCTCAACGTACCT-5'.
Target DNA: 5'-TTAGAGTTGCATGGA-TTAACTCCTCTTTCT-3'.
Complement DNA: 3'-AATTGAGGAGAA-AGA-FITC-5'.

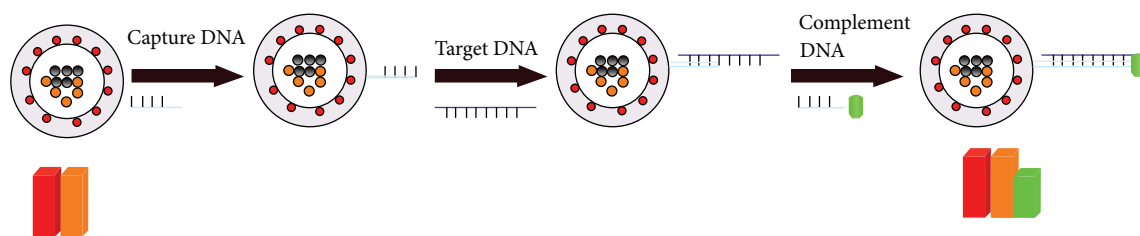
Additionally, wash buffer (WB, 10 mM Tris-HCl, pH 7, 1 mM EDTA), binding buffer (BB, 10 mM Tris-HCl, pH 7, 1.0 M NaCl, 2 mM EDTA), and PBS buffer solution (PH = 7.4) were fabricated by our laboratory.

The fluorescence spectra were recorded with a fluorescence spectrophotometer (RF-5301, Shimadzu Co., Japan). The UV-vis absorption spectra were measured by a UV-vis spectrometer (GBC Cintra 10e, Varian Co., United States). The composite nanoparticles were dispersed by a bath ultrasonic cleaner (Autoscience AS 3120, Tianjin, China). The microscopic structures were obtained using a transmission electron microscope (TEM) (JEOL-1230, Japan). The magnetic hysteresis loops were performed on a vibrating sample magnetometer (VSM) (Nanjing Nanda Instrument Plant, China). The zeta potential and dynamic light scattering (DLS) size distribution was characterized by a Malvern Zetasizer ZEN 3600. All optical measurements were carried out at room temperature under ambient conditions.

2.2. Preparation of Amino-Modified Magnetic Fluorescent Composite Nanoparticles. Stable water compatible CdTe quantum dots (QDs) and superparamagnetic Fe₃O₄ nanoparticles were synthesized as described in our previous work [25, 26]. The CdTe QDs with emission maximum at 573 nm were QDs₁ (average diameter 3.7 nm), and CdTe QDs with emission maximum at 653 nm were QDs₂ (average diameter 4.3 nm), and the concentration was 2×10^{-3} mol/L. Superparamagnetic Fe₃O₄ nanoparticles were synthesized by chemical coprecipitation method, and the harvested concentrations, diameter, and saturation magnetization value of nanoparticles were 10 mmol/L, 7–12 nm, and 60 emu/g, respectively.

QDs₁-Fe₃O₄/SiO₂ composite nanoparticles were synthesized by reverse microemulsion method at room temperature. At first, 7.5 mL cyclohexane, 1.77 mL Triton X-100, 1.8 mL *n*-hexanol, 60 μL PDDA solution (0.075% v/v), and 100 μL TEOS were added in a flask including 100 μL Fe₃O₄ nanoparticles and 400 μL CdTe QDs₁; after stirring for 0.5 h, a uniform microemulsion system was formed. Subsequently, 60 μL NH₄OH (28% v/v) was added to the microemulsion system to initiate TEOS hydrolysis in the dark at room temperature. After reaction for 24 h, 20 μL APS and 40 μL THPMP were added to the system; the reaction system was kept under stirring for 24 h at room temperature. Next, 20 mL of acetone was added in the flask to break the microemulsion system, and the resultant mixture was amino-modified magnetic fluorescent nanospheres (QDs₁-Fe₃O₄/SiO₂ composite nanoparticles) which was separated by a magnet and washed three times in sequence with ethanol and water, respectively. Ultimately, QDs₁-Fe₃O₄/SiO₂ composite nanoparticles were diluted in 5 mL water, and the harvested concentration of the composite nanoparticles was 2.2 mg/mL.

2.3. Synthesized Amino Functional Magnetic Fluorescent Encoded Nanoparticles (AFMFEM). The preparation of AFMFEM was according to our previous work [27]. 7.5 mL cyclohexane, 1.8 mL *n*-hexanol, 1.77 mL Triton X-100, a certain proportion QDs₁ solution, and the as-synthesized amino-modified QDs₁-Fe₃O₄/SiO₂ solution were added in a 50 mL flask including 100 μL TEOS; after stirring for 30 min, the microemulsion system was formed. Then, 120 μL NH₃·H₂O (28% v/v) was added into the flask, and after stirring for 24 h, 30 μL APS and 60 μL THPMP were added to the system. After stirring for 24 h, 20 mL of acetone was



SCHEME 1: Scheme for sandwich immunoassay determination of DNA based on magnetic fluorescent encoded nanoparticles.

added into the flask to break the microemulsion system, and the stirring was terminated when a great deal of precipitation was formed. A magnet was used to separate the product which was washed successively three times with ethanol and water. Finally, the final product was AFMFEM which was diluted in 5 mL deionized water, and the harvested concentration of AFMFEM was 3.6 mg/mL.

According to the requirement of this work, two types of the AFMFEM, with fluorescent encoded $I_{560\text{ nm}} : I_{650\text{ nm}} = 2:1$ and $I_{560\text{ nm}} : I_{650\text{ nm}} = 4:5$, were chosen as models of AFMFEM-1 and AFMFEM-2 for following works.

2.4. Preparation of Capture DNA-Modified Magnetic Fluorescent Encoded Nanoprobes. The capture DNA-AFMFEM was fabricated by electrostatic adsorption of amino functional magnetic fluorescent encoded nanoparticles and capture DNA. Capture DNA and AFMFEM were combined by the electrostatic adsorption principle because of positive charges on the surface of AFMFEM and negative charges on the framework of single-stranded DNA. First, 100 μL AFMFEM (3.6 mg/mL) was washed with wash buffer (WB, 10 mM Tris-HCl, pH 7, 1 mM EDTA) and distributed in 500 μL WB solution. Then, different volumes of capture DNA (200 nM/L) were added, respectively, to the equal AFMFEM solutions, and the mixture solution was diluted to 1 mL. The mixture solution was shaken for 60 min at room temperature, and the final product was capture DNA-AFMFEM which was separated by a magnet. The capture DNA-AFMFEM were washed repetitively with WB solution and were dispersed in 100 μL PBS solution.

Two types of magnetic fluorescent encoded nanoprobes were synthesized as models of AFMFEM-1-HAV capture DNA and AFMFEM-2-HAV capture DNA via the above method.

2.5. Fabrication of Hybrid Compound Using Sandwich Hybridization Analysis. In order to determine unlabeled HAV Target DNA and HBV Target DNA, the sandwich hybridization analysis was used in this work, as schematically outlined in Scheme 1. 50 μL capture DNA-AFMFEM nanoprobes were mixed with equal, various volumes of Target DNA and FITC-Complement DNA, and BB solution was added to the system. The mixture solution was stirred slowly at room temperature to promote the hybridization process of capture DNA and Complement DNA with Target DNA. After stirring for 2 h, the composite was separated by a magnet. The product was washed two times with WB

solution and was dispersed in 1 mL PBS buffer solution. Finally, fluorescence image of the product was measured.

Two types of hybrid composite were fabricated as models of AFMFEM-1-HAV capture DNA/HAV Target DNA/HAV FITC-Complement DNA and AFMFEM-2-HBV capture DNA/HBV Target DNA/HBV FITC-Complement DNA via the above method.

3. Results and Discussion

3.1. Characterization of AFMFEM. In order to avoid the spectra overlap, in this work, orange QDs₁ (emission maximum at 573 nm) and red QDs₂ (emission maximum at 653 nm) were chosen to fabricate magnetic fluorescent encoded nanoparticles. Figure 1(a) shows the emission spectra obtained from QDs and two types of AFMFEM, and the insert is fluorescence spectra of two types of QDs. It can be seen that two types of AFMFEM have clear fluorescent encoding and high fluorescence intensity owing to using different amount of QDs₁-Fe₃O₄/SiO₂ and QDs₂, which are the good candidates as fluorescent probe. Figure 1(b) shows the hysteresis loop of two types of AFMFEM at room temperature, and it can be seen that two types of AFMFEM have perfect superparamagnetic and magnetic response property, and the saturation magnetization value is, respectively, 1.21 emu/g and 1.44 emu/g, manifesting that the trace pathogenic DNA can be separated by the magnetic field.

The properties of AFMFEM could decide the ability of enrichment, detection, and separation of DNA, and the amounts of amino grafted on the nanoparticle surfaces are especially important, because the combination between capture DNA and AFMFEM was formed through electrostatic binding. The more amounts of the amino on the surface, the more amounts of AFMFEM that could combine with capture DNA, and the stronger ability of enrichment and detection of Target DNA. The amounts of the amino grafted on AFMFEM can be evaluated through zeta potential detection. Figures 1(c) and 1(d) show, respectively, zeta potential spectra and TEM image of AFMFEM. From Figure 1(c), it can be seen that zeta potential of AFMFEM at neutral pH was +46.5 mV, which implied a large quantity of amino on the surface of AFMFEM, and the AFMFEM could disperse well in the water because of electrostatic repulsion. From Figure 1(d), it can be seen that the formed AFMFEM have uniform size about 100 ± 10 nm and good dispersity.

3.2. Preparation of Capture DNA-AFMFEM Probe. In order to optimize the combination of capture DNA with AFMFEM,

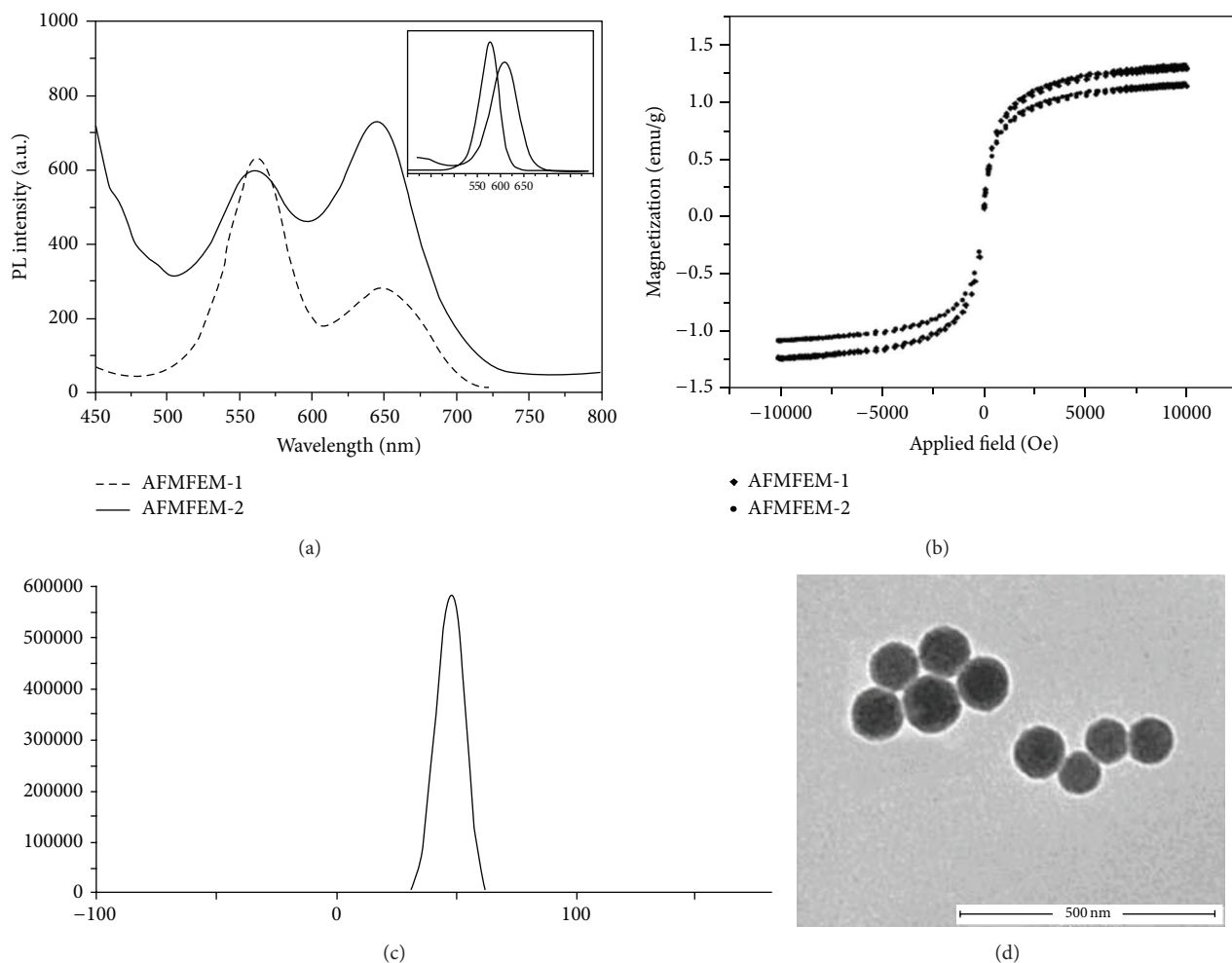


FIGURE 1: The fluorescence spectra of AFMFEM-1 and AFMFEM-2 (a); the picture in the upper right corner is the fluorescence spectra of QDs₁ and QDs₂; the hysteresis loops taken at 300 K for AFMFEM-1 and AFMFEM-2 (b); the zeta potential of AFMFEM (c); the TEM micrographs of AFMFEM (d).

different volumes of capture DNA (200 nM) were reacted with 10 μ L AFMFEM solution (3.6 mg/mL); the product was separated and measured by DLS. Figure 2(a) shows the hydrated radius of capture DNA-AFMFEM in solution at the various proportions of capture DNA and AFMFEM. From Figure 2(a), it can be seen that the hydrated radius of AFMFEM is about 125 ± 5 nm when there is no capture DNA, and the hydrated radius of capture DNA-AFMFEM increases gradually as capture DNA was added abidingly. When the proportion of capture DNA and AFMFEM reaches 8:1, we get the maximum hydrated radius in 135 nm. The result seems to be comparatively reasonable if hydrodynamic sizes of AFMFEM (130 nm) and capture DNA (2 nm) are considered. The volume of AFMFEM is slightly increased because the electrostatic force causes the DNA to pack tightly on the surface of AFMFEM. When the volume ratio of capture DNA and AFMFEM reaches 8:1, the adsorption of capture DNA on the AFMFEM reaches saturation. The hydrated radius of the product began to decrease due to the presence of excessive free capture DNA as capture DNA was added abidingly.

To further verify the measurement of DLS, the UV adsorption spectra of supernatant of the mixture with various volume ratio after magnetic separation were measured, to monitor the quantity of excessive free capture DNA. Figure 2(b) shows the results. From Figure 2(b), it can be seen that the UV adsorption of supernatant (260 nm) was almost the same for the volume ratio from 1:1 to 8:1, which indicates a little of excessive DNA dispersed in the supernatant. When the volume ratio is higher than 8:1, the UV absorption of supernatant increased rapidly with the volume ratio, which proves amounts of excessive DNA dispersed in the solution, and this phenomenon further indicates the capture DNA on the surface of AFMFEM reached saturation when the ratio is 8:1.

3.3. Nonspecific Hybridization of Capture DNA-AFMFEM-1 and Target DNA. For studying of DNA specific hybridization reaction, two groups of experiments were performed: in the first group, the HBV Target DNA and the HBV FITC-Complement DNA were used to connect with HAV capture

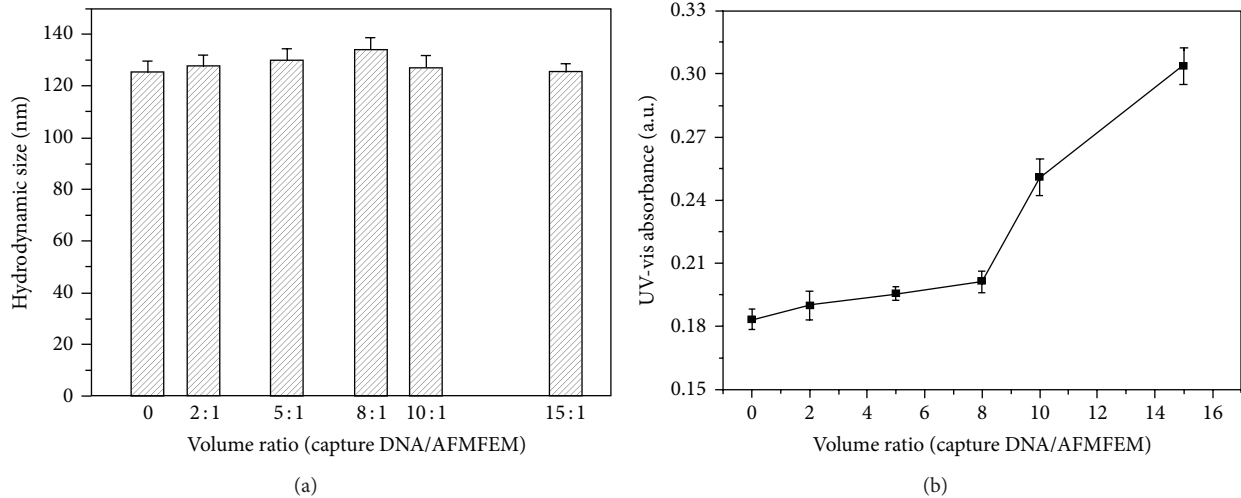


FIGURE 2: DLS analysis of capture DNA-AFMFEM probe prepared at various volume ratios of capture DNA (200 nM) to 10 μ L AFMFEM (3.6 mg/mL) (a); the adsorption spectra at 260 nm of the supernatant of the mixture with various volume ratios (DNA/AFMN) (b).

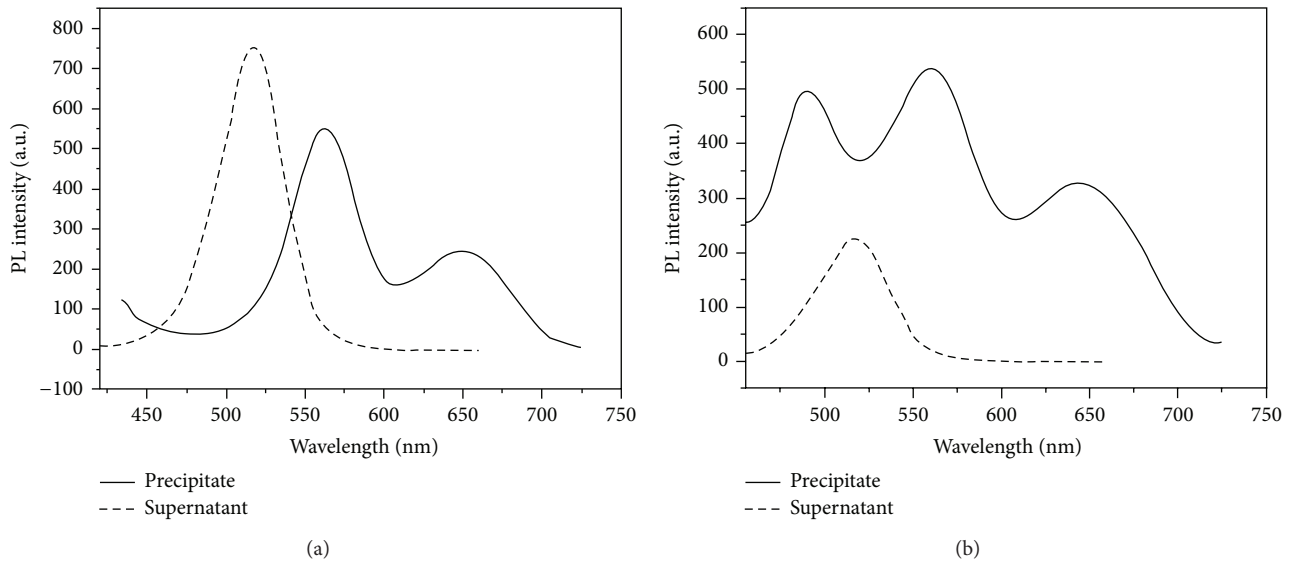


FIGURE 3: The investigation of nonspecific binding: HAV capture DNA-AFMFEM-1 with HBV Target DNA and HBV FITC-Complement DNA (a); HAV capture DNA-AFMFEM-1 with HAV Target DNA and HAV FITC-Complement DNA (b).

DNA-AFMFEM-1; in second group, the HAV Target DNA and the HAV FITC-Complement DNA were used to react with HAV capture DNA AFMFEM-1. The magnet was used to separate products and the fluorescence spectra of precipitation and supernatant were recorded. Figure 3(a) shows the results of the first group. The supernatant exhibits strong fluorescence peak at 510 nm, but there is no obvious fluorescence peak at 510 nm in the spectra of the precipitation, which proved that the hybridization reaction did not occur between HAV capture DNA AFMFEM-1 and the mixture of HBV Target DNA. But from Figure 3(b), the results of the second group, the spectra of precipitation separated by magnet show a strong fluorescence peak at 510 nm and the supernatant also exhibits strong fluorescence peak at 510 nm but lower than that of Figure 3(a); it proved that the hybridization reaction

has indeed occurred between HAV capture DNA AFMFEM-1 and the mixture of HAV Target DNA. The results of Figure 3 clearly demonstrate that HAV Target DNA and HBV Target DNA do not interfere with each other in the same system and guarantee the process of multicomponent immunoassay.

3.4. *Enrichment and Detection of Substrate Target DNA.* To verify the magnetic separation and enrichment capacity of AFMFEM, the same amounts of 100 μ L of HAV Target DNA (50 pM), FITC-Complement DNA, and capture DNA-AFMFEM-1 (15 μ L of AFMFEM saturated by capture DNA) were added into different volumes of BB solution (1, 10, and 50 mL) at room temperature. The amount of capture DNA-AFMFEM-1 was kept excess, and the final concentration of HAV Target DNA in the solution was 5, 0.5, and 0.1 pM,

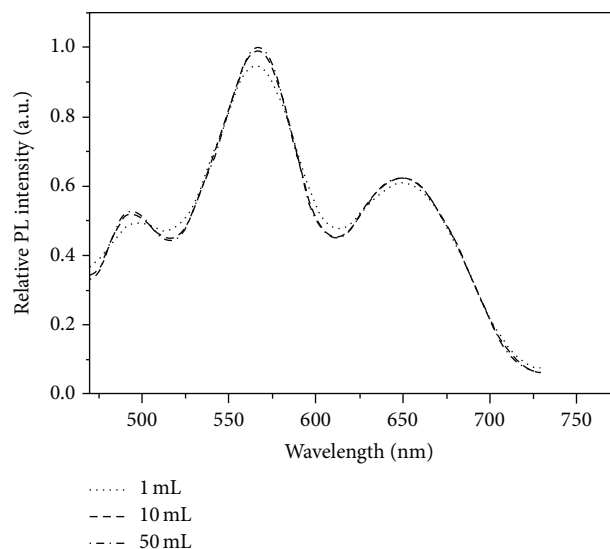


FIGURE 4: The fluorescence spectra of the hybridization complex separated from above 1 (dotted line), 10 (dashed line), and 50 (dotted and dashed line) mL solutions.

respectively. After stirring at room temperature for 2 h, the precipitation of each sample was separated by a magnet and was dispersed in 1 mL PBS buffer solution. Figure 4 shows the fluorescence spectra of resultant complex. As shown in Figure 4, there are three similar fluorescence peaks in the fluorescence spectra of the products which are fabricated by enrichment and separation of AFMFEM-1-HAV capture DNA in three different samples. The peak at 510 nm is the fluorescence peak of FITC-Target DNA; the peaks at 560 nm and 650 nm are the fluorescence peak of capture DNA-AFMFEM-1, and the fluorescence intensity of three fluorescence peaks at 510 nm is the same, which indicates that the FITC-Target DNA dispersed in 1, 10, mL or 50 mL BB solution can be enriched completely and separated by a magnet same as to the FITC-Target DNA dispersed in 1 mL BB solution. The results imply that 0.1 pM FITC-Target DNA could be detected sensitively. The reported detection limit of other technologies based on nanoparticles is 4 nM for QDs [28], 10 pM for $\text{Fe}_3\text{O}_4/\text{Eu}:\text{Gd}_2\text{O}_3$ [29], 5 pM for cyanide dyed silica nanoparticles DNA microarrays [30], and 1 pM for scanometric detection of gold-silver-enhanced nanoparticles in DNA microarrays [31]. In comparison, our analysis method provides a high sensitive nanoimmunoassay platform for enrichment, detection, and separation of trace DNA. With the improvement the performances of magnetic fluorescent encoded nanoparticles, the sensitivity will be further improved, and the nanoimmunoassay technology will be used for detection and analysis of other viruses in the future.

3.5. Study of Hybridization Kinetics. For studying the hybridization kinetics of AFMFEM, in this work, the same volume of different concentration of Target DNA was reacted with FITC-Complement DNA and 50 μL capture DNA (50 μL of AFMFEM saturated by capture DNA). The fluorescence spectra were obtained at different hybridization time, as

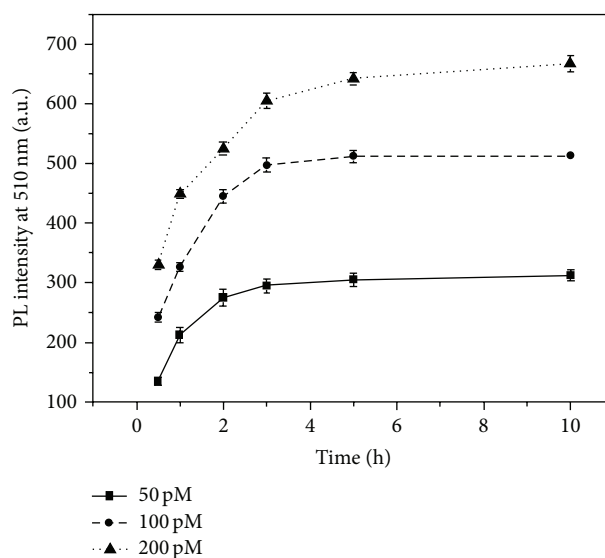


FIGURE 5: Hybridization kinetics curve with the concentration of target DNA was 50 (■), 100 (●), and 200 pM (▲), respectively.

schematically outlined in Figure 5. Although the amount of capture DNA-AFMFEM probe was constant, the reaction time of various concentrations of target DNA hybridized with capture DNA-AFMFEM was different. The hybridization time for obtaining stable composite was short with decrease of the concentration of target DNA, the reaction time of 50 pM Target DNA hybridized with capture DNA-AFMFEM was only 1 h, and the reaction time of 200 pM Target DNA hybridized with capture DNA-AFMFEM was about 3 h.

3.6. Detection of Pathogenic DNA Using Fluorescent Sandwich Immunoassay Principle. In order to detect HAV Target DNA and HBV Target DNA in this work, sandwich immunoassay technology was adopted to analyze and detect unlabeled pathogenic DNA in the solution. The different concentrations of HAV Target DNA in the range of 0–120 pM were added into mixed solution of HAV FITC-Complement DNA and capture DNA-AFMFEM-1 (50 μL of AFMFEM saturated by capture DNA), and the fluorescence spectra of the product were obtained by fluorescence spectrophotometer. Figure 6 shows the relationship of fluorescent intensity and the amount of HAV Target DNA conjugated on the surface of AFMFEM-1 by electrostatic interaction. The illustration of Figure 6 exhibits the relatively fluorescent intensities ($I_{500\text{ nm}}/I_{560\text{ nm}}$) versus the concentrations of pathogenic DNA. As we expected, the relationship of the concentration of HAV Target DNA in the linear range from 0 to 100 pM and the relatively fluorescence intensity ($I_{500\text{ nm}}/I_{560\text{ nm}}$) of the product is proportional linear relationship. The linear regression equation is as follows: $I_{500\text{ nm}}/I_{560\text{ nm}} = 0.50197 + 0.00527C_{\text{HAV Target DNA}}$ (pM), and the coefficient of correlation is 0.96371, and the limit of detection for immunoassay is 0.1 pM of HAV Target DNA. Upon further addition of HAV Target DNA, there is no obvious change of fluorescent intensity ($I_{500\text{ nm}}/I_{560\text{ nm}}$). For the detection of HBV Target DNA, a similar process was

TABLE 1: The detection of pathogenic DNA in human serum samples.

Serum samples	Added (pM)	Founded (pM)	Recovery (%)	RSD (% $n = 3$)
1	HAV 1.5 pM	1.48 ± 0.04	98.67	1.06
	HBV 1.5 pM	1.54 ± 0.03	102.67	2.18
2	HAV 2.0 pM	2.06 ± 0.02	103.00	1.83
	HBV 2.0 pM	2.03 ± 0.05	101.50	0.92
3	HAV 3.0 pM	3.08 ± 0.06	102.67	1.10
	HBV 3.0 pM	3.09 ± 0.05	103.00	1.22

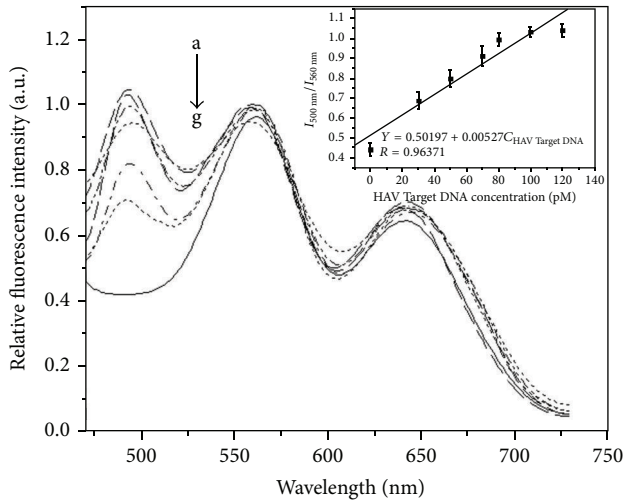


FIGURE 6: Fluorescence emission spectra of hybridization complex with a series of different concentrations of HAV Target DNA added (a–g: 0 pM, 30 pM, 50 pM, 70 pM, 80 pM, 100 pM, and 120 pM). The inset shows the relationship between relative fluorescent intensity of $I_{500\text{ nm}}/I_{560\text{ nm}}$ after immunoreaction and the concentration of HAV Target DNA.

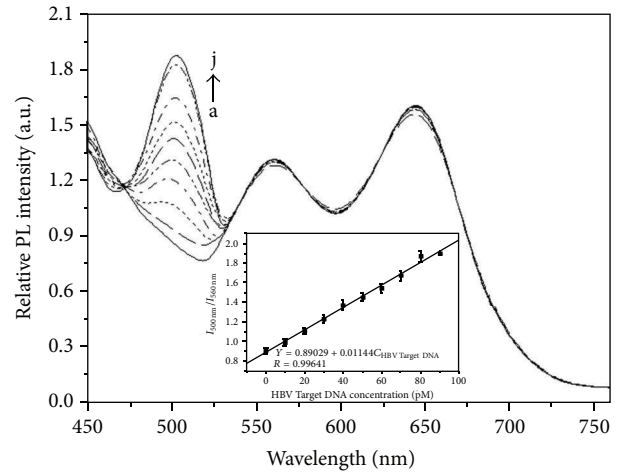


FIGURE 7: Fluorescence emission spectra of hybridization complex with a series of different concentrations of HBV Target DNA added (a–j: 0 pM, 10 pM, 20 pM, 30 pM, 40 pM, 50 pM, 60 pM, 70 pM, 80 pM, and 90 pM). The inset shows the relationship between relative fluorescent intensity of $I_{500\text{ nm}}/I_{560\text{ nm}}$ after immunoreaction and the concentration of HBV Target DNA.

used. From Figure 7, it can be seen that the fluorescence intensity at 500 nm also increases gradually with increasing concentration of HBV Target DNA in the range from 0 to 90 pM. The fluorescence intensity of complex emission at 500 nm reaches a plateau when the concentration of HBV Target DNA reaches 90 pM, which indicates the immunointeraction among FITC-Complement DNA, Target DNA, and capture DNA-AFMFEM-2 is complete at this concentration. The linear regression equation is as follows: $I_{500\text{ nm}}/I_{560\text{ nm}} = 0.89029 + 0.01144C_{\text{HBV Target DNA}} \text{ (pM)}$, and the coefficient of correlation is 0.99641, and the limit of detection for immunoassay is 0.12 pM of HBV Target DNA.

3.7. Detection of Pathogenic DNA in Human Serum Samples. To assess the application of this nanoimmunoassay system in complex biological systems, the analyses of pathogenic DNA HAV and HBV in human serum samples were carried out. Serum is what remains from whole blood after coagulation; the chemical composition is similar to plasma but does not contain coagulation protein [32]. We performed detection of pathogenic DNA in 10-fold-diluted serum samples under the optimal conditions. The results obtained by standard addition

method were listed in Table 1. From the table, we can see that the RSD was lower than 3% and the average recoveries of pathogenic DNA HAV and HBV in the real samples were in the range of 98.7–103.0%, indicating that the accuracy and precision of the proposed method were satisfactory.

4. Conclusion

In this work, we have reported a novel strategy for multiplexed immunoassay with magnetic fluorescent encoded composite nanoparticles. The magnetic fluorescent encoded composite nanoparticles, which contain two colors of CdTe QDs and supermagnetic Fe_3O_4 nanoparticles for fluorescent encoded and excellent magnetic response property, are a new powerful tool for biological applications. Based on this novel nanomaterial, in this study, we establish a new fluorescent analytical method for multicomponent biological immunoassay by the combination of amino-modified magnetic fluorescent encoded nanoparticles and sandwich immunoassay principle. And this method was successfully applied for the detection and separation of two types of subtrace pathogenic DNA. Compared with the traditional method, the proposed method is time-saving and easy to

operate and has high sensitivity (0.1 pM for HAV DNA and 0.12 pM for HBV DNA), and most importantly it can be used for multiplex immunoanalysis and could be applied in many other antibody-antigen systems and virus detection.

Conflict of Interests

The authors declare that there is no conflict of interests regarding the publication of this paper.

Acknowledgments

This project was supported by the National Natural Science Foundation of China (no. 81401499), Startup grant of University of Macau (SRG2015-00007-FHS), Quanmin Oral Graduate Sci-Tech Innovation Foundation, and the President Fund of Liaoning Medical University (nos. XZJJ20140101, QM2014006, and 2014D06).

References

- [1] Z. Liu, Y. Q. Song, C. H. Xie, F. Zhu, and X. Bao, "Clustering gene expression data analysis using an improved EM algorithm based on multivariate elliptical contoured mixture models," *Optik*, vol. 125, no. 21, pp. 6388–6394, 2014.
- [2] S.-Y. Xue, Z.-Y. Li, H.-J. Zhi et al., "Metabolic fingerprinting investigation of *Tussilago farfara* L. by GC-MS and multivariate data analysis," *Biochemical Systematics and Ecology*, vol. 41, pp. 6–12, 2012.
- [3] F. Chen, W. D. Taylor, W. B. Anderson, and P. M. Huck, "Application of fingerprint-based multivariate statistical analyses in source characterization and tracking of contaminated sediment migration in surface water," *Environmental Pollution*, vol. 179, pp. 224–231, 2013.
- [4] X. W. Feng, Q. H. Zhang, P. S. Cong, and Z. L. Zhu, "Preliminary study on classification of rice and detection of paraffin in the adulterated samples by Raman spectroscopy combined with multivariate analysis," *Talanta*, vol. 115, pp. 548–555, 2013.
- [5] G. N. Wang and X. G. Su, "The synthesis and bio-applications of magnetic and fluorescent bifunctional composite nanoparticles," *Analyst*, vol. 136, no. 9, pp. 1783–1798, 2011.
- [6] L. Shu, J. Zhou, X. C. Yuan et al., "Highly sensitive immunoassay based on SERS using nano-Au immune probes and a nano-Ag immune substrate," *Talanta*, vol. 123, pp. 161–168, 2014.
- [7] D. Knopp, D. P. Tang, and R. Niessner, "Review: bioanalytical applications of biomolecule-functionalized nanometer-sized doped silica particles," *Analytica Chimica Acta*, vol. 647, no. 1, pp. 14–30, 2009.
- [8] G. N. Wang, X. Z. Zhang, A. Skallberg et al., "One-step synthesis of water-dispersible ultra-small Fe_3O_4 nanoparticles as contrast agents for T_1 and T_2 magnetic resonance imaging," *Nanoscale*, vol. 6, no. 5, pp. 2953–2963, 2014.
- [9] P. B. Santhosh and N. P. Ulrih, "Multifunctional superparamagnetic iron oxide nanoparticles: promising tools in cancer theranostics," *Cancer Letters*, vol. 336, no. 1, pp. 8–17, 2013.
- [10] J. Yu, R. Hao, F. G. Sheng, L. L. Xu, G. J. Li, and T. L. Hou, "Hollow manganese phosphate nanoparticles as smart multifunctional probes for cancer cell targeted magnetic resonance imaging and drug delivery," *Nano Research*, vol. 5, no. 10, pp. 679–694, 2012.
- [11] G. N. Wang, L. Jin, Y. K. Dong et al., "Multifunctional Fe_3O_4 -CdTe@ SiO_2 -carboxymethyl chitosan drug nanocarriers: synergistic effect towards magnetic targeted drug delivery and cell imaging," *New Journal of Chemistry*, vol. 38, no. 2, pp. 700–708, 2014.
- [12] D. Zhao, W. H. Chan, Z. K. He, and T. Qiu, "Quantum dot-ruthenium complex dyads: recognition of double-strand DNA through dual-color fluorescence detection," *Analytical Chemistry*, vol. 81, no. 9, pp. 3537–3543, 2009.
- [13] B. Sun, Y. Zhang, K.-J. Gu, Q.-D. Shen, Y. Yang, and H. Song, "Layer-by-layer assembly of conjugated polyelectrolytes on magnetic nanoparticle surfaces," *Langmuir*, vol. 25, no. 10, pp. 5969–5973, 2009.
- [14] J. Zhang, S. Q. Zhao, K. Zhang, and J. Q. Zhou, "Cd-doped ZnO quantum dots-based immunoassay for the quantitative determination of bisphenol A," *Chemosphere*, vol. 95, pp. 105–110, 2014.
- [15] J. Kim, S. Kwon, J.-K. Park, and I. Park, "Quantum dot-based immunoassay enhanced by high-density vertical ZnO nanowire array," *Biosensors and Bioelectronics*, vol. 55, pp. 209–215, 2014.
- [16] E. Cassette, M. Helle, L. Bezdetsnaya, F. Marchal, B. Dubertret, and T. Pons, "Design of new quantum dot materials for deep tissue infrared imaging," *Advanced Drug Delivery Reviews*, vol. 65, no. 5, pp. 719–731, 2013.
- [17] J. B. Liu, X. H. Yang, X. X. He et al., "Fluorescent nanoparticles for chemical and biological sensing," *Science China Chemistry*, vol. 54, no. 8, pp. 1157–1176, 2011.
- [18] E. Q. Song, W. Y. Han, J. R. Li et al., "Magnetic-encoded fluorescent multifunctional nanospheres for simultaneous multicomponent analysis," *Analytical Chemistry*, vol. 86, no. 19, pp. 9434–9442, 2014.
- [19] J. Hu, M. Xie, C.-Y. Wen et al., "A multicomponent recognition and separation system established via fluorescent, magnetic, dualencoded multifunctional bioprobes," *Biomaterials*, vol. 32, no. 4, pp. 1177–1184, 2011.
- [20] E. Q. Song, W. Y. Han, H. Y. Xu et al., "Magnetically encoded luminescent composite nanoparticles through layer-by-layer self-assembly," *Chemistry—A European Journal*, vol. 20, no. 45, pp. 14642–14649, 2014.
- [21] G. N. Wang, Y. Gao, H. Huang, and X. G. Su, "Multiplex immunoassays of equine virus based on fluorescent encoded magnetic composite nanoparticles," *Analytical and Bioanalytical Chemistry*, vol. 398, pp. 805–813, 2010.
- [22] Y. Xu, A. Karmakar, D. Wang et al., "Multifunctional Fe_3O_4 cored magnetic-quantum dot fluorescent nanocomposites for RF nanohyperthermia of cancer cells," *Journal of Physical Chemistry C*, vol. 114, no. 11, pp. 5020–5026, 2010.
- [23] F. Zhan and C. Y. Zhang, "Bifunctional nanoparticles with superparamagnetic and luminescence properties," *Journal of Materials Chemistry*, vol. 21, no. 13, pp. 4765–4767, 2011.
- [24] L. Wang, R. M. Liao, and X. Z. Li, "Layer-by-layer deposition of luminescent polymeric microgel films on magnetic Fe_3O_4 @ SiO_2 nanospheres for loading and release of ibuprofen," *Powder Technology*, vol. 235, pp. 103–109, 2013.
- [25] G. N. Wang, P. Xie, C. R. Xiao, P. F. Yuan, and X. G. Su, "Magnetic fluorescent composite nanoparticles for the fluoroimmunoassays of newcastle disease virus and avian virus arthritis virus," *Journal of Fluorescence*, vol. 20, no. 2, pp. 499–506, 2010.
- [26] G. N. Wang, X. G. Su, S. J. Yang, Y. H. Jia, and D. H. Li, "The double-effect mechanism between Fe_3O_4 nanoparticles and MSA-capped CdTe QDs," *Journal of Luminescence*, vol. 132, no. 9, pp. 2505–2511, 2012.

- [27] G. N. Wang, C. Wang, and X. G. Su, "Synthesis of dual fluorescent encoding magnetic composite nanoparticles," *Journal of Nanoscience and Nanotechnology*, vol. 10, no. 3, pp. 1956–1963, 2010.
- [28] X. Zhou and J. Zhou, "Improving the signal sensitivity and photostability of DNA hybridizations on microarrays by using dye-doped core-shell silica nanoparticles," *Analytical Chemistry*, vol. 76, no. 18, pp. 5302–5312, 2004.
- [29] D. Gerion, F. Q. Chen, B. Kannan et al., "Room-temperature single-nucleotide polymorphism and multiallele DNA detection using fluorescent nanocrystals and microarrays," *Analytical Chemistry*, vol. 75, no. 18, pp. 4766–4772, 2003.
- [30] T. A. Taton, G. Lu, and C. A. Mirkin, "Two-color labeling of oligonucleotide arrays via size-selective scattering of nanoparticle probes," *Journal of the American Chemical Society*, vol. 123, no. 21, pp. 5164–5165, 2001.
- [31] X. J. Zhao, R. Tapeç-Dytioco, K. Wang, and W. H. Tan, "Collection of trace amounts of DNA/mRNA molecules using genomagnetic nanocaptors," *Analytical Chemistry*, vol. 75, no. 14, pp. 3476–3483, 2003.
- [32] W. D. Na, X. T. Liu, L. Wang, and X. G. Su, "Label-free aptamer biosensor for selective detection of thrombin," *Analytica Chimica Acta*, vol. 899, pp. 85–90, 2015.

Research Article

MP Resulting in Autophagic Cell Death of Microglia through Zinc Changes against Spinal Cord Injury

Dingding Li,¹ Guannan Wang,² Donghe Han,³ Jing Bi,³ Chenyuan Li,⁴
Hongyu Wang,¹ Zhiyuan Liu,¹ Wei Gao,⁴ Kai Gao,¹ Tianchen Yao,¹
Zhanghui Wan,¹ Haihong Li,¹ and Xifan Mei¹

¹Department of Orthopedic Surgery, First Affiliated Hospital of Liaoning Medical University, Jinzhou 121000, China

²Department of Chemistry, College of Pharmacy, Liaoning Medical University, Jinzhou 121000, China

³Department of Neurobiology, Key Laboratory of Neurodegenerative Diseases of Liaoning Province, Liaoning Medical University, Jinzhou 121000, China

⁴Department of Basic Medical Sciences, Liaoning Medical University, Jinzhou 121000, China

Correspondence should be addressed to Xifan Mei; meixifan1971@163.com

Received 4 February 2015; Accepted 16 February 2015

Academic Editor: Xuanjun Zhang

Copyright © 2016 Dingding Li et al. This is an open access article distributed under the Creative Commons Attribution License, which permits unrestricted use, distribution, and reproduction in any medium, provided the original work is properly cited.

Methylprednisolone pulse therapy (MPPT), as a public recognized therapy of spinal cord injury (SCI), is doubted recently, and the exact mechanism of MP on SCI is unclear. This study sought to investigate the exact effect of MP on SCI. We examined the effect of MP in a model of SCI in vivo and an LPS induced model in vitro. We found that administration of MP produced an increase in the Basso, Beattie, and Bresnahan scores and motor neurons counts of injured rats. Besides the number of activated microglia was apparently reduced by MP in vivo, and Beclin-1 dependent autophagic cell death of microglia was induced by MP in LPS induced model. At the same time, MP increases cellular zinc concentration and level of ZIP8, and TPEN could revert effect of MP on autophagic cell death of microglia. Finally, we have found that MP could inhibit NF- κ B in LPS induced model. These results show that the MP could result in autophagic cell death of microglia, which mainly depends on increasing cellular labile zinc, and may be associated with inhibition of NF- κ B, and that MP can produce neuroprotective effect in SCI.

1. Introduction

Spinal cord injury (SCI) has been studied for over 100 years, and its harm that lies in causing lifelong disability and psychological burden have been described in considerable papers [1]. However, exactly effective therapies of SCI have not advanced to improve the recovery of SCI patients. Therefore, it is critical to find out therapeutic strategies for SCI patients [2]. The pathophysiology of SCI involves two mechanisms, primary and secondary mechanisms [3]. Secondary injury mechanisms, which are more pivotal in the recovery of SCI, include inflammation, oxidization, immunological reaction, electrolyte disorder, vascular damage, and loss of energy balance [4].

Methylprednisolone (MP) is a synthetic glucocorticoid agonist, with major properties of potent anti-inflammation

and suppressing immunity, and methylprednisolone pulse therapy (MPPT) is the only public recognized therapy of SCI at present in acute phase, in order to minimize neurological damage [5]. Besides, MP gets rid of free radical-induced or iron-catalyzed lipid peroxidation and protein oxidative damage [6, 7]. MP also has protective effect on vascular injury after SCI, through diverse aspects of tissue edema, vascular permeability, and polymorphonuclear cell infiltration [8]. However, the exact mechanism of MP on SCI is not perceived for its complicated mechanisms. And there are new researches on high dose of MP, giving out contrary results against the protection of MP on SCI [9, 10].

Autophagy is involved not only in the protein synthesis and degradation, digestion of intracellular components, but also in the execution of cell death, nonapoptotic programmed cell death, which is also known as autophagic cell death

[11]. Previous studies have reported that autophagic cell death occurs in various diseases. Autophagic cell death was induced through glutamate-mediated GSK-3 β activation in astrocytes [12] or through elevation of Beclin-1 in neurons [13] after traumatic brain injury. Autophagic cell death participates in cardiac myocytes during myocardial infarction, ischemia/reperfusion, and heart failure [14]. Autophagic cell death of hepatocyte results in liver graft dysfunction [15]. Furthermore, autophagy is closely associated with inflammation [16, 17]. Loss of the autophagy protein Atg16L1 increases IL-1 β production induced by endotoxin [18]. Dysfunction of autophagy related 16-like 1 (ATG16L1) triggers chronic intestinal inflammation [19].

Interestingly, MP administration causing plasma zinc decreasing in human was reported [20–22]. Rekers recently found that MP regulates intracellular concentrations of zinc through influencing MT-1 expression [23]. Nowadays zinc is increasingly recognized as an ionic messenger or a neurotransmitter more than a micronutrient [24]. In our previous study, we demonstrated that spinal cord zinc changes after SCI. In the current study, we suppose that the neuronal protective role of MP may relate to the activation of autophagy through the changes of zinc, as an ionic messenger.

2. Methods and Materials

2.1. Animals and Drug Administration. Adult male Sprague-Dawley rats (220 \pm 20.0 g, aged 2-3 months) were purchased from Capital Medical University (Beijing, China), and the study was approved by the Animal Care and Use Committee of Liaoning Medical University. Five animals were used in each experiment group at each time point. The animals were housed in individual cages with 12 h light/dark schedule, relative humidity of 50%, controlled temperature (24 \pm 1°C), and free access to water and food before and after surgery. Rats were randomly and evenly divided into two groups: SCI-only group and SCI + MP group. Compared to SCI-only group, rats of SCI + MP group received not only SCI, but also injection of methylprednisolone (MP, 30 mg/kg, i.v., Sigma-Aldrich, St. Louis, MO, USA) once a day in first week. And in each group, subgroups were set up as normal animal (without injury), 1 hour (1 h), 6 hours (6 h), 12 hours (12 h), 18 hours (18 h), 1 day (1 d), 3 days (3 d), 7 days (7 d), 14 days (14 d), 21 days (21 d), and 60 days (60 d) after SCI.

2.2. Acute Spinal Cord Injury Model. Following 10% chloral hydrate (2 mL/kg, i.p.) anesthesia, rats were positioned on a platform, with continuous rectal temperature monitored and maintained at 37.0 \pm 0.5°C by a heating pad. Laminectomy was carried out at the level of T10 to expose the intact dorsal cord surface. Then a contusion was induced by a self-made electromagnetic programmed weight-drop device in the spinal cord corresponding to the T10 spinous process, centering at the posterior median spinal vessels. The striking force was 25 \times 3 g*cm: the iron stick was 25 g in weight and 3 cm in bottom diameter, the dropping distance was 3 cm, and the time of contact with the dura mater was 0.1 s. After operation, the wound was sterilely closed.

2.3. Primary Microglia Cell Cultures. Spinal cord tissues from postnatal day 1 SD rat were collected and mechanically fragmented, then digested with 2.5 mg/mL trypsin-EDTA buffered with 10 mM HEPES (GIBCO) for 12 min at 37°C, and finally mechanically dissociated. Cells were planted on poly-D-lysine (30–70 kDa, Sigma-Aldrich, St. Louis, MO, USA) coated dishes in DMEM medium, 10% FBS, and 1% penicillin/streptomycin solution (GIBCO). After 10 days, microglia were dislocated by the addition of 12 mM lidocaine. Isolated microglia were planted on poly-D-lysine coated plates at a density of 1.5*10⁵ cells/mL in DMEM medium (10% FBS, 1% penicillin/streptomycin solution).

2.4. Behavioral Test. At different time points (normal, 3 d, 7 d, 21 d, and 60 d) of each group, behavioral testing was analyzed as described previously [25, 26]. All experiments were performed in a double-blind manner.

2.5. Nissl Stain. Spinal cord sections of rats were prepared as previously described [27]. Every tenth section was collected and stained with cresyl violet in each group.

2.6. Immunohistochemistry. Spinal cord sections of rats were prepared as previously described [27]. The following antibodies were applied: goat anti-Iba-1 (ionized calcium binding adaptor molecule 1, microglia-specific marker) antibody (4 μ g/mL; Abcam Cambridge, UK). The following secondary antibodies were applied: rabbit anti-goat IgG secondary antibody (1 : 500; Origene).

2.7. RNA Extraction and RT-PCR Analysis. Spinal cord tissues were collected from rats in each group, total mRNA were generated as previously described, and real-time PCR was analyzed as previously described by using an Applied Biosystems 7500 Real-Time PCR System (Foster City, CA, USA) [28]. In brief, according to our previous protocol, we also use TRIzol RNA isolation reagent to purify total cellular RNA and GAPDH (Chemicon International Temecula, CA, USA) as the internal reference. The iNOS (inducible nitric oxide synthase), IL-6 (interleukin-6), IL-10 (interleukin-10), Beclin-1, LC-3B (microtubule-associated protein 1 light chain 3B), and ZIP8 (zinc transport SLC39A8) primer sequences were selected by using a Lasergene (DNA Star Inc., WI, USA) program.

2.8. Atomic Absorption Spectrometry. Spinal cord sections of rats at injured site were collected to be weighed, and we recorded the weight (about 0.5 g–1 g). Then specimens were moved to digestion tank and digested by automatic digestion apparatus (ST-60, Polytech, China) as in the following steps: (1) adding 100% HNO₃ 4 mL and 100% HClO₄ 1 mL, respectively; (2) vibrating at 100% speed for 1 minute; (3) heating at 100°C for 30 minutes; (4) vibrating at 100% speed for 1 minute; (5) heating at 180°C for 30 minutes; (6) cooling down for 30 minutes; and (7) diluting volumes to 20 mL with 1% HNO₃. Then solutions were measured with atomic absorption spectrometry (PE AA800, Perkinelmer, USA) for zinc. Venous blood samples (4 mL) of rats were collected for

analysis of zinc, and after centrifugation, serum was stored at -20°C until analysis. The samples were thawed at 37°C and diluted to 20 mL with 1% HNO_3 . Then samples were detected by flame atomic absorption spectrometry.

2.9. Immunofluorescence Staining. In vitro, lipopolysaccharide (LPS, 100 ng/mL, Sigma-Aldrich, St. Louis, MO, USA) was added into the primary cultured microglia; at the same time MP (10 μM) was added into the LPS inflammation model. The details of staining were as previously described [29]. The following primary antibodies were used, based on differing targets: goat anti-Iba-1 antibody (4 $\mu\text{g}/\text{mL}$; Abcam Cambridge, UK). The following secondary antibodies were applied: FITC donkey anti-goat IgG secondary antibody (1:500; Abcam Cambridge, UK).

2.10. Western Blot. Western blot was performed by using a standard protocol as previously described [29]. Samples were normalized to 1 mg/mL and the loading volume was 20 mL/well. The membranes were, respectively, incubated with rabbit polyclonal anti-LC-3B (1:500; Novus Biologicals), rabbit polyclonal Beclin-1 (1:1000; Abcam Cambridge, UK), rabbit polyclonal ZIP8 (1:1000; Santa Cruz Biotechnology), rabbit polyclonal nuclear factor-kappa beta ($\text{NF-}\kappa\beta$) (1:1000, Abcam Cambridge, UK), rabbit polyclonal anti-iNOS antibody (1:1000, Abcam Cambridge, UK), and rabbit anti- β -actin (1:500; Santa Cruz Biotechnology). The bound antibodies were detected using goat anti-rabbit IgG-HRP antibody (1:1000; Abcam Cambridge, UK). The protein bands were visualized by an ECL detection system (Pierce Chemical, Rockford, IL, USA) and quantified by Image J software (NIH, Bethesda, MD).

2.11. ELISA. Spinal cord tissues were collected from rats and dissected and homogenized in RIPA buffer. IL-6, IL-10, and TNF- α (tumor necrosis factor- α) (both Origene) were measured using respective ELISA kit according to the manufacturer's instructions and analyzed by microplate reader (Dynex Technology, Chantilly, VA, USA).

2.12. Cell Proliferation Analysis. Cells were planted on 96-well plates at 4000 cells per well. Different drug administration (nothing, MP (10 μM), LPS (100 ng/mL), LPS (100 ng/mL) + 3-MA (5 μM , Sigma-Aldrich, St. Louis, MO, USA), LPS (100 ng/mL) + rapamycin (200 nM, Sigma-Aldrich, St. Louis, MO, USA), LPS (100 ng/mL) + MP (10 μM), LPS (100 ng/mL) + MP (10 μM) + 3-MA (5 μM), and LPS (100 ng/mL) + MP (10 μM) + TPEN (tetrakis (2-pyridylmethyl-1) ethylenediamine, 1 μM) (Santa Cruz Biotechnology)) were added to microglia cultures. A day later, cell proliferative activity was assessed by 3-(4,5-dimethylthiazol-2-yl)-2,5-diphenyltetrazolium bromide (MTT) assay (Sigma-Aldrich) according to the instructions of the manufacturer. Absorbance was measured at a test wavelength of 570 nm and a reference wavelength of 630 nm for each well using a microplate reader (Dynex Technology, Chantilly, VA, USA).

2.13. Cellular Zinc Stain. Primary cultured microglia were stained with 5 μM FluoZin-3-AM (Invitrogen) in culture media for 15 min in a humidified CO_2 incubator, imaged by fluorescence microscope, and analyzed by microplate reader (Dynex Technology, Chantilly, VA, USA) according to the manufacturer's instructions.

2.14. Statistical Analysis. Data are expressed as the mean \pm SEM or SD. Statistical evaluation of the data was performed using one-way analysis of variance (ANOVA) and Dunnett's post hoc test. P values < 0.05 were considered statistically significant.

3. Result

3.1. MP Has a Neuroprotective Effect on SCI. To evaluate the effect of MP on the recovery of SCI, BBB scores firstly were assessed in SCI group and SCI + MP group at different time points (3 d, 7 d, 21 d, and 60 d) after injury. As shown in Figure 1(a), the averages of the total BBB scores were significantly lower in SCI group than SCI + MP group since 7 d after injuries. And especially 60 days after contusion, MP treatment increased BBB scores to around 11 compared to 7 of SCI group, indicating that locomotor activity was significantly promoted by MP. Furthermore, the effect of MP on the numbers of motor neurons in spinal cord was investigated using Nissl staining at 3 days after SCI (Figure 1(b)), and average motoneuron counts per section in thoracic spinal cord of rat were calculated (Figure 1(c)). SCI group showed extensive loss of large anterior horn cells. In contrast, motor neurons of the anterior horns were significantly reserved in rats treated with MP.

3.2. MP Reduced Microglia Activation Maybe via Beclin-1 Dependent Autophagic Cell Death after Spinal Cord Injury. In order to examine whether microglia activation was inhibited by MP, the representative protein Iba-1 of microglia/macrophages was assessed by immunohistochemistry. Twelve hours after MP administration, number of activated microglia/macrophages, stained by Iba-1, was apparently reduced, compared to a mass of expression in SCI-only group (Figure 2(a)). Furthermore, other relevant markers associated with activation of microglia were then tested by RT-PCR. Levels of iNOS, IL-6, and IL-10 in SCI + MP group at 12 h and 18 h were lower than those in SCI group (Figure 2(b)). And we supposed whether autophagic cell death resulted in the decreased number of microglia; the reprehensive proteins of autophagy were assessed by western blot. The levels of Beclin-1 and LC-3B, as we expected, were significantly increased in SCI + MP group compared to SCI-only group (Figure 2(c)).

3.3. MP Increases the Level of Zinc and ZIP8. In order to examine whether tissue zinc level changed after MP administration in SCI rat, atomic absorption spectrometry was used to quantify the content of zinc elements. As shown in Figure 3(a), tissue zinc decreased from 40 $\mu\text{g}/\text{g}$ to 22 $\mu\text{g}/\text{g}$ in six hours after SCI and returned to baseline zinc level

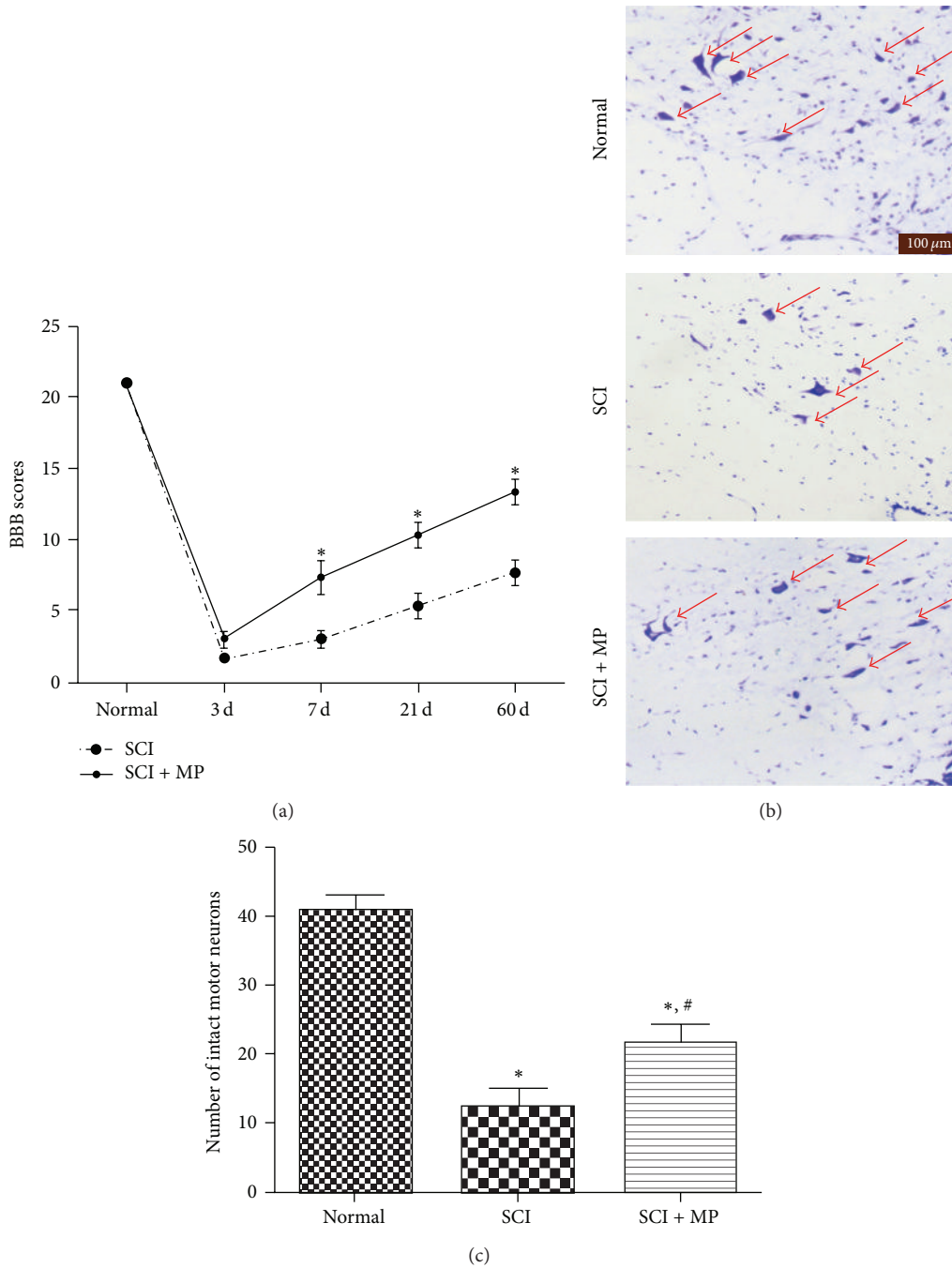
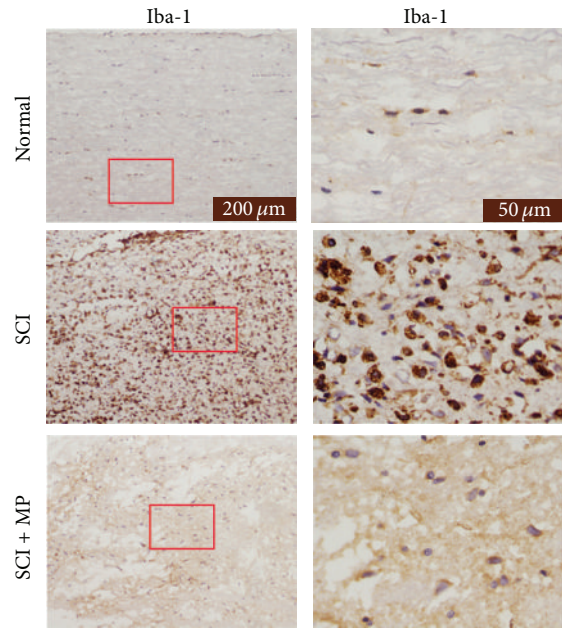


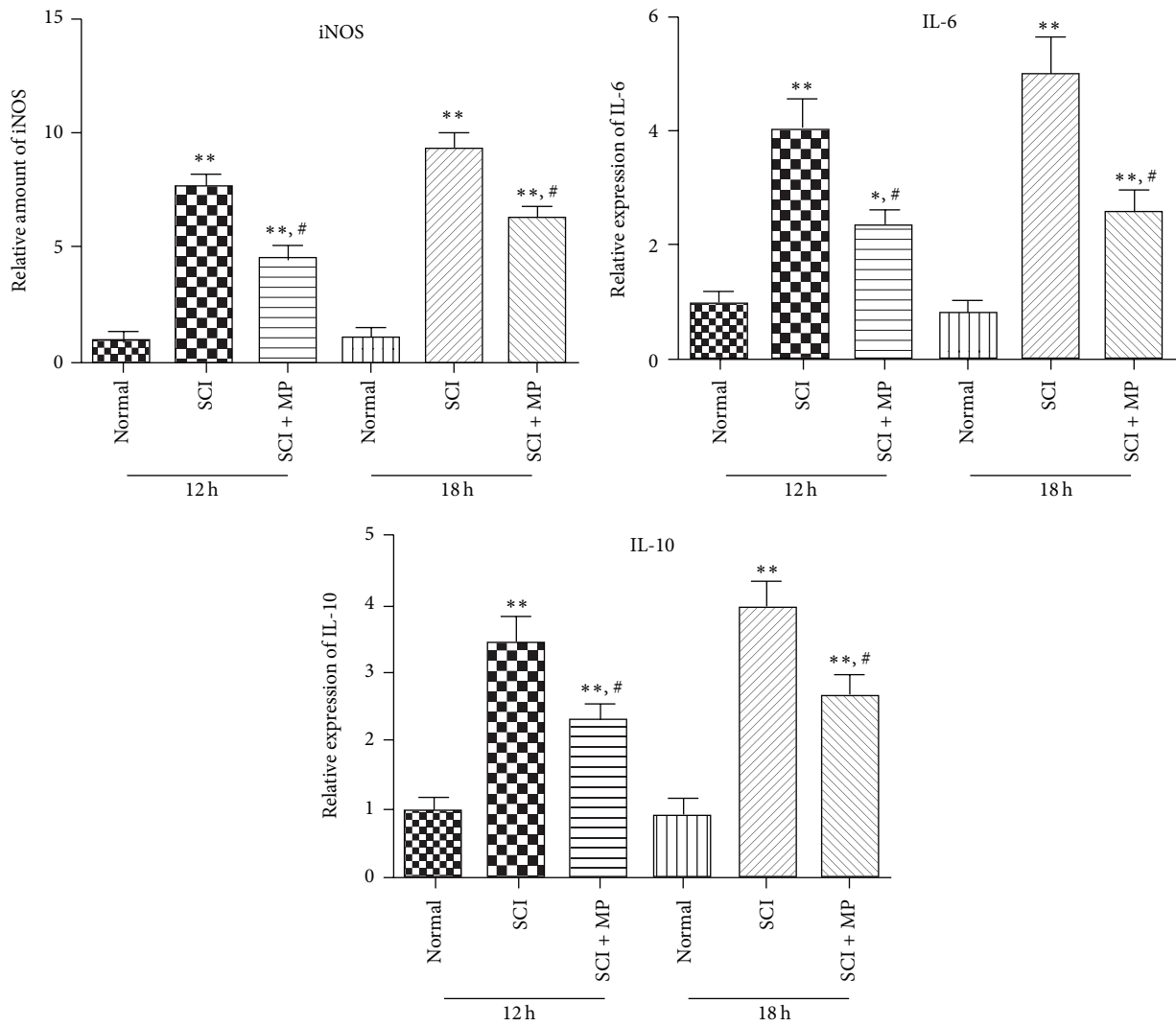
FIGURE 1: MP promoted neurologic motor function and histologic assessment in SCI rat. (a) BBB scores of rats in SCI-only group and MP group at each time point (3 d, 7 d, 21 d, and 60 d) after injury. Data were expressed as mean ± SD ($n = 8$ for each group); (b) representative sections of spinal cords in the ventral horn of gray matter stained with cresyl violet at 72 h after injury. Normal neurons exhibited a fine cytoplasm with Nissl substance (arrows); scale bar = 100 μm; (c) quantitative motor neurons counts in the ventral gray matter at 72 h after injury. Data were expressed as mean ± SEM ($n = 3$ for each group). * $P < 0.05$ versus normal group; # $P < 0.05$ versus SCI group.

seven days after withdrawal. MP significantly inhibited the decreases of tissue zinc from 6 h to 1 d. The results suggest that MP SCI could revert the tissue zinc deficiency that existed in SCI rats. So we had to assess changes of serum zinc by atomic absorption spectrometry, corresponding to tissue zinc. Serum zinc level was significantly increased 6 hours later in SCI group. However, it was significantly decreased at

12 h and 18 h (180 um/mL) and the level of zinc returned to baseline zinc level from day 7 after SCI. Serum zinc levels in SCI + MP group were lower than those in SCI groups at different time points (6 h, 12 h, and 18 h) (Figure 3(b)). These results suggest that MP could inhibit the increased serum zinc in SCI rats. To further test zinc transporter we measured ZIP6, ZIP8, and ZIP14 by RT-PCR. Comparing SCI



(a)



(b)

FIGURE 2: Continued.

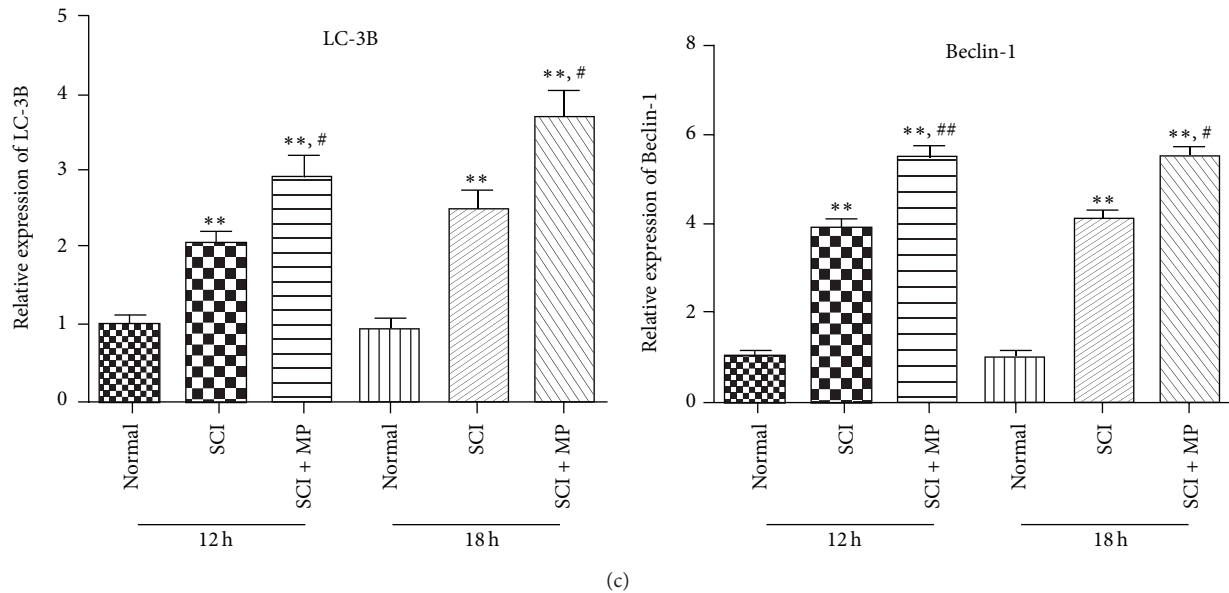


FIGURE 2: MP reduced the activation of microglia in SCI rats. After 12 hours and 18 hours treatment, spinal cord was collected for histological analysis, ELISA and RT-PCR. (a) Immunohistochemistry of Iba1 (brown) in spinal cord at 12 h and 18 h. Scale bar = 200 μ m, 50 μ m; (b), (c) Spinal cord around lesion was subjected to examine the expression of iNOS, IL-6, IL-10, LC-3B and Beclin-1 by RT-PCR. Data were expressed as mean \pm SD ($n = 5$ for each group). * $P < 0.05$, ** $P < 0.01$ versus normal group; # $P < 0.05$, ## $P < 0.05$ versus SCI group.

group with SCI + MP group, only ZIP8 has shown significant difference, which was found to be upregulated in SCI + MP groups compared to SCI groups (Figure 3(c)).

3.4. Microglia Activation Is Inhibited by MP In Vitro. To confirm whether MP could inhibit microglia activation in vitro, by MTT, we first choose a proper concentration of MP on microglia, not influencing cell state and viability after lasting 24 h incubation. The result shows that at concentration of 10 μ M MP has no influence on cell state and viability of microglia. Then we visualized morphology of microglia in each group by immunofluorescence staining of Iba-1. The pictures revealed significant differences in morphology between the groups. In normal group, nonactivated microglia showed long, thin, branched processes. And in LPS group (100 ng/mL LPS alone), microglia undergoing moderate activation had larger somata, thickened proximal processes, and retracted distal processes. Interestingly, in LPS + MP group (100 ng/mL LPS plus 10 μ M MP), we found that microglia, expressing disordered and retracted distal processes, were in poor state, with large somata and nucleus, known as morphology of autophagic cell death (Figure 4(a)). To further confirm effects of MP on inhibiting microglia activation, we used western blot to assess iNOS protein expressions level, after exposing microglia to MP (10 μ M) in LPS induced activation of microglia lasting 12 h, at which the iNOS expression level is the strongest following LPS treatment [30]. The results indicate that MP significantly inhibited LPS induced increase of iNOS proteins (Figure 4(b)). Finally, in the same conditions as described above, we assessed TNF- α , IL-6, and IL-10 cytokine secretion levels in microglia culture medium by ELISA (Figure 4(c)). According to our prospects, protein

expressions of cytokine secretion levels of these cytokines were downregulated in varying degrees.

3.5. Beclin-1 Dependent Autophagic Cell Death Was Induced by MP When Microglia Were under Stress In Vitro. In vitro, we assessed effect of MP on cell viability of microglia by MTT. The results showed that MP did not influence cell viability of microglia when cell state was normal, that MP significantly enhanced the death rate when microglia were under stress, that rapamycin also enhanced the death rate when microglia were under the same stress, and that the death rate of LPS + MP groups was suppressed by 3-MA or TPEN (Figure 5(a)). Then we assessed autophagy through detected LC-3B protein by western blot, which is often used to detect the levels of autophagy. There appeared to be an upregulation of LC-3B in LPS groups. MP + LPS treatment had a more increasing level of LC-3B than LPS groups, which was suppressed following treatment with 3-MA or TPEN (Figure 5(b)). To further evaluate whether the effect of MP on autophagy depended on Beclin-1, Beclin-1 expression of each group was detected via western blot analysis. As shown in Figure 5(c), the expression of Beclin-1 was almost consistent with LC-3B protein expression levels. All of these results suggest that Beclin-1 dependent autophagic cell death was induced by MP.

3.6. MP Upregulates Cellular Labile Zinc Level and ZIP8 and Inhibits NF- κ B. We examined cellular labile zinc changes after microglia were activated. After cells were disposed in the same way as described above, microglia were stained with FluoZin-3-AM, a zinc-specific fluorescent dye. Consistent with our prospects, imaging showed that the concentrations

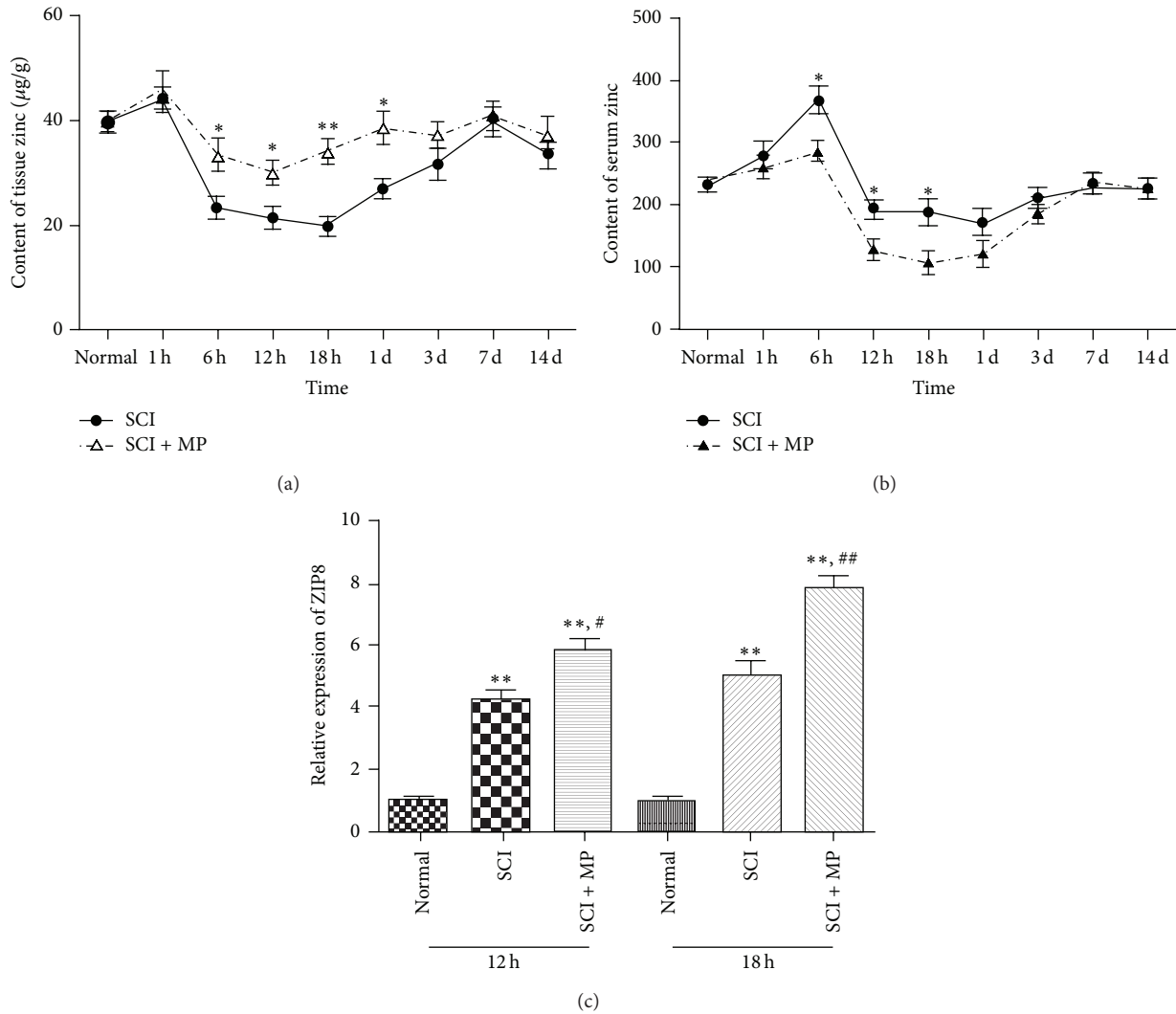


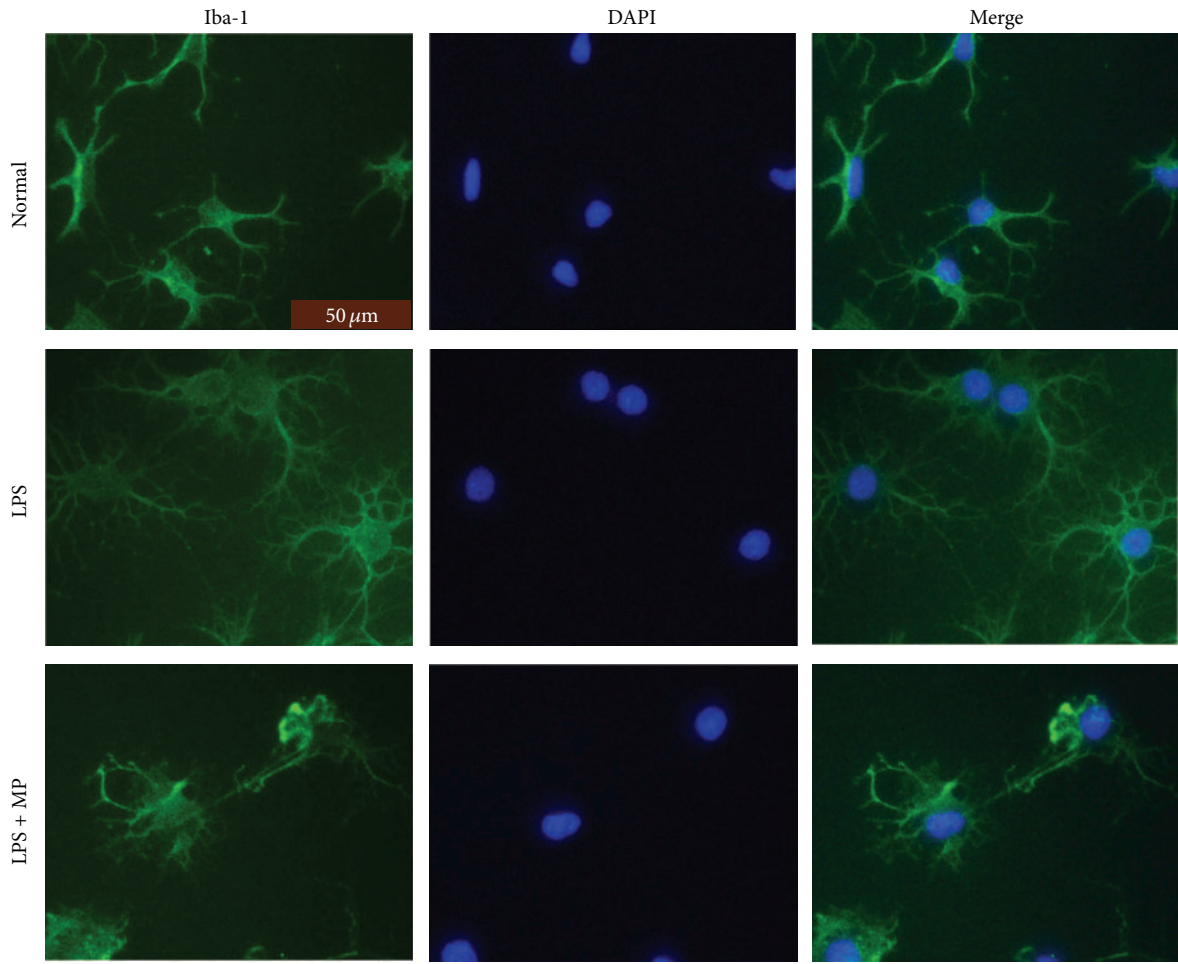
FIGURE 3: Effects of MP on zinc level. Spinal cords around lesions (a) and serum (b) from different time points (1h, 6h, 12h, 18h, 1d, 3d, 7d, and 14d) were used to measure the level of zinc by atomic absorption spectrometry; (c) expression of ZIP8 was detected by RT-PCR at 12h and 18h. Data were expressed as mean ± SEM (*n* = 3 for each group). **P* < 0.05, ***P* < 0.01 versus control group; #*P* < 0.05, ##*P* < 0.01 versus LPS group.

of cellular labile zinc increased in activated microglia after LPS treatment, and that MP administration caused a further increase of concentrations obviously (Figures 6(a) and 6(b)). To test ZIP8 changes, the membrane protein was collected and the expression of ZIP8 was detected by western blot. The results were in accord with the variations of cellular zinc we had found (Figure 6(c)). Recently NF-κβ was reported to be a major inhibitory target of zinc [31, 32]. Hence the protein of NF-κβ in microglia was detected by western blot. The results suggest that LPS induced upregulation of NF-κβ is significantly suppressed by MP (Figure 6(d)).

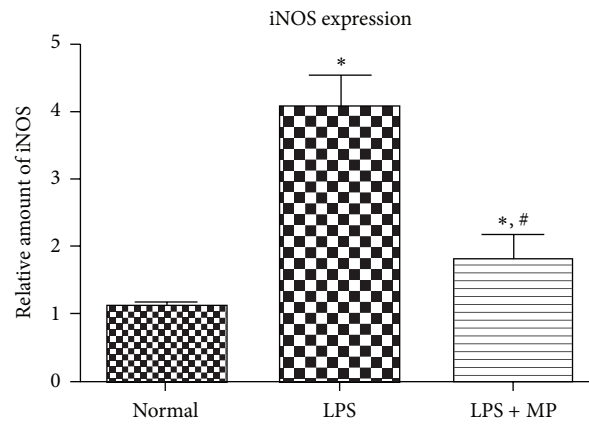
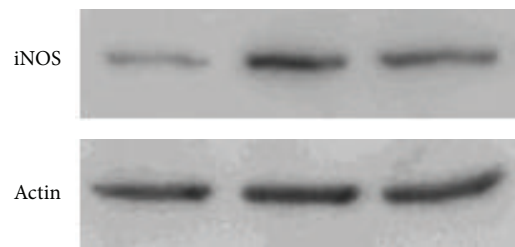
4. Discussion

Indeed, microglia activation is a feature of secondary mechanisms of SCI; some of the properties of that are beneficial, for example, protecting spinal cord from infections

and confining injury regions [33, 34]. However, the excessive and prolonged activation of microglia causes significant damage to neurologic recovery in SCI [35]. A pharmacological intervention on the microglia activation could be a promising therapeutic target. Thus, our result is noteworthy that MP administration obviously reduced density of microglia in injured spinal cord (Figure 2(a)), which was correlated with decreased axonal injury. And in our in vitro studies, we now report that cell viability of microglia was significantly reduced by MP administration when microglia were undergoing activation (Figure 5(a)). Besides, we found that MP + LPS administration resulted in morphology manifestations of disordered and retracted distal processes and in poor state with large somata and nucleus (Figure 4(a)), known as morphology manifestation of autophagic cell death [36]. These results suggest that MP could directly inhibit excessive microglia activation and that the inhibition may be related to autophagic cell death of microglia. Besides, microglia



(a)



(b)

FIGURE 4: Continued.

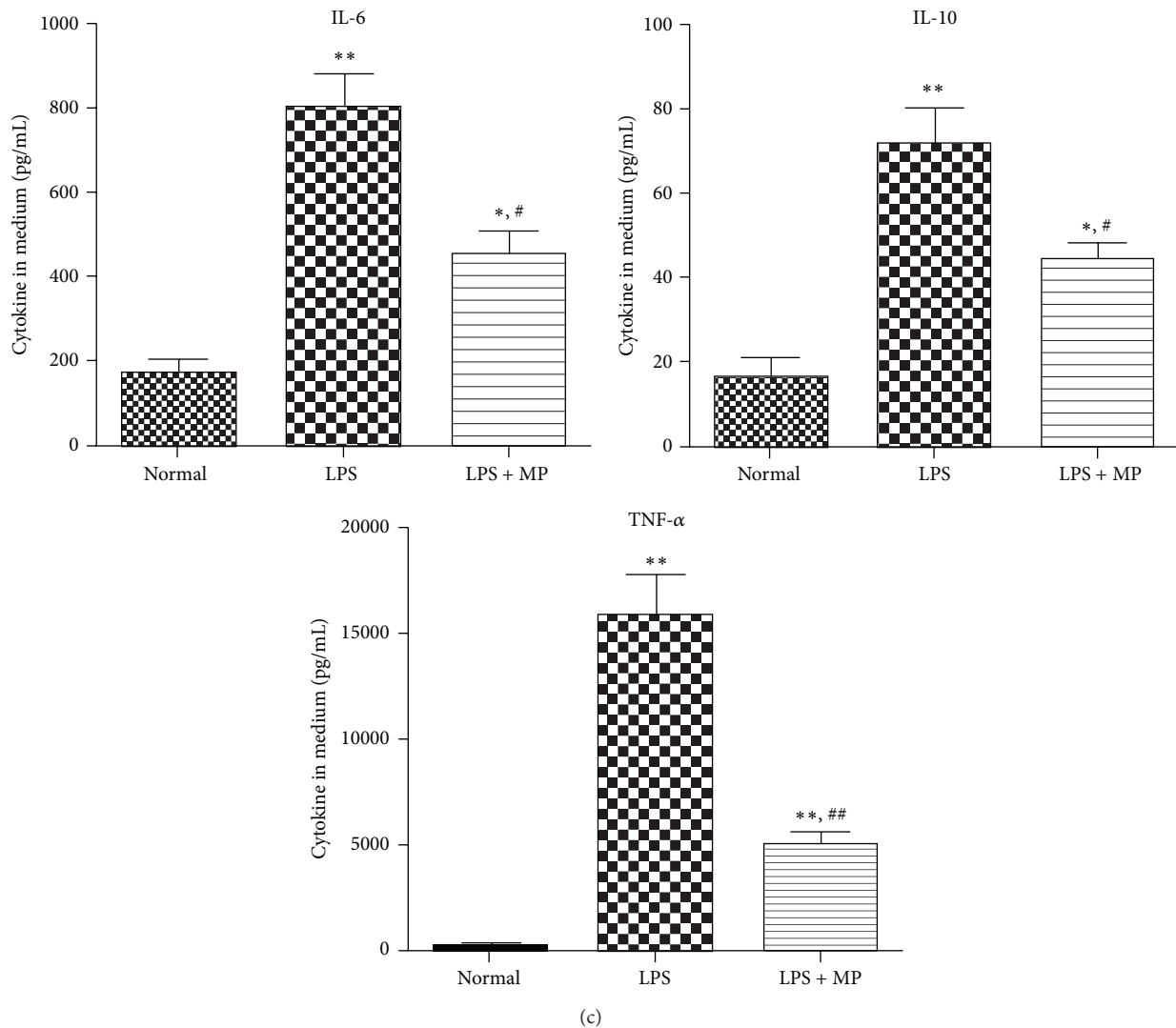


FIGURE 4: Effects of MP on microglia activation and secretion of inflammatory cytokines. (a) The expression of Iba-1 of microglia. After 12 hours of treatment, immunofluorescence staining was performed to assess expression of Iba-1 (Iba-1 green; DAPI blue); scale bar = 50 μ m. (b) After 12 hours of incubation, the expression of protein iNOS in microglia was assessed in LPS group, LPS + MP group, and normal group by western blot. (c) Cytokine levels in culture medium. After 12 hours of treatment, the culture media were collected and expression of IL-6, IL-10, and TNF- α was detected by ELISA kit. Data were expressed as mean \pm SD ($n = 5$ for each group). * $P < 0.05$, ** $P < 0.01$ versus normal group; # $P < 0.05$ versus LPS group.

activation is mainly associated with increased iNOS and proinflammatory cytokines, such as TNF- α , IL-6, and IL-10, which not only are inflammatory markers associated with microglia/macrophages, but also could produce a neuroinflammatory environment [37] and play critical roles in the pathogenesis of SCI [38]. We detected a significant downregulation of proinflammatory molecules iNOS, IL-6, and IL-10 by MP administration following SCI (Figure 2(b)). And in our in vitro studies, MP decreased the protein expression of iNOS and IL-6, IL-10, and TNF- α levels in culture medium in diverse degrees (Figures 4(b) and 4(c)). These results further certify an inhibitory effect of MP administration on the microglia activation and attendant inflammatory molecule production.

As described above, MP may cause autophagic cell death of microglia to inhibit microglia activation. Indeed, whether autophagy is good or bad is argued [39]. Autophagy was upregulated in amyotrophic lateral sclerosis, maybe causing autophagic cell death, which may increase the loss of motor neurons [40]. By contrast, induction of autophagy can induce neuroprotective effects after SCI via inhibition of apoptosis [41]. In the current study, autophagic cell death that occurred in microglia is supposed to be good for SCI, for its inhibition of microglia activation. ATG8/LC3, microtubule-associated protein 1 light chain 3, exists in two forms, as LC-3A and LC-3B. And LC-3B or LC-3B/LC-3A ratio is positive correlation with autophagy [16]. It is also known that autophagy could be divided into Beclin-1 dependent

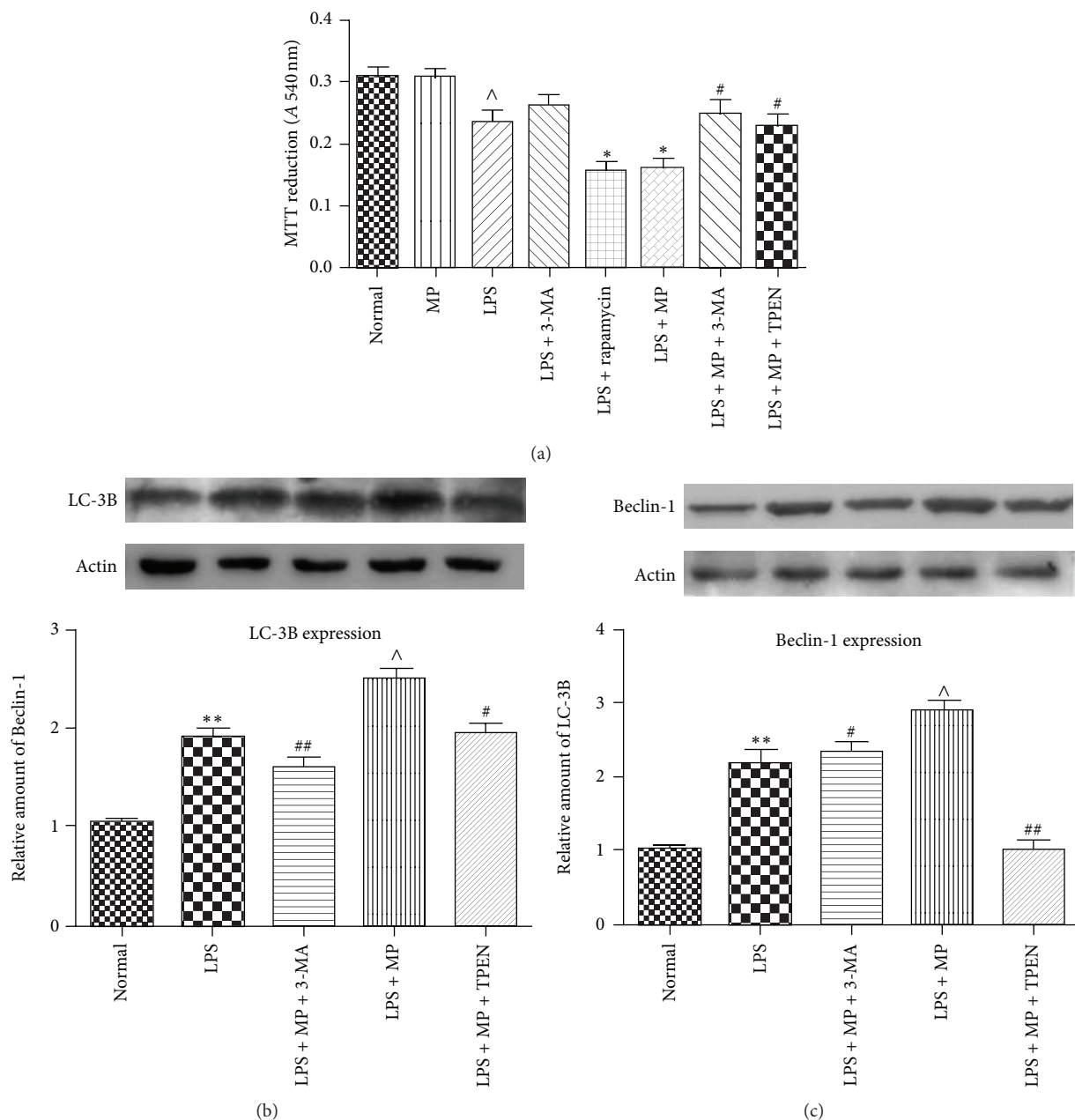


FIGURE 5: MP induced autophagic cell death of microglia in vitro in LPS induced inflammation model. (a) After 12 hours of incubation, cell viability of microglia was measured in normal group, LPS group, LPS + 3-MA group, LPS + rapamycin group, LPS + MP group, LPS + MP + 3-MA group, and LPS + MP + TPEN group by MTT. MTT reductions were expressed as mean \pm SD ($n = 5$ for each group). * $P < 0.05$ versus LPS group; # $P < 0.05$ versus LPS + MP group; ^ $P < 0.05$ versus normal group. (b), (c) After incubation as described above, the expression of LC-3B (b) and Beclin-1 (c) in microglia was assessed by western blot in normal group, LPS group, LPS + MP + 3-MA group, LPS + MP group, and LPS + MP + TPEN group. Relative amounts were expressed as mean \pm SD ($n = 5$ for each group). ** $P < 0.01$ versus normal group; # $P < 0.05$, ## $P < 0.01$ versus LPS + MP group; ^ $P < 0.05$ versus normal group.

and nondependent according to the diverse mechanisms and that Beclin-1 is also associated with the induction of autophagic cell death [42]. Coinciding with our supposition, we have found that expression of both LC-3B and Beclin-1 was upregulated by MP after SCI (Figure 2(c)), which indicated that MP strengthened Beclin-1 dependent autophagy after SCI. But whether autophagy occurs in microglia, or in other

cells of spinal cord except microglia? In in vitro study, we focus on effect of MP on autophagy in microglia. We found that LPS induced increases of both LC-3B and Beclin-1 were significantly upregulated by MP (Figures 5(b) and 5(c)) and that 3-MA, a powerful inhibitor of autophagy now widely used [43], reverted the enhancement caused by MP, which verified our supposition. Actually, the cell viability was

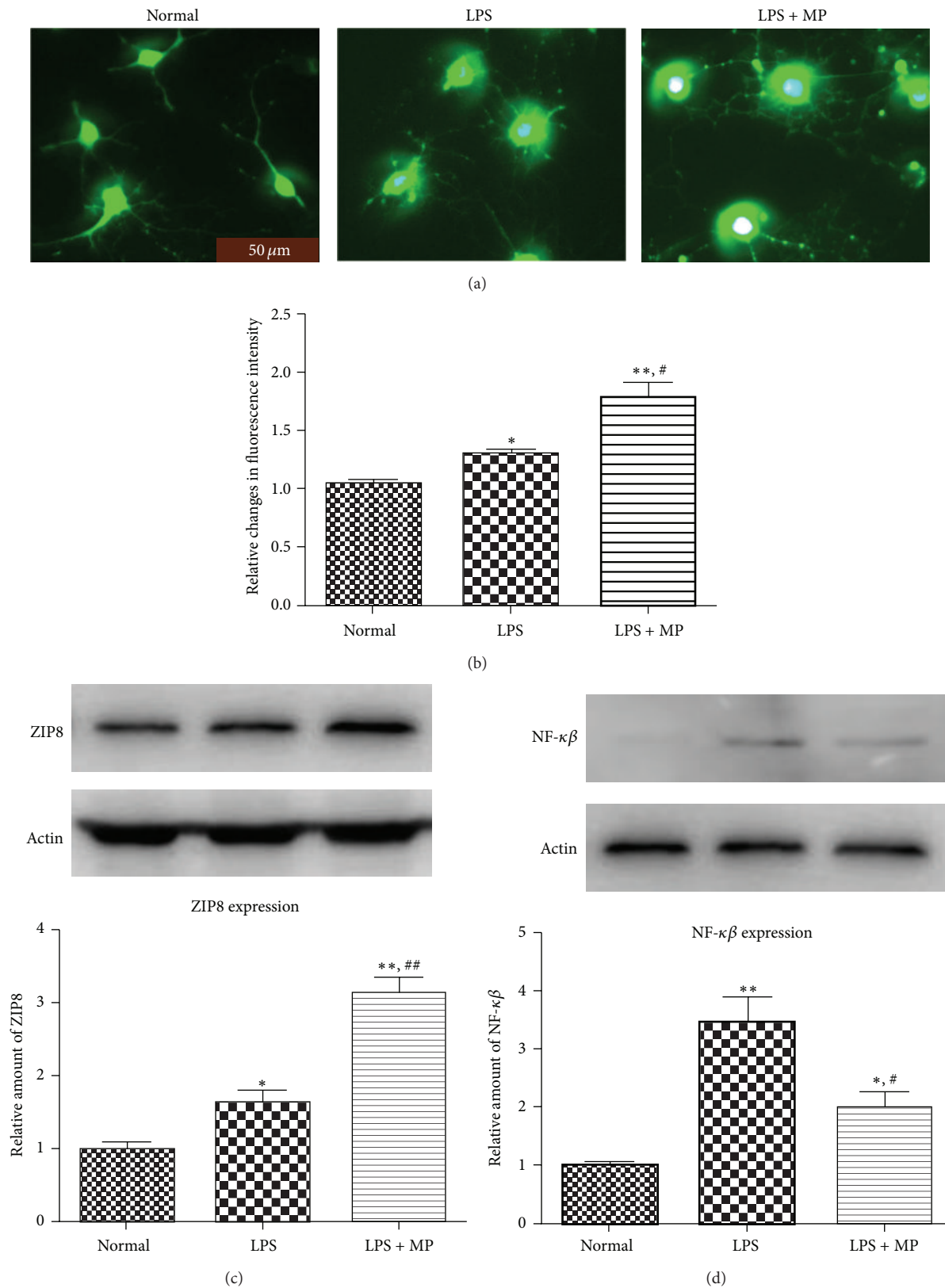


FIGURE 6: Increasing cellular zinc inhibited NF-κβ in microglia. (a) After 12 hours of treatment, microglia were stained with FluoZin-3-AM in normal group, LPS group, and LPS + MP group. Scale bar = 50 μm. (b) The relative fluorescence intensity of zinc. Data were expressed as mean ± SD (n = 5 for each group). *P < 0.05, **P < 0.01 versus normal group; #P < 0.05, versus LPS group. (c) After the same disposition as described above, the membrane protein of microglia was collected and the expression of ZIP8 was detected by western blot. Relative density of ZIP8 was analyzed. Data were expressed as mean ± SEM (n = 3 for each group). (d) After the same disposition as described above, the expression of NF-κβ in microglia was observed by western blot. Data were expressed as mean ± SD (n = 5 for each group). *P < 0.05, **P < 0.01 versus normal group; #P < 0.05, ##P < 0.01 versus LPS group.

reduced by rapamycin in LPS model; comparing LPS group and LPS + rapamycin group, we supposed that autophagic cell death induced by rapamycin may be the main reason of the enhanced cell death and that autophagic cell death later could be induced in LPS model (Figure 5(a)). Furthermore, combining with the results that MP reduced cell viability, compared LPS + MP group to LPS group, and that 3-MA significantly reverted the reduced cell viability of MP, compared LPS + MP group to LPS + MP + 3-MA group, we supposed that autophagic cell death may be main reason of MP reduced cell viability in LPS model (Figure 5(a)). Interestingly, we also have found that there was no statistical difference between LPS + 3-MA group and LPS + 3-MA + MP group; we supposed that 3-MA maybe mostly inhibit the Beclin-1 depended autophagy pathway in LPS + 3-MA + MP group, so MP did not reduce cell viability as like the MP did in LPS + MP group, compared to LPS group (Figure 5(a)). Besides, comparing LPS group and LPS + 3-MA group, there was also no statistical difference, which indicated that LPS induced cell death was not mainly through autophagic cell death (Figure 5(a)). So we suggested that when undergoing stress, autophagic signaling of microglia is activated but the level of autophagy is not enough to cause autophagic cell death and that MP administration could then strengthen the level of autophagy, finally causing autophagic cell death of microglia.

Zinc is greatly associated with autophagy; endogenous zinc plays key role as a trigger in autophagy [44, 45]. In keeping with previous results that MP administration results in a decrease of serum zinc in human [20–22], our findings extend these previous reports by that MP caused a redistribution of zinc from serum to injured spinal cord, resulting in an obvious increase of cellular zinc in injured spinal cord (Figures 3(a) and 3(b)). The importance of zinc redistribution is emphasized in many diseases [46]. Free zinc within cells recently has been ascribed status of neurotransmitter functions, emphasizing the roles of zinc in biology [47]. Hence, combining our current studies, we supposed that effect of MP on autophagy may mainly depend on zinc. Interestingly, at the beginning of SCI, there was an increase of serum zinc in both SCI-only and SCI + MP groups (Figure 3(b)); we suppose that SCI may cause loss of zinc from damage cells or mesenchyme into blood. Besides, after one week, tissue zinc was going to decrease (Figure 3(a)), which suggests that there was a deficiency of zinc after SCI, coinciding with our previous results. Due to the fact that zinc was redistributed by MP to injured spinal cord, we supposed ZIP6, ZIP8, or ZIP14 protein would change in spinal cord tissue, which mainly had a function of transporting zinc inside cells. And we have found that ZIP8 changed greatly and this was coinciding with the variation of serum and tissue zinc (Figure 3(c)). Actually ZIP8 expression is critical in the protection of zinc against tissues damage. It participates in protection of zinc against tn α induced damage [48], deregulation of proinflammatory responses [49], and so on. Combining these results with our in vitro result that MP caused a further increase of ZIP8 (Figure 6(c)), we further suggested that the increased cellular free zinc of microglia after SCI may mainly come from outside, not from inside as we supposed. As

described above, zinc was supposed to be main participant in autophagic cell death of microglia; we test the cellular labile zinc intensity of microglia in vitro. We found that LPS induced an increase in concentrations of cellular labile zinc and that MP administration obviously caused a further increase, maybe mainly through ZIP8. Furthermore, with our results that TPEN, a zinc chelator, reverted the reduced cell viability caused by MP (Figure 5(a)) and that TPEN reduced MP induced enhancement of autophagy (Figures 5(b) and 5(c)), we suggested that increasing concentrations of cellular labile zinc has a key role in autophagic cell death of microglia caused by MP. Besides, recently NF- κ B was reported to be a major inhibitory target of zinc [31, 32]. What is more important is that Ming-Jie Liu reports that cellular zinc increasing was confirmed to cause downregulation of NF- κ B, which was the result of increased ZIP8 expression [49]. According to previous results, we also found that NF- κ B was downregulated after MP treatment (Figure 6(d)). At the same time, currently, there are also advances which have demonstrated that activation of NF- κ B could inhibit autophagy [50]. Hence, we supposed that MP caused concentrations of cellular labile zinc to increase, which may downregulate expression of NF- κ B, which finally results in upregulating autophagy of microglia. More studies should be done to confirm these suppositions.

Both BBB scores (Figure 1(a)) and motor neurons numbers of the anterior horns (Figure 1(c)) were significantly higher in rats treated with MP than the SCI-only rats. Combined with Nissl staining results (Figure 1(b)), these results indicated that autophagic cell death of microglia induced by MP administration protected neuronal locomotor function and enhanced the behavioral recovery of rats after SCI.

Abbreviations

SCI:	Spinal cord injury
BBB scores:	Basso, Beattie, and Bresnahan scores
MP:	Methylprednisolone
Iba-1:	Ionized calcium binding adaptor molecule-1
iNOS:	Inducible nitric oxide synthase
IL-6:	Interleukin-6
IL-10:	Interleukin-10
TNF- α :	Tumor necrosis factor alpha
NF- κ B:	Nuclear factor-kappa beta
LC-3B:	Microtubule-associated protein 1 light chain-3B
ZIP8:	Zinc transport SLC39A8
LPS:	Lipopolysaccharide
TPEN:	Tetrakis(2-pyridylmethyl)ethylenediamine.

Disclaimer

The funders had no role in study design, data collection and analysis, decision to publish, or preparation of the paper.

Conflict of Interests

The authors declare no competing financial interests.

Acknowledgments

This work was supported by the National Natural Science Foundation of China (NSFC) (nos. 81171799, 81471854, and 81300620), Collaborative Fund of Liaoning Province (no. 2013022030), Program for Liaoning Excellent Talents in University (LNET) (nos. LR2014024 and LJQ2014092), and Program for Liaoning Provincial Education Department (no. L2013333). The authors also thank the other researchers who helped them in this study.

References

- [1] J. F. Ditunno Jr. and C. S. Formal, "Chronic spinal cord injury," *New England Journal of Medicine*, vol. 330, no. 8, pp. 550–556, 1994.
- [2] G. Courtine, R. van den Brand, and P. Musienko, "Spinal cord injury: time to move," *The Lancet*, vol. 377, no. 9781, pp. 1896–1898, 2011.
- [3] M. D. Walker, "Acute spinal-cord injury," *The New England Journal of Medicine*, vol. 324, no. 26, pp. 1885–1887, 1991.
- [4] T. B. Ducker, "Treatment of spinal-cord injury," *The New England Journal of Medicine*, vol. 322, no. 20, pp. 1459–1461, 1990.
- [5] N. A. Silva, N. Sousa, R. L. Reis, and A. J. Salgado, "From basics to clinical: a comprehensive review on spinal cord injury," *Progress in Neurobiology*, vol. 114, pp. 25–57, 2014.
- [6] E. D. Hall, "Antioxidant therapies for acute spinal cord injury," *Neurotherapeutics*, vol. 8, no. 2, pp. 152–167, 2011.
- [7] M. B. Bracken, "Treatment of acute spinal cord injury with methylprednisolone: results of a multicenter, randomized clinical trial," *Journal of Neurotrauma*, vol. 8, no. 1, pp. S-47–S-52, 1991.
- [8] J. Xu, Z. X. Qu, E. L. Hogan, and P. L. Perot Jr., "Protective effect of methylprednisolone on vascular injury in rat spinal cord injury," *Journal of Neurotrauma*, vol. 9, no. 3, pp. 245–253, 1992.
- [9] J. E. Pereira, L. M. Costa, A. M. Cabrita et al., "Methylprednisolone fails to improve functional and histological outcome following spinal cord injury in rats," *Experimental Neurology*, vol. 220, no. 1, pp. 71–81, 2009.
- [10] A. Gorio, L. Madaschi, B. Di Stefano et al., "Methylprednisolone neutralizes the beneficial effects of erythropoietin in experimental spinal cord injury," *Proceedings of the National Academy of Sciences of the United States of America*, vol. 102, no. 45, pp. 16379–16384, 2005.
- [11] Y. Tsujimoto and S. Shimizu, "Another way to die: autophagic programmed cell death," *Cell Death and Differentiation*, vol. 12, supplement 2, pp. 1528–1534, 2005.
- [12] C.-J. Lin, T.-H. Chen, L.-Y. Yang, and C.-M. Shih, "Resveratrol protects astrocytes against traumatic brain injury through inhibiting apoptotic and autophagic cell death," *Cell Death & Disease*, vol. 5, no. 3, Article ID e1147, 2014.
- [13] S. Erlich, E. Shohami, and R. Pinkas-Kramarski, "Neurodegeneration induces upregulation of Beclin 1," *Autophagy*, vol. 2, no. 1, pp. 49–51, 2006.
- [14] R. S. Whelan, V. Kaplinskiy, and R. N. Kitsis, "Cell death in the pathogenesis of heart disease: mechanisms and significance," *Annual Review of Physiology*, vol. 72, pp. 19–44, 2009.
- [15] K. Gotoh, Z. Lu, M. Morita et al., "Participation of autophagy in the initiation of graft dysfunction after rat liver transplantation," *Autophagy*, vol. 5, no. 3, pp. 351–360, 2009.
- [16] B. Levine, N. Mizushima, and H. W. Virgin, "Autophagy in immunity and inflammation," *Nature*, vol. 469, no. 7330, pp. 323–335, 2011.
- [17] V. Deretic, T. Saitoh, and S. Akira, "Autophagy in infection, inflammation and immunity," *Nature Reviews Immunology*, vol. 13, no. 10, pp. 722–737, 2013.
- [18] T. Saitoh, N. Fujita, M. H. Jang et al., "Loss of the autophagy protein Atg16L1 enhances endotoxin-induced IL-1 β production," *Nature*, vol. 456, no. 7219, pp. 264–268, 2008.
- [19] M. Scharl and G. Rogler, "Inflammatory bowel disease: dysfunction of autophagy?" *Digestive Diseases*, vol. 30, supplement 3, pp. 12–19, 2013.
- [20] A. A. Yunice, A. W. Czerwinski, and R. D. Lindeman, "Influence of synthetic corticosteroids on plasma zinc and copper levels in humans," *The American Journal of the Medical Sciences*, vol. 282, no. 2, pp. 68–74, 1981.
- [21] R. Scott, B. Ferrie, A. Mc Lelland, and G. S. E. Fell, "The effect of steroid therapy on serum trace metal levels in sub-fertile males," *Urological Research*, vol. 12, no. 4, pp. 213–215, 1984.
- [22] A. Peretz, J. Neve, and J. P. Famaey, "Effects of chronic and acute corticosteroid therapy on zinc and copper status in rheumatoid arthritis patients," *Journal of Trace Elements and Electrolytes in Health and Disease*, vol. 3, no. 2, pp. 103–108, 1989.
- [23] N. V. Rekers, I. M. Bajema, M. J. K. Mallat et al., "Increased metallothionein expression reflects steroid resistance in renal allograft recipients," *American Journal of Transplantation*, vol. 13, no. 8, pp. 2106–2118, 2013.
- [24] S. Yamasaki, K. Sakata-Sogawa, A. Hasegawa et al., "Zinc is a novel intracellular second messenger," *Journal of Cell Biology*, vol. 177, no. 4, pp. 637–645, 2007.
- [25] D. M. Basso, M. S. Beattie, and J. C. Bresnahan, "Graded histological and locomotor outcomes after spinal cord contusion using the NYU weight-drop device versus transection," *Experimental Neurology*, vol. 139, no. 2, pp. 244–256, 1996.
- [26] Z. Li, G.-H. Guo, G.-S. Wang, C.-X. Guan, and L. Yue, "Influence of neural stem cell transplantation on angiogenesis in rats with spinal cord injury," *Genetics and Molecular Research*, vol. 13, no. 3, pp. 6083–6092, 2014.
- [27] S. Tada, T. Okuno, T. Yasui et al., "Deleterious effects of lymphocytes at the early stage of neurodegeneration in an animal model of amyotrophic lateral sclerosis," *Journal of Neuroinflammation*, vol. 8, no. 1, article 19, 2011.
- [28] Y. Wang, R. Su, G. Lv et al., "Supplement zinc as an effective treatment for spinal cord ischemia/reperfusion injury in rats," *Brain Research*, vol. 1545, pp. 45–53, 2014.
- [29] M. K. Mishra, J. Wang, M. B. Keough et al., "Laquinimod reduces neuroaxonal injury through inhibiting microglial activation," *Annals of Clinical and Translational Neurology*, vol. 1, no. 6, pp. 409–422, 2014.
- [30] A. Henn, S. Lund, M. Hedtj rn, A. Schrattenholz, P. P rziggen, and M. Leist, "The suitability of BV2 cells as alternative model system for primary microglia cultures or for animal experiments examining brain inflammation," *Altx*, vol. 26, no. 2, pp. 83–94, 2009.

- [31] S. Vasto, E. Mocchegiani, G. Candore et al., "Inflammation, genes and zinc in ageing and age-related diseases," *Biogerontology*, vol. 7, no. 5-6, pp. 315–327, 2006.
- [32] K. Baruch, L. Gur-Arie, C. Nadler et al., "Metalloprotease type III effectors that specifically cleave JNK and NF- κ B," *The EMBO Journal*, vol. 30, no. 1, pp. 221–231, 2011.
- [33] R. M. Ransohoff and A. E. Cardona, "The myeloid cells of the central nervous system parenchyma," *Nature*, vol. 468, no. 7321, pp. 253–262, 2010.
- [34] A. Nimmerjahn, F. Kirchhoff, and F. Helmchen, "Neuroscience: resting microglial cells are highly dynamic surveillants of brain parenchyma in vivo," *Science*, vol. 308, no. 5726, pp. 1314–1318, 2005.
- [35] K. Saijo and C. K. Glass, "Microglial cell origin and phenotypes in health and disease," *Nature Reviews Immunology*, vol. 11, no. 11, pp. 775–787, 2011.
- [36] H. D. VanGuilder, G. V. Bixler, R. M. Brucklacher et al., "Concurrent hippocampal induction of MHC II pathway components and glial activation with advanced aging is not correlated with cognitive impairment," *Journal of Neuroinflammation*, vol. 8, article 138, 2011.
- [37] M. A. Burguillos, T. Deierborg, E. Kavanagh et al., "Caspase signalling controls microglia activation and neurotoxicity," *Nature*, vol. 472, no. 7343, pp. 319–324, 2011.
- [38] F. M. Bareyre and M. E. Schwab, "Inflammation, degeneration and regeneration in the injured spinal cord: insights from DNA microarrays," *Trends in Neurosciences*, vol. 26, no. 10, pp. 555–563, 2003.
- [39] E. Wirawan, T. Vanden Berghe, S. Lippens, P. Agostinis, and P. Vandenabeele, "Autophagy: for better or for worse," *Cell Research*, vol. 22, no. 1, pp. 43–61, 2012.
- [40] S. Sasaki, "Autophagy in spinal cord motor neurons in sporadic amyotrophic lateral sclerosis," *Journal of Neuropathology & Experimental Neurology*, vol. 70, no. 5, pp. 349–359, 2011.
- [41] L. Zhang, P. Tang, H. Hou et al., "Autophagy reduces neuronal damage and promotes locomotor recovery via inhibition of apoptosis after spinal cord injury in rats," *Molecular Neurobiology*, vol. 49, no. 1, pp. 276–287, 2014.
- [42] T. Diskin, P. Tal-Or, S. Erlich et al., "Closed head injury induces upregulation of beclin 1 at the cortical site of injury," *Journal of Neurotrauma*, vol. 22, no. 7, pp. 750–762, 2005.
- [43] C. Takatsuka, Y. Inoue, K. Matsuoka, and Y. Moriyasu, "3-Methyladenine inhibits autophagy in tobacco culture cells under sucrose starvation conditions," *Plant and Cell Physiology*, vol. 45, no. 3, pp. 265–274, 2004.
- [44] J. P. Liuzzi and C. Yoo, "Role of Zinc in the regulation of autophagy during ethanol exposure in human hepatoma cells," *Biological Trace Element Research*, vol. 156, no. 1–3, pp. 350–356, 2013.
- [45] S.-J. Lee, K. S. Cho, and J.-Y. Koh, "Oxidative injury triggers autophagy in astrocytes: the role of endogenous zinc," *Glia*, vol. 57, no. 12, pp. 1351–1361, 2009.
- [46] M. Foster and S. Samman, "Zinc and Regulation of inflammatory cytokines: implications for cardiometabolic disease," *Nutrients*, vol. 4, no. 7, pp. 676–694, 2012.
- [47] C. J. Frederickson, J.-Y. Koh, and A. I. Bush, "The neurobiology of zinc in health and disease," *Nature Reviews Neuroscience*, vol. 6, no. 6, pp. 449–462, 2005.
- [48] B. Besecker, S. Bao, B. Bohacova, A. Papp, W. Sadee, and D. L. Knoell, "The human zinc transporter SLC39A8 (Zip8) is critical in zinc-mediated cytoprotection in lung epithelia," *The American Journal of Physiology—Lung Cellular and Molecular Physiology*, vol. 294, no. 6, pp. L1127–L1136, 2008.
- [49] M.-J. Liu, S. Bao, M. Gálvez-Peralta et al., "ZIP8 regulates host defense through zinc-mediated inhibition of NF- κ B," *Cell Reports*, vol. 3, no. 2, pp. 386–400, 2013.
- [50] T. G. Sommermann, H. I. D. Mack, and E. Cahir-McFarland, "Autophagy prolongs survival after NF κ B inhibition in B-cell lymphomas," *Autophagy*, vol. 8, no. 2, pp. 265–267, 2012.

Review Article

Nanoparticle Probes for Structural and Functional Photoacoustic Molecular Tomography

Haobin Chen,^{1,2} Zhen Yuan,² and Changfeng Wu¹

¹State Key Laboratory on Integrated Optoelectronics, College of Electronic Science and Engineering, Jilin University, Changchun, Jilin 130012, China

²Bioimaging Core, Faculty of Health Sciences, University of Macau, Taipa, Macau

Correspondence should be addressed to Zhen Yuan; zhenyuan@umac.mo and Changfeng Wu; cwu@jlu.edu.cn

Received 28 October 2014; Revised 11 December 2014; Accepted 11 December 2014

Academic Editor: Weibo Cai

Copyright © 2015 Haobin Chen et al. This is an open access article distributed under the Creative Commons Attribution License, which permits unrestricted use, distribution, and reproduction in any medium, provided the original work is properly cited.

Nowadays, nanoparticle probes have received extensive attention largely due to its potential biomedical applications in structural, functional, and molecular imaging. In addition, photoacoustic tomography (PAT), a method based on the photoacoustic effect, is widely recognized as a robust modality to evaluate the structure and function of biological tissues with high optical contrast and high acoustic resolution. The combination of PAT with nanoparticle probes holds promises for detecting and imaging diseased tissues or monitoring their treatments with high sensitivity. This review will introduce the recent advances in the emerging field of nanoparticle probes and their preclinical applications in PAT, as well as relevant perspectives on future development.

1. Introduction

PAT, as an emerging powerful modality, has the capability to image the structural and functional information of biological tissues with high resolution and satisfactory imaging depth [1–4]. In PAT, a nonionizing short-pulsed laser source is generally used to illuminate the biological tissues. After the irradiated tissues absorb the light energy, the acoustic waves are produced due to thermoelastic expansion. The acoustic pressure distributions along the tissue surfaces are detected by ultrasound transducers, which can be utilized to generate the functional or structural photoacoustic images. PAT is able to image the optical properties, physiological parameters including deoxyhemoglobin and oxyhemoglobin concentrations, and mechanical parameters such as acoustic velocity of biological tissues. Interestingly photoacoustic molecular imaging can be used to detect biomarkers and reveal specific tumor cells or gene expression [5–8].

PAT based on intrinsic contrast is dominated by the endogenous agents of biological tissues such as hemoglobin, melanin, and water [9]. As a result, the imaging accuracy of PAT for diseased tissues is governed by these contrasts. For example, the diseased tissues scatter or absorb lights

differently from those of healthy ones and another noticeable distinction between the two lies in respective background noise. However, the intrinsic optical contrast is probably not sufficient and in many cases may not be disease-specific. As such, it is essential to use the exogenous contrast agents which have some kinds of affinity for the diseased areas via a chemical interaction within the tissues, which is able to provide sensitive and disease-specific detection or monitoring. The use of photoacoustic exogenous agents has the capability of significantly improving the imaging sensitivity, which will greatly extend PAT's applications to areas such as deep-tissue imaging, cell-specific contrast, and molecular imaging [10–13].

In recent years nanoparticle probes have tremendously impacted scientific researches in biomedical imaging, biological diagnostics, and disease treatments [14]. In comparison with other contrast agents, nanoparticles have their very unique merits: (1) the functional properties are able to be tailored via varying their compositions, structures, sizes, and shapes; (2) the huge specific surface area as well as the quantum confinement effect in some systems bestows crucial properties for the preclinical animal study; and (3) the surface of nanoparticle probes is able to be modified to have different functions for multimodality molecular imaging.

To date, different types of nanoparticle probes, including metal (typically Au or Ag) nanoparticles, carbon nanotubes, and superparamagnetic iron oxide nanoparticles as well as semiconductor quantum dots, have been synthesized and adopted for different biomedical applications [15–24]. PAT combined with nanoparticle contrast agents can provide unique structural and functional information at unprecedented levels. For the mini review, the recent advances in the development of nanoparticle probes in PAT are first summarized. To date, inorganic nanoparticles, such as gold nanostructures, carbon nanotubes, iron oxide, semiconductor quantum dots, and upconversion nanoparticles [20], are successfully applied in PAT as contrast agents. In addition, this work also introduces the recent progress in organic nanoparticles such as semiconducting polymer dots that show improved performance in structural and functional photoacoustic molecular tomography.

2. Inorganic Nanoparticle Probes for PAT

2.1. Metal Nanostructures. Metal nanoparticles have been employed for photoacoustic molecular tomography because of the biocompatibility, easy modification for targeting, minimized toxicity, and localized surface plasmon resonance peak as well as enhanced optical signals in near-infrared spectral regions [25–27]. In addition, while the intrinsic fluorescence signals from metal nanoparticles are not very strong, certain types of metal clusters and nanoparticles can be employed for fluorescent imaging or PAT. So far six types of metal nanostructures have been utilized as nanoparticle probes for PAT in vivo tests, including nanospheres [28, 29], nanorods [30, 31], nanocages [32], nanoshells [33], nanobeacons [34], and nanoplates [35]. The basic preparation and in vivo and in vitro investigations for gold nanostructures in PAT have been described in detail by previous work [3]. Here we only focus on its recent advances in biomedical fields. It is widely recognized that the determination of tumor margin during the surgical resection is essential for the prevention of tumor recurrences [36, 37]. Kircher et al. have used gold nanospheres for both PAT and surface-enhanced Raman spectroscopy (SERS). Their results revealed that multimodal molecular imaging (MRI-PAT-SERS) using the multifunctional nanoprobe can help quantify the tumor margins of living mice with high accuracy [38]. In addition, gold nanorods (GNRs) have several advantages that motivate their biomedical applications for PAT [39–41]. For example, GNRs have enhanced optical absorption cross section, which is able to generate strong photoacoustic signals and produce minimized uptakes within the reticuloendothelial systems. Accordingly, molecular imaging agents using the nanorods as a passively targeted probe were proposed, in which the probes allowed for presurgical tumor imaging for locoregional staging by PAT and intraoperative imaging of tumor margins to remove the tumors completely by SERS [31].

Nanoshells, particularly gold nanoshells, have been demonstrated as valuable vehicles for ex vivo and pre-clinical studies. Nanoshells coated with polyethylene glycol (PEG) can improve the biocompatibility and the circulating lifetime through the animal body. Nanoshells have been

used as an intravascular contrast agent for optical coherence tomography (OCT) and PAT to identify the vascular structures of the brains [1]. Nanoshells can be conjugated to certain biomolecules that allow for specific targeting to malignant tumors because the protocol utilized to conjugate biomolecules to the surface of the gold has been well established. Nanoshells can also provide the early detection of diseases and can be used as tools for the treatment of disorders or diseases, which includes the use of hollow structures as carriers of different antitumor drugs, the development of scattering nanoshells as nanoprobe for OCT, and the implementation of absorbing nanoshells in near-infrared thermal therapy of tumors [42].

2.2. Carbon Nanotubes. Single-walled carbon nanotubes have been extensively investigated and used as nanoparticle probes for photoacoustic molecular tomography [17, 43–45]. The broad absorption spectrum of single-walled carbon nanotubes (SWCNTs) can cover the optical window of biological tissue, therefore yielding a strong photoacoustic signal. de La Zerda et al. demonstrated that SWCNTs conjugated with cyclic Arg-Gly-Asp peptides can be adopted as nanoparticle probes for photoacoustic molecular imaging of cancers [17]. The photoacoustic signals from the targeted nanotubes in mice bearing tumors were found to be eight times higher than that from the nontargeted ones. In addition, SWCNTs can be further modified to improve their performance for PAT. For instance, Indocyanine Green dye enhanced SWCNTs (SWNT-ICG) were proposed to generate photoacoustic signals that can provide a remarkably high optical contrast for in vivo animal study [21]. In particular, the ultrahigh surface area of the nanotubes has highly efficient loading of aromatic molecules such as ICG on the nanotube surface, which can create a new sort of photoacoustic probes including SWNT-ICG-RGD (Figure 1(a)). The optical absorption spectrum for the novel SWNT-ICG nanoparticles shows that the SWNT-ICG particles can perform a 20-fold higher absorbance at its peak absorbance (780 nm) when compared to plain SWCNTs (Figure 1(b)). They also built a nonabsorbing and nonscattering agarose phantom with inclusions of SWNT-ICG-RGD with increased concentrations from 0.5 nM to 121.5 nM. They found that the photoacoustic signals generated by the SWNT-ICG-RGD particles correlated well with the nanoparticle concentrations (Figure 1(c)). Finally, they also revealed that the new nanoparticle probes could detect cancer cells 20 times fewer than those by previously reported SWCNTs [21].

2.3. Superparamagnetic Iron Oxide Nanoparticles. Superparamagnetic iron oxide nanoparticles (SPIONs) are FDA approved nanoprobe for MRI, which can also be used for nanoparticles probes for photoacoustic molecular tomography due to their perfect biosafety profiles [18, 46–49]. For example, recent work revealed that the contrast agents composed of SPIONs cores coated with silica showed their potentials as nanoparticle probes for PAT when irradiated with 1064 nm laser sources [46]. For this work, they employed a modulated continuous wave laser to access the maximum depth characterization of silica-coated SPION and they also tested the optical stability of the nanoprobe within different

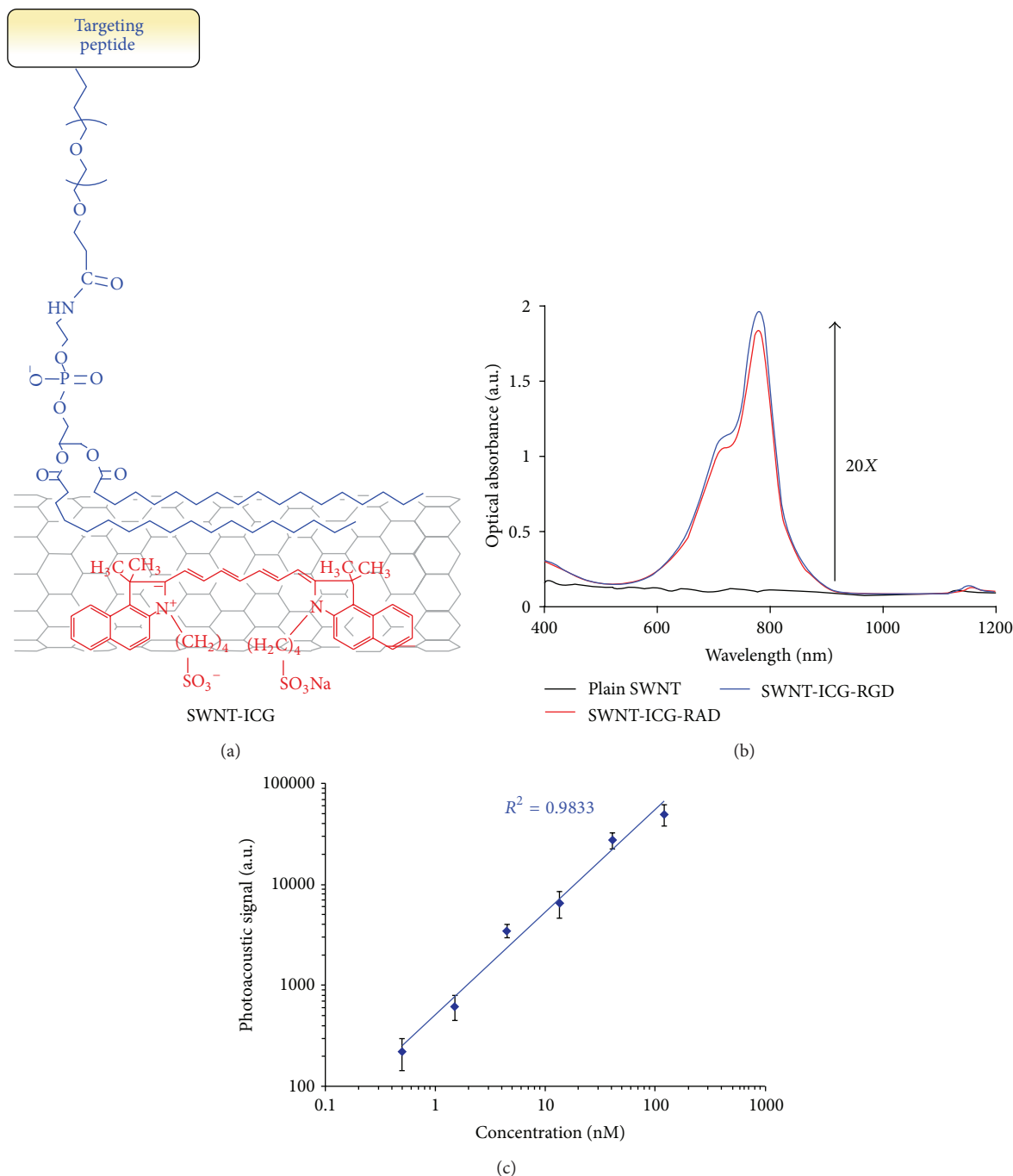


FIGURE 1: ICG dye-enhanced SWNT probes for photoacoustic imaging. (a) A schematic of a SWNT-ICG particle with ICG molecules (red) attached to the SWNT surface via noncovalent π - π stacking bonds. The targeting peptide was attached to SWNT via a PEGylated phospholipid. (b) The absorption spectra from different probes including SWNT-ICG-RAD (red), plain SWNT (black), and SWNT-ICG-RGD (blue). The absorption intensity of ICG dye-SWNTs particles was much higher (over 20 times) than that of plain SWNT at 780 nm. The absorption spectra between SWNT-ICG-RAD and SWNT-ICG-RGD were very similar, which validated that the peptide conjugation should not significantly perturb the photoacoustic signal. (c) The photoacoustic signals of SWNT-ICG was proportional to the probe concentrations ($R^2 = 0.9833$). Reproduced with permission from [21].

solvents in PAT. Importantly they found that the minimum detectable concentration of the silica-coated SPION at depths of 5 mm and 10 mm inside the intralipid was ~ 0.17 and ~ 0.23 mg/mL, respectively [46].

2.4. Quantum Dots. Quantum dots (Qdots) generally refer to semiconductor nanocrystals when the physical dimensions are much smaller than the exciton Bohr radius [50, 51]. Unlike bulk counterparts, these tiny structures exhibit broad

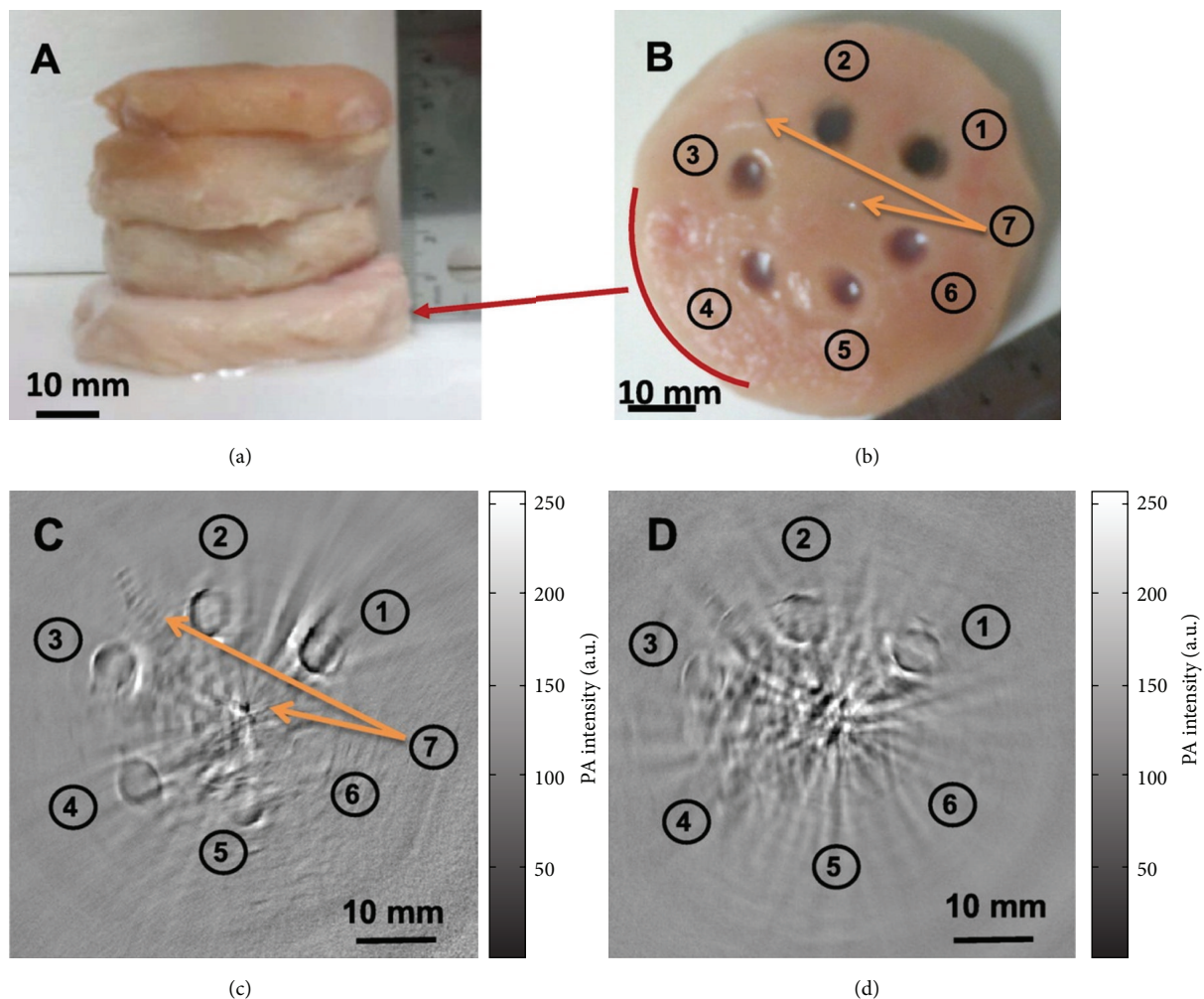


FIGURE 2: Photoacoustic molecular tomography of deep-embedded targets based on CuS Qdot probes. The agarose gels that contained CuS Qdots were placed in the background of chicken breast muscle with different chicken breasts stacked. (a) showed the configuration of chicken breast muscle stacked. (b) Photograph of chicken breast muscle that had the targets with CuS Qdots of (1) 100 $\mu\text{g}/\text{mL}$ (2 OD), (2) 50 $\mu\text{g}/\text{mL}$ (1 OD), (3) 25 $\mu\text{g}/\text{mL}$ (0.5 OD), (4) 12.5 $\mu\text{g}/\text{mL}$ (0.25 OD), (5) 6.25 $\mu\text{g}/\text{mL}$ (0.125 OD), (6) gel without contrast agent, and (7) two needle tips at the center and 11 o'clock position. The photoacoustic image was shown at the bottom low with a depth of (c) 25 mm and (d) 50 mm. Reproduced with permission from [22].

excitation spectra which range from ultraviolet to near-infrared regions and discrete energy levels that are determined primarily by their sizes and chemical compositions [52, 53]. When compared to organic dyes or fluorescent proteins, Qdots exhibit several important properties including high absorption coefficients and enhanced photostability [54]. Due to the wide absorption bands and narrow emission bands, Qdots are considered as extraordinary contrast agents for fluorescence imaging and multiplexed detections [55]. Importantly, the large surface area of Qdots enables the design of multifunctional probes for multimodal molecular imaging. Qdots are playing an essential role as versatile labels for biomedical imaging. Interestingly, Qdots are also used as nanoparticle probes for PAT [19, 56, 57]. For example, Shashkov et al. demonstrated the applications of Qdots in PAT and photothermal microscopy [19]. By using a nanosecond pulsed laser, the bubble formation phenomena

were performed using an advanced multifunctional microscope that integrated fluorescence and photoacoustic and photothermal imaging. They found that Qdots can be used as multifunctional contrast agents and sensitizers for multimodal molecular imaging and photothermal therapy [19].

Semiconductor copper sulfide (CuS) has received extensive attention for its applications in catalysis and photovoltaics. Recently different gold nanostructures have been developed for the combination applications of PAT and chemotherapy [58, 59]. However, the near-infrared absorbance peaks of gold nanostructures, such as GNRs, would disappear after 1h laser irradiation at a low power density [60]. Interestingly, the near-infrared absorption of CuS Qdots, derived from the d-d transition of Cu^{2+} ions, seldom changes with their morphologies [61]. A few modalities have been implemented for the development of CuS Qdots [62, 63]. For example, Zhou et al. conducted

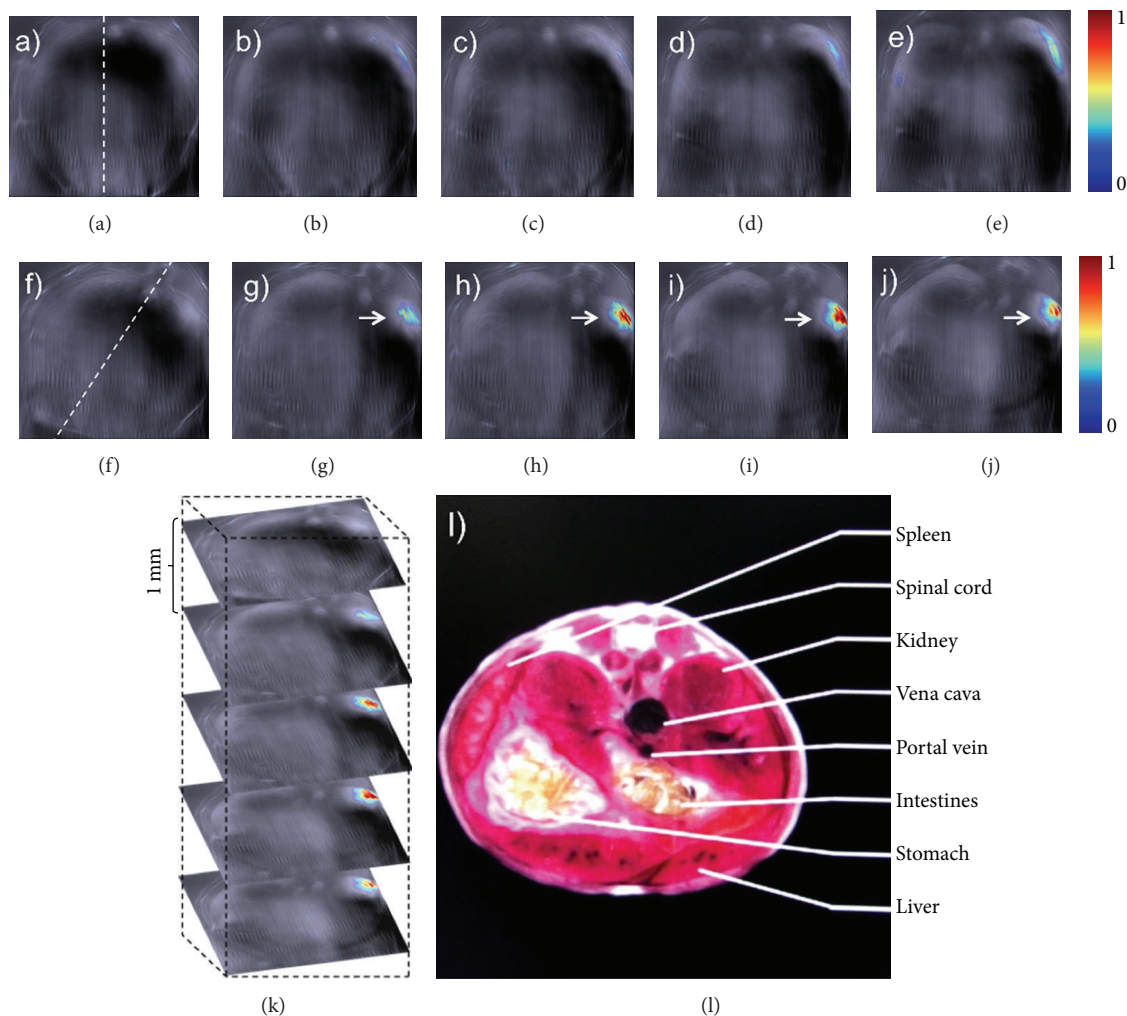


FIGURE 3: Photoacoustic molecular imaging of mice in vivo based on the lanthanide upconversion nanoparticles (UC- α -CD). ((a)–(e)) Generated slice images of live mice before UC- α -CD injection. ((f)–(j)) 35 minutes after injection. Dashed lines in (a) and (f) displayed positions of the mouse while (g)–(j) showed the localized UC- α -CD. (k) 3D rendering of scanned region. (l) Schematic sections related to analysis region. Reproduced with permission from [20].

thioglycolic acid-stabilized CuS Qdots and showed their application for photothermal destruction of tumor cells in vitro using a near-infrared laser beam [64]. They also found that the absorption peak could be tuned toward longer wavelengths by simply adjusting the stoichiometric ratio between CuCl_2 and Na_2S [22]. In their study, the average diameter of the CuS Qdots was 11 nm and the molar absorption coefficient at 1064 nm was estimated to be $2.6 \times 10^7 \text{ cm}^{-1} \text{ M}^{-1}$. The strongest absorption peak at 1064 nm implies that CuS Qdots are encouraging entrant for PAT contrast enhancement. Employing a Nd:YAG laser at a wavelength of 1064 nm for PA excitation, PAT clearly visualized CuS Qdots in mouse brain and rat lymph nodes. Furthermore, agarose gel containing CuS Qdots embedded in chicken breast at a depth of $\sim 5 \text{ cm}$ could be promptly imaged with an in-plane imaging resolution of $\sim 800 \mu\text{m}$ and a sensitivity of $\sim 0.7 \text{ nmol}$ per imaging voxel (Figure 2). Their work showed that it is possible to image lesions in the human breast at a depth of up to 40 mm with imaging resolution and

sensitivity similar to that attained with CuS Qdots in chicken breast muscles. Besides the breast, lesions located in other anatomic sites such as the skin, arm or leg, head and neck, and lymph nodes may also be detected with the next generation of PAT devices equipped with more powerful 1064 nm lasers and a more sensitive ultrasonic detection array.

2.5. Upconversion Nanoparticles. Recently upconversion nanoparticles (UCNPs) such as NaYF_4 codoped with lanthanide ions have been developed as potential nanoparticle probes for biomedical imaging [65, 66]. Maji et al. found that the $\text{NaYF}_4:\text{Yb}^{3+}, \text{Er}^{3+}$ UCNPs with α -cyclodextrin (UC- α -CD) in aqueous conditions were able to exhibit luminescence quenching when excited at 980 nm. The nonradiative relaxation can result in an unprecedented and high photoacoustic signal. In vivo localization of UC- α -CD was conducted using PAT in live mice (Figure 3) [20]. The luminescence quenching of UC- α -CD in aqueous solution due to nonradiative relaxation of the excited states will generate intrinsic heat

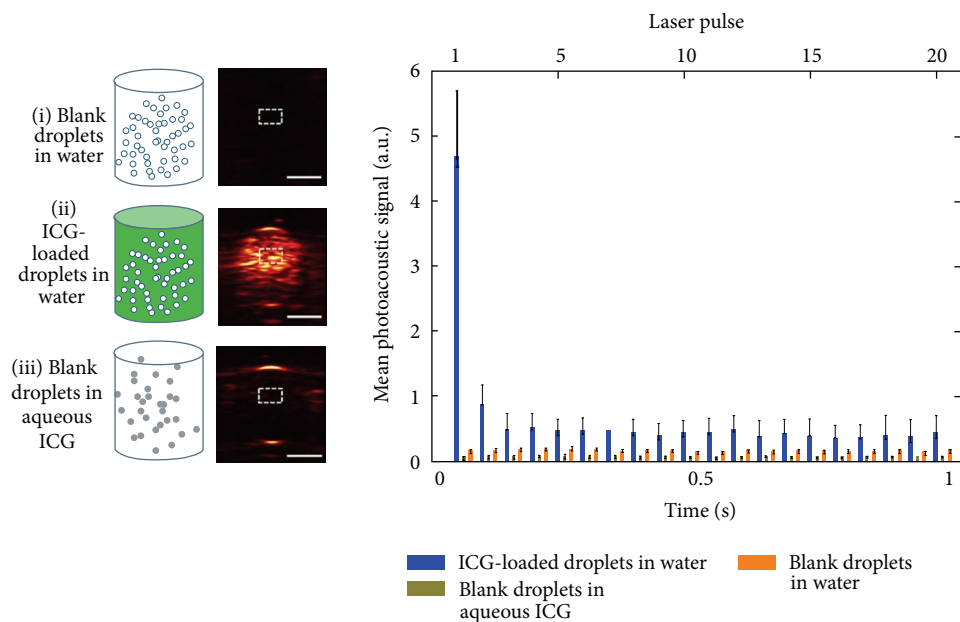


FIGURE 4: Photoacoustic molecular imaging of ICG-loaded droplets. (i) Blank droplets in water, (ii) ICG-loaded droplets in water, and (iii) blank droplets in aqueous ICG. The right panel plotted the mean photoacoustic intensity identified in the defined ROI. Error bar represents the mean \pm standard deviation. $N \geq 3$ for all reported values; scale bar = 2 mm. Reproduced with permission from [23].

generation during the upconversion process under 980 nm excitation. UC- α -CD has been identified to be noncytotoxic and suitable for in vivo PAT as shown by cytotoxicity studies. Figure 3 presented the photoacoustic images generated in real time before and 35 min after intravenous injection of UC- α -CD in the thoracic region of the anesthetized mouse. Contrast enhancement was observed for the images before and after injection. It was also found from the reconstructed images in Figure 3 that, compared to other contrast agents, the developed UC- α -CD material has the advantages of easy preparation, sharp emission bandwidth, long lifetime, high photostability, low biotoxicity, and more importantly less background autofluorescence [67–70], which makes it an excellent nanoparticle probe for PAT.

3. Organic Nanoparticle Probes for PAT

3.1. Indocyanine Green-Loaded Photoacoustic Nanodroplets. Over the last few years, perfluorocarbon (PFC) nanodroplets have been developed into powerful probes for optical molecular imaging as well as image-guided treatments [71, 72]. For instance, high-intensity ultrasound pulses have been used to generate gas microbubbles according to the phase transitions of liquid PFC. Newly, PFC nanodroplets with encapsulated plasmonic nanoparticles were developed as probes for PAT [73]. In terms of accelerated clinical translation, Hannah et al. developed ICG-loaded PFC nanodroplets, which are identified as nontoxic, biocompatible, and safe materials [23]. The contrast enhancement via droplet vaporization was observed for PAT after the initial laser pulse, and the mean signals were determined over several pulses (Figure 4). They also evaluated the quality enhancement of PAT via

the analysis of imaging contrast. Upon irradiation, the PA image contrast was 36 (au), and the contrast-to-noise ratio (CNR) was 51 dB when compared to the 1.1 (au) and 19 dB from blank droplets. They also investigated how the increased ambient temperature would affect the change of PAT imaging contrast. They found that, with increased temperatures, the nanodroplets will generate enhanced photoacoustic signals upon vaporization.

3.2. Semiconductor Polymer Dots. Semiconducting polymer nanoparticles (Pdots or SPNs) have recently generated tremendous interests as a novel class of contrast agents for biological imaging [74]. They exhibit several important virtues such as their extraordinary fluorescence brightness, fast emission rate, excellent photostability, and nonblinking and nontoxic features [75–81]. In particular, we recently developed several influential approaches for introducing functional groups, controlling the surface chemistry of Pdots, and employing these novel nanoparticle probes for cellular labeling and in vivo imaging [82–84]. These superior properties of Pdots over other fluorescent probes have established their enormous potential in biology and medicine as highly bright in vitro and in vivo probes.

Pu et al. have developed a new class of near-infrared SPN probes for in vivo photoacoustic molecular imaging [24]. SPN can generate stronger signals than SWCNTs or GNRs on a per mass basis, permitting whole-body lymph node photoacoustic mapping in living mice at a low systemic injection mass. Semiconducting polymers have been originally developed for a wide variety of optoelectronic devices. These purely organic SPNs for PAT have a unique set of advantages that derive from the light-harvesting polymers including the large mass

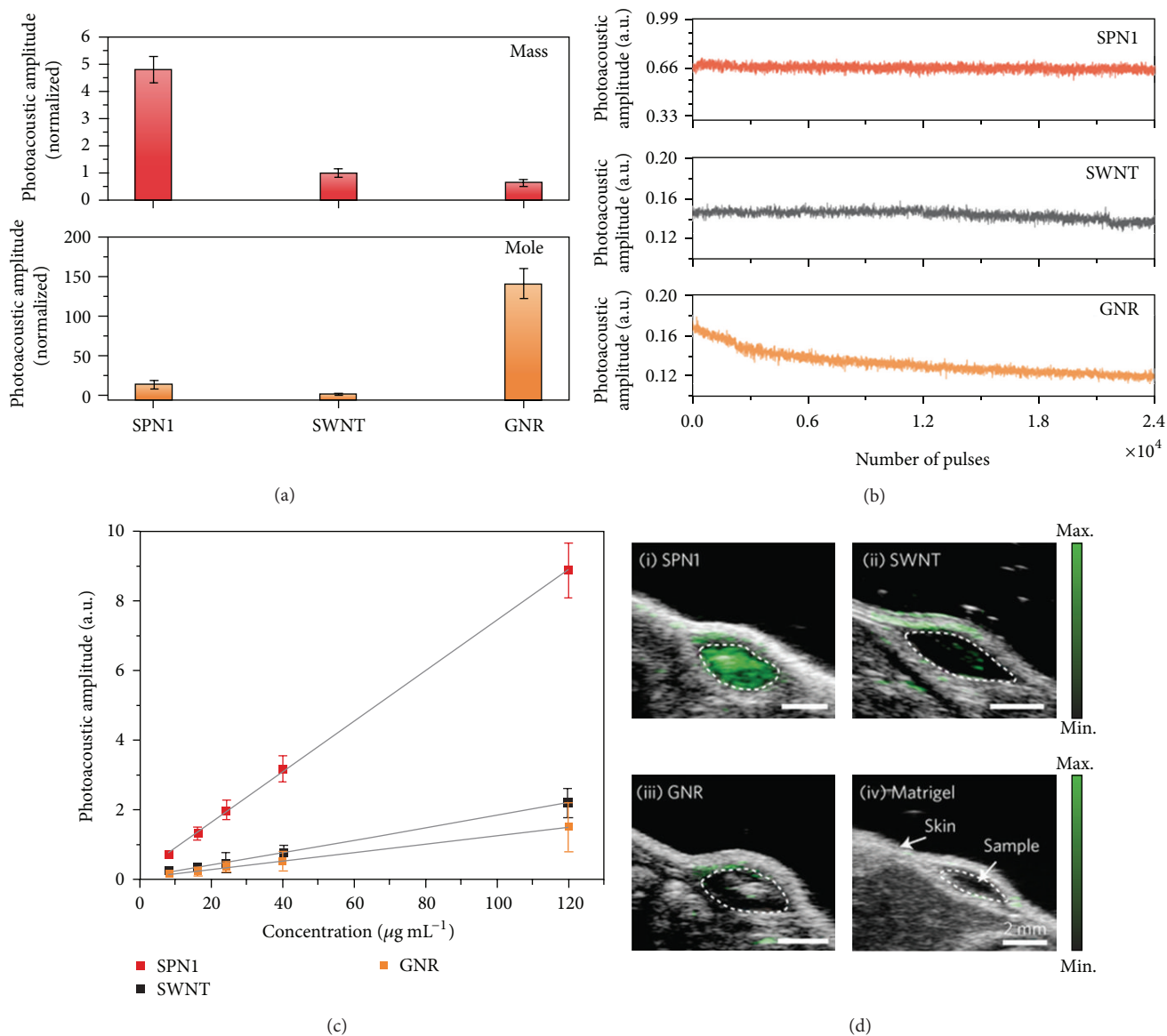
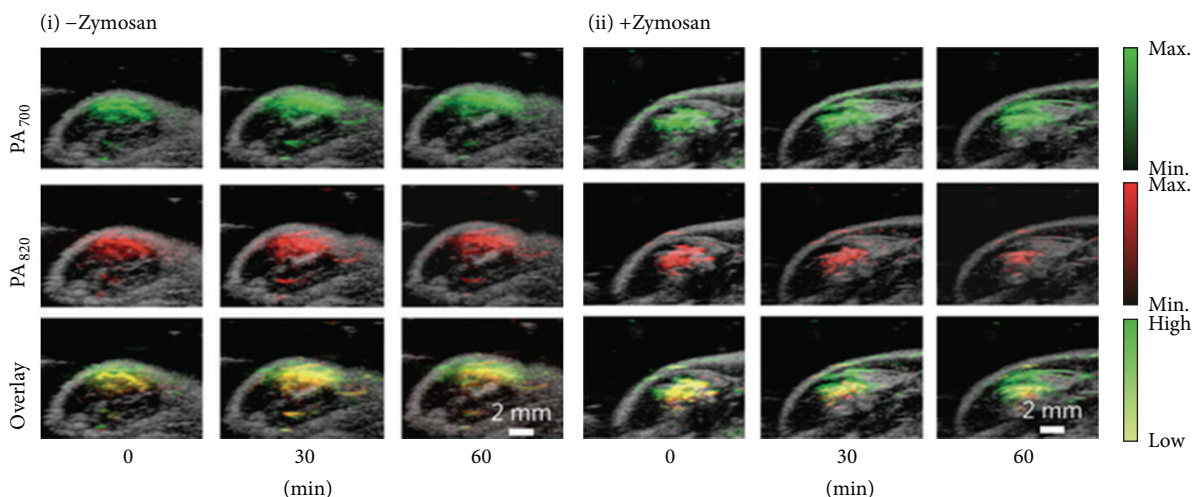


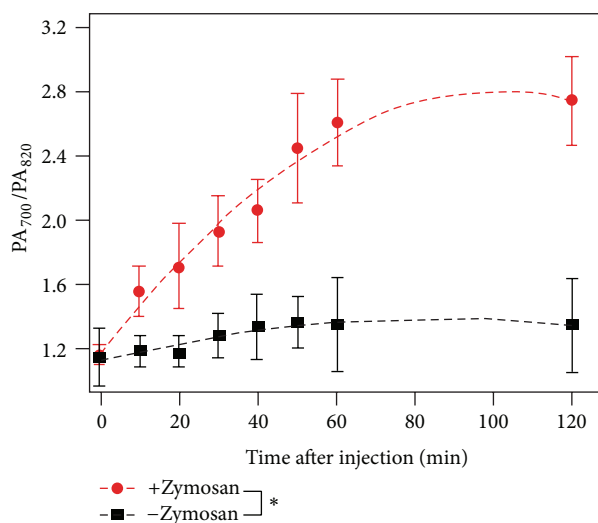
FIGURE 5: Differences on photoacoustic properties generated from conjugated polymer nanoparticles (SPN1), carbon nanotubes (SWCNTs), and gold nanorods (GNRs). (a) The photoacoustic intensity produced by different nanoparticles based on the same mass ($25 \mu\text{g mL}^{-1}$) (top) and molar (48 nM) (bottom) concentrations in an agar phantom. (b) The photoacoustic intensity regarding indicated nanoparticles in agar phantoms versus the number of laser pulses. (c) The photoacoustic intensity of the nanoparticle-matrigel targets (inclusions) ($30 \mu\text{L}$) in the subcutaneous dorsal space of living mice as a function of nanoparticle mass concentration. (d) The overlaid photoacoustic/ultrasound images of the nanoparticle-matrigel targets in mice at a concentration of $8 \mu\text{g mL}^{-1}$. Reproduced with permission from [24].

extinction coefficients and excellent photostability. These merits make SPNs superior PAT probes for generating strong and photostable photoacoustic signals in the near-infrared region when compared to SWCNT and GNR. At the same mass concentration, the intrinsic photoacoustic amplitude of the SPN at 700 nm can be over five times higher than that from SWCNT or GNR (Figure 5). Such high photoacoustic brightness in combination with its favorable size enables the efficient PAT of major lymph nodes in living mice with high sensitivity after a single intravenous administration of a small amount of SPNs. With the properties such as the narrow

photoacoustic spectral profile, good photostability, and reactive oxygen species (ROS) inert photoacoustic signals, they further developed SPN into an activated NIR ratiometric photoacoustic probe for in vivo imaging of reaction oxygen species (ROS) (Figure 6), a hallmark of many pathological processes such as cancer, cardiomyopathy, stroke, and bacterial infections. The SPN-based photoacoustic probes effectively detect ROS and exhibit great enhancements in ratiometric photoacoustic signals ($\text{PA}_{700}/\text{PA}_{820}$) of 25, 7.3, and 2.7 times in solution, in cells, and in living mice (Figure 6), respectively.



(a)



(b)

FIGURE 6: In vivo photoacoustic molecular tomography of reactive oxygen species (ROS) generation in a mouse model of acute oedema by using a ratiometric photoacoustic probe (RSPN). (a) The combined photoacoustic/ultrasound images in the thigh of living mice ($n = 3$) with respect to saline-treated (i) and zymosan-treated (ii) protocols. RSPN was injected into the thigh 20 min after zymosan treatment. (b) The ratio of photoacoustic signals generated between the wavelength of 700 and 820 nm (PA_{700}/PA_{820}) after RSPN injection. Reproduced with permission from [24].

4. Conclusions

In this review, recent advances of both inorganic and organic nanoparticle probes for structural and functional photoacoustic tomography have been highlighted. The use of multifarious nanoprobe for various in vitro, ex vivo, and in vivo tests represents a surging trend in nanobiotechnology and nanomedicine. However, inorganic nanoparticles have the characteristic of being nonbiodegradable, which could accumulate within the animal body for a relatively long time. Importantly, the issue on the long-term toxicity is yet not resolved for preclinical and clinical investigations. In terms of UCNPs, the efficiency of the UC process would be much lower due to the solvent relaxation problem in

aqueous conditions, which should significantly affect their potential applications for in vivo photoacoustic molecular tomography. Alternatively, organic nanoparticles including semiconducting polymers show good biocompatibility as demonstrated in different cellular assays [85–87]. In the coming years, we expect a more widespread study and application of these probes with potential clinical translations, in the areas such as deep-tissue imaging, molecular diagnosis of the disease, image-guided delivery, and targeted nanoparticle drug delivery, monitoring disease progression and outcome of therapy. For the further improvement of the performance of photoacoustic probes, we envision that the development of novel light-harvesting nanoparticle species that have well-controlled surface properties as well as targeting capability

and the usage of the probes for combined detection and treatment of diseases will be the most particular areas of interest in the near future.

Conflict of Interests

The authors declare that there is no conflict of interests regarding the publication of this paper.

Acknowledgments

Changfeng Wu acknowledges financial support from “Thousand Young Talents Program” and the National Science Foundation of China (Grants 61222508 and 61335001). The authors also acknowledge financial support from SRG2013-00035-FHS Grant, MYRG2014-00093-FHS and MYRG 2015-00036-FHS Grants from University of Macau in Macau, and FDCT Grant 026/2014/A1 from Macao Government.

References

- [1] Y. Wang, X. Xie, X. Wang et al., “Photoacoustic tomography of a nanoshell contrast agent in the in vivo rat brain,” *Nano Letters*, vol. 4, no. 9, pp. 1689–1692, 2004.
- [2] L. V. Wang and S. Hu, “Photoacoustic tomography: in vivo imaging from organelles to organs,” *Science*, vol. 335, no. 6075, pp. 1458–1462, 2012.
- [3] C. Kim, C. Favazza, and L. V. Wang, “In vivo photoacoustic tomography of chemicals: high-resolution functional and molecular optical imaging at new depths,” *Chemical Reviews*, vol. 110, no. 5, pp. 2756–2782, 2010.
- [4] X. Wang, Y. Pang, G. Ku, X. Xie, G. Stoica, and L. V. Wang, “Noninvasive laser-induced photoacoustic tomography for structural and functional in vivo imaging of the brain,” *Nature Biotechnology*, vol. 21, no. 7, pp. 803–806, 2003.
- [5] Z. Yuan, C. Wu, H. Zhao, and H. Jiang, “Imaging of small nanoparticle-containing objects by finite-element-based photoacoustic tomography,” *Optics Letters*, vol. 30, no. 22, pp. 3054–3056, 2005.
- [6] Z. Yuan, X. Q. Li, and L. Xi, “Listening to light scattering in turbid media: quantitative optical scattering imaging using photoacoustic measurements with one-wavelength illumination,” *Journal of Optics*, vol. 16, no. 6, Article ID 065301, 2014.
- [7] Z. Yuan, J. Zhang, X. D. Wang, and C. Q. Li, “A systematic investigation of reflectance diffuse optical tomography using nonlinear reconstruction methods and continuous wave measurements,” *Biomedical Optics Express*, vol. 5, no. 9, pp. 3011–3022, 2014.
- [8] Z. Yuan and H. Jiang, “Simultaneous recovery of tissue physiological and acoustic properties and the criteria for wavelength selection in multispectral photoacoustic tomography,” *Optics Letters*, vol. 34, no. 11, pp. 1714–1716, 2009.
- [9] Z. Yuan and H. B. Jiang, “Photoacoustic tomography for imaging nanoparticles,” in *Cancer Nanotechnology*, S. R. Grobmyer and B. Moudgil, Eds., vol. 624 of *Methods in Molecular Biology*, Humana Press, 2010.
- [10] L. Nie, S. Wang, X. Wang et al., “In vivo volumetric photoacoustic molecular angiography and therapeutic monitoring with targeted plasmonic nanostars,” *Small*, vol. 10, no. 8, pp. 1585–1593, 2014.
- [11] J. R. Cook, W. Frey, and S. Emelianov, “Quantitative photoacoustic imaging of nanoparticles in cells and tissues,” *ACS Nano*, vol. 7, no. 2, pp. 1272–1280, 2013.
- [12] X. Cai, W. Li, C.-H. Kim, Y. Yuan, L. V. Wang, and Y. Xia, “In vivo quantitative evaluation of the transport kinetics of gold nanocages in a lymphatic system by noninvasive photoacoustic tomography,” *ACS Nano*, vol. 5, no. 12, pp. 9658–9667, 2011.
- [13] Z. Chen, L. Ma, Y. Liu, and C. Chen, “Applications of functionalized fullerenes in tumor theranostics,” *Theranostics*, vol. 2, no. 3, pp. 238–250, 2012.
- [14] H. Xu, Q. Li, L. Wang et al., “Nanoscale optical probes for cellular imaging,” *Chemical Society Reviews*, vol. 43, no. 8, pp. 2650–2661, 2014.
- [15] Q. Zhang, N. Iwakuma, P. Sharma et al., “Gold nanoparticles as a contrast agent for in vivo tumor imaging with photoacoustic tomography,” *Nanotechnology*, vol. 20, no. 39, Article ID 395102, 2009.
- [16] K. A. Homan, M. Souza, R. Truby et al., “Silver nanoplate contrast agents for in vivo molecular photoacoustic imaging,” *ACS Nano*, vol. 6, no. 1, pp. 641–650, 2012.
- [17] A. de La Zerda, C. Zavaleta, S. Keren et al., “Carbon nanotubes as photoacoustic molecular imaging agents in living mice,” *Nature Nanotechnology*, vol. 3, no. 9, pp. 557–562, 2008.
- [18] L. Xi, S. R. Grobmyer, G. Zhou, W. Qian, L. Yang, and H. Jiang, “Molecular photoacoustic tomography of breast cancer using receptor targeted magnetic iron oxide nanoparticles as contrast agents,” *Journal of Biophotonics*, vol. 7, no. 6, pp. 401–409, 2014.
- [19] E. V. Shashkov, M. Everts, E. I. Galanzha, and V. P. Zharov, “Quantum dots as multimodal photoacoustic and photothermal contrast agents,” *Nano Letters*, vol. 8, no. 11, pp. 3953–3958, 2008.
- [20] S. K. Maji, S. Sreejith, J. Joseph et al., “Upconversion nanoparticles as a contrast agent for photoacoustic imaging in live mice,” *Advanced Materials*, vol. 26, no. 32, pp. 5633–5638, 2014.
- [21] A. D. L. Zerda, Z. Liu, S. Bodapati et al., “Ultrahigh sensitivity carbon nanotube agents for photoacoustic molecular imaging in living mice,” *Nano Letters*, vol. 10, no. 6, pp. 2168–2172, 2010.
- [22] G. Ku, M. Zhou, S. Song, Q. Huang, J. Hazle, and C. Li, “Copper sulfide nanoparticles as a new class of photoacoustic contrast agent for deep tissue imaging at 1064 nm,” *ACS Nano*, vol. 6, no. 8, pp. 7489–7496, 2012.
- [23] A. Hannah, G. Luke, K. Wilson, K. Homan, and S. Emelianov, “Indocyanine green-loaded photoacoustic nanodroplets: dual contrast nanoconstructs for enhanced photoacoustic and ultrasound imaging,” *ACS Nano*, vol. 8, no. 1, pp. 250–259, 2014.
- [24] K. Y. Pu, A. J. Shuhendler, J. V. Jokerst et al., “Semiconducting polymer nanoparticles as photoacoustic molecular imaging probes in living mice,” *Nature Nanotechnology*, vol. 9, no. 3, pp. 233–239, 2014.
- [25] C. Fan, S. Wang, J. W. Hong, G. C. Bazan, K. W. Plaxco, and A. J. Heeger, “Beyond superquenching: hyper-efficient energy transfer from conjugated polymers to gold nanoparticles,” *Proceedings of the National Academy of Sciences of the United States of America*, vol. 100, no. 11, pp. 6297–6301, 2003.
- [26] C. J. Murphy, A. M. Gole, J. W. Stone et al., “Gold nanoparticles in biology: beyond toxicity to cellular imaging,” *Accounts of Chemical Research*, vol. 41, no. 12, pp. 1721–1730, 2008.
- [27] J. Chen, F. Saeki, B. J. Wiley et al., “Gold nanocages: bioconjugation and their potential use as optical imaging contrast agents,” *Nano Letters*, vol. 5, no. 3, pp. 473–477, 2005.
- [28] W. Lu, Q. Huang, G. Ku et al., “Photoacoustic imaging of living mouse brain vasculature using hollow gold nanospheres,” *Biomaterials*, vol. 31, no. 9, pp. 2617–2626, 2010.

- [29] W. Lu, M. P. Melancon, C. Xiong et al., "Effects of photoacoustic imaging and photothermal ablation therapy mediated by targeted hollow gold nanospheres in an orthotopic mouse xenograft model of glioma," *Cancer Research*, vol. 71, no. 19, pp. 6116–6121, 2011.
- [30] J. V. Jokerst, M. Thangaraj, P. J. Kempen, R. Sinclair, and S. S. Gambhir, "Photoacoustic imaging of mesenchymal stem cells in living mice via silica-coated gold nanorods," *ACS Nano*, vol. 6, no. 7, pp. 5920–5930, 2012.
- [31] J. V. Jokerst, A. J. Cole, D. van de Sompel, and S. S. Gambhir, "Gold nanorods for ovarian cancer detection with photoacoustic imaging and resection guidance via Raman imaging in living mice," *ACS Nano*, vol. 6, no. 11, pp. 10366–10377, 2012.
- [32] E. C. Cho, C. Kim, F. Zhou et al., "Measuring the optical absorption cross sections of Au-Ag nanocages and Au nanorods by photoacoustic imaging," *The Journal of Physical Chemistry C*, vol. 113, no. 21, pp. 9023–9028, 2009.
- [33] H. J. Lee, Y. Liu, J. Zhao et al., "In vitro and in vivo mapping of drug release after laser ablation thermal therapy with doxorubicin-loaded hollow gold nanoshells using fluorescence and photoacoustic imaging," *Journal of Controlled Release*, vol. 172, no. 1, pp. 152–158, 2013.
- [34] D. Pan, M. Pramanik, A. Senpan et al., "Molecular photoacoustic imaging of angiogenesis with integrin-targeted gold nanobeacons," *The FASEB Journal*, vol. 25, no. 3, pp. 875–882, 2011.
- [35] G. P. Luke, A. Bashyam, K. A. Homan, S. Makhija, Y.-S. Chen, and S. Y. Emelianov, "Silica-coated gold nanoplates as stable photoacoustic contrast agents for sentinel lymph node imaging," *Nanotechnology*, vol. 24, no. 45, Article ID 455101, 2013.
- [36] M. K. Bucci, A. Maity, A. J. Janss et al., "Near complete surgical resection predicts a favorable outcome in pediatric patients with nonbrainstem, malignant gliomas: results from a single center in the magnetic resonance imaging era," *Cancer*, vol. 101, no. 4, pp. 817–824, 2004.
- [37] R. Stupp, M. E. Hegi, M. J. van den Bent et al., "Changing paradigms—an update on the multidisciplinary management of malignant glioma," *Oncologist*, vol. 11, no. 2, pp. 165–180, 2006.
- [38] M. F. Kircher, A. de La Zerda, J. V. Jokerst et al., "A brain tumor molecular imaging strategy using a new triple-modality MRI-photoacoustic-Raman nanoparticle," *Nature Medicine*, vol. 18, no. 5, pp. 829–834, 2012.
- [39] G. von Maltzahn, J.-H. Park, A. Agrawal et al., "Computationally guided photothermal tumor therapy using long-circulating gold nanorod antennas," *Cancer Research*, vol. 69, no. 9, pp. 3892–3900, 2009.
- [40] K. Kim, S.-W. Huang, S. Ashkenazi et al., "Photoacoustic imaging of early inflammatory response using gold nanorods," *Applied Physics Letters*, vol. 90, no. 22, Article ID 223901, 2007.
- [41] T. B. Huff, M. N. Hansen, Y. Zhao, J.-X. Cheng, and A. Wei, "Controlling the cellular uptake of gold nanorods," *Langmuir*, vol. 23, no. 4, pp. 1596–1599, 2007.
- [42] C. Loo, A. Lin, L. Hirsch et al., "Nanoshell-enabled photonics-based imaging and therapy of cancer," *Technology in Cancer Research & Treatment*, vol. 3, no. 1, pp. 33–40, 2004.
- [43] L. Xiang, Y. Yuan, D. Xing, Z. Ou, S. Yang, and F. Zhou, "Photoacoustic molecular imaging with antibody-functionalized single-walled carbon nanotubes for early diagnosis of tumor," *Journal of Biomedical Optics*, vol. 14, no. 2, Article ID 021008, 2009.
- [44] J.-W. Kim, E. I. Galanzha, E. V. Shashkov, H.-M. Moon, and V. P. Zharov, "Golden carbon nanotubes as multimodal photoacoustic and photothermal high-contrast molecular agents," *Nature Nanotechnology*, vol. 4, no. 10, pp. 688–694, 2009.
- [45] F. Zhou, S. Wu, Y. Yuan, W. R. Chen, and D. Xing, "Mitochondria-targeting photoacoustic therapy using single-walled carbon nanotubes," *Small*, vol. 8, no. 10, pp. 1543–1550, 2012.
- [46] R. Alwi, S. Telenkov, A. Mandelis et al., "Silica-coated superparamagnetic iron oxide nanoparticles (SPION) as biocompatible contrast agent in biomedical photoacoustics," *Biomedical Optics Express*, vol. 3, no. 10, pp. 2500–2509, 2012.
- [47] D. J. Grootendorst, J. Jose, R. M. Fratila et al., "Evaluation of superparamagnetic iron oxide nanoparticles (Endorem) as a photoacoustic contrast agent for intra-operative nodal staging," *Contrast Media and Molecular Imaging*, vol. 8, no. 1, pp. 83–91, 2013.
- [48] X. Feng, F. Gao, and Y. Zheng, "Thermally modulated photoacoustic imaging with super-paramagnetic iron oxide nanoparticles," *Optics Letters*, vol. 39, no. 12, pp. 3414–3417, 2014.
- [49] R. Qiao, C. Yang, and M. Gao, "Superparamagnetic iron oxide nanoparticles: from preparations to in vivo MRI applications," *Journal of Materials Chemistry*, vol. 19, no. 35, pp. 6274–6293, 2009.
- [50] A. P. Alivisatos, "Semiconductor clusters, nanocrystals, and quantum dots," *Science*, vol. 271, no. 5251, pp. 933–937, 1996.
- [51] W. C. W. Chan, D. J. Maxwell, X. Gao, R. E. Bailey, M. Han, and S. Nie, "Luminescent quantum dots for multiplexed biological detection and imaging," *Current Opinion in Biotechnology*, vol. 13, no. 1, pp. 40–46, 2002.
- [52] A. M. Smith and S. M. Nie, "Semiconductor nanocrystals: structure, properties, and band gap engineering," *Accounts of Chemical Research*, vol. 43, no. 2, pp. 190–200, 2010.
- [53] C. B. Murray, D. J. Norris, and M. G. Bawendi, "Synthesis and characterization of nearly monodisperse CdE (E = sulfur, selenium, tellurium) semiconductor nanocrystallites," *Journal of the American Chemical Society*, vol. 115, no. 19, pp. 8706–8715, 1993.
- [54] X. Gao, L. Yang, J. A. Petros, F. F. Marshall, J. W. Simons, and S. Nie, "In vivo molecular and cellular imaging with quantum dots," *Current Opinion in Biotechnology*, vol. 16, no. 1, pp. 63–72, 2005.
- [55] L. A. Bentolila, Y. Ebenstein, and S. Weiss, "Quantum dots for in vivo small-animal imaging," *The Journal of Nuclear Medicine*, vol. 50, no. 4, pp. 493–496, 2009.
- [56] T. Toyoda, K. Oshikane, D. Li, Y. Luo, Q. Meng, and Q. Shen, "Photoacoustic and photoelectrochemical current spectra of combined CdS/CdSe quantum dots adsorbed on nanostructured TiO₂ electrodes, together with photovoltaic characteristics," *Journal of Applied Physics*, vol. 108, no. 11, Article ID 114304, 2010.
- [57] S. Abdallah, N. Al-Hosiny, and A. Badawi, "Photoacoustic study of CdS QDs for application in quantum-dot-sensitized solar cells," *Journal of Nanomaterials*, vol. 2012, Article ID 498286, 6 pages, 2012.
- [58] P. Huang, J. Lin, W. Li et al., "Biodegradable gold nanovesicles with an ultrastrong plasmonic coupling effect for photoacoustic imaging and photothermal therapy," *Angewandte Chemie—International Edition*, vol. 52, no. 52, pp. 13958–13964, 2013.

- [59] H.-W. Yang, H.-L. Liu, M.-L. Li et al., "Magnetic gold-nanorod/PNIPAAmMA nanoparticles for dual magnetic resonance and photoacoustic imaging and targeted photothermal therapy," *Biomaterials*, vol. 34, no. 22, pp. 5651–5660, 2013.
- [60] K. Yang, H. Xu, L. Cheng, C. Sun, J. Wang, and Z. Liu, "In vitro and in vivo near-infrared photothermal therapy of cancer using polypyrrole organic nanoparticles," *Advanced Materials*, vol. 24, no. 41, pp. 5586–5592, 2012.
- [61] Y. Li, W. Lu, Q. Huang, C. Li, and W. Chen, "Copper sulfide nanoparticles for photothermal ablation of tumor cells," *Nanomedicine*, vol. 5, no. 8, pp. 1161–1171, 2010.
- [62] L. Xu, X. Chen, L. Ma, and F. Gao, "Facile preparation of copper sulfide nanoparticles from perovskite templates containing bromide anions," *Colloids and Surfaces A: Physicochemical and Engineering Aspects*, vol. 349, no. 1–3, pp. 69–73, 2009.
- [63] P. Huang, Z. Li, H. Hu, and D. Cui, "Synthesis and characterization of bovine serum albumin-conjugated copper sulfide nanocomposites," *Journal of Nanomaterials*, vol. 2010, Article ID 641545, 6 pages, 2010.
- [64] M. Zhou, R. Zhang, M. Huang et al., "A chelator-free multifunctional [^{64}Cu]CuS nanoparticle platform for simultaneous micro-PET/CT imaging and photothermal ablation therapy," *Journal of the American Chemical Society*, vol. 132, no. 43, pp. 15351–15358, 2010.
- [65] Z. Li, Y. Zhang, and S. Jiang, "Multicolor core/shell-structured upconversion fluorescent nanoparticles," *Advanced Materials*, vol. 20, no. 24, pp. 4765–4769, 2008.
- [66] F. Vetrone, R. Naccache, A. J. de La Fuente et al., "Intracellular imaging of HeLa cells by non-functionalized $\text{NaYF}_4:\text{Er}^{3+}, \text{Yb}^{3+}$ upconverting nanoparticles," *Nanoscale*, vol. 2, no. 4, pp. 495–498, 2010.
- [67] N.-N. Dong, M. Pedroni, F. Piccinelli et al., "NIR-to-NIR two-photon excited $\text{CaF}_2:\text{Tm}^{3+}, \text{Yb}^{3+}$ nanoparticles: multifunctional nanoprobe for highly penetrating fluorescence bio-imaging," *ACS Nano*, vol. 5, no. 11, pp. 8665–8671, 2011.
- [68] Q. Liu, T. Yang, W. Feng, and F. Li, "Blue-emissive upconversion nanoparticles for low-power-excited bioimaging in vivo," *Journal of the American Chemical Society*, vol. 134, no. 11, pp. 5390–5397, 2012.
- [69] Y. Yang, Q. Shao, R. Deng et al., "In vitro and in vivo uncaging and bioluminescence imaging by using photocaged upconversion nanoparticles," *Angewandte Chemie*, vol. 51, no. 13, pp. 3125–3129, 2012.
- [70] G. Y. Chen, T. Y. Ohulchanskyy, S. Liu et al., "Core/shell $\text{NaGdF}_4:\text{Nd}^{3+}/\text{NaGdF}_4$ nanocrystals with efficient near-infrared to near-infrared downconversion photoluminescence for bioimaging applications," *ACS Nano*, vol. 6, no. 4, pp. 2969–2977, 2012.
- [71] J. R. Lindner, "Microbubbles in medical imaging: current applications and future directions," *Nature Reviews Drug Discovery*, vol. 3, no. 6, pp. 527–532, 2004.
- [72] J. Zhong, S. Yang, X. Zheng, T. Zhou, and D. Xing, "In vivo photoacoustic therapy with cancer-targeted indocyanine green-containing nanoparticles," *Nanomedicine*, vol. 8, no. 6, pp. 903–919, 2013.
- [73] K. Wilson, K. Homan, and S. Emelianov, "Biomedical photoacoustics beyond thermal expansion using triggered nanodroplet vaporization for contrast-enhanced imaging," *Nature Communications*, vol. 3, article 618, 2012.
- [74] C. Wu and D. T. Chiu, "Highly fluorescent semiconducting polymer dots for biology and medicine," *Angewandte Chemie—International Edition*, vol. 52, no. 11, pp. 3086–3109, 2013.
- [75] C. Wu, C. Szymanski, and J. McNeill, "Preparation and encapsulation of highly fluorescent conjugated polymer nanoparticles," *Langmuir*, vol. 22, no. 7, pp. 2956–2960, 2006.
- [76] S. Kim, C. K. Lim, J. Na et al., "Conjugated polymer nanoparticles for biomedical in vivo imaging," *Chemical Communications*, vol. 46, no. 10, pp. 1617–1619, 2010.
- [77] L. Feng, C. Zhu, H. Yuan, L. Liu, F. Lv, and S. Wang, "Conjugated polymer nanoparticles: preparation, properties, functionalization and biological applications," *Chemical Society Reviews*, vol. 42, no. 16, pp. 6620–6633, 2013.
- [78] D. Ding, J. Liu, G. Feng, K. Li, Y. Hu, and B. Liu, "Bright far-red/near-infrared conjugated polymer nanoparticles for in vivo bioimaging," *Small*, vol. 9, no. 18, pp. 3093–3102, 2013.
- [79] E. Ahmed, S. W. Morton, P. T. Hammond, and T. M. Swager, "Fluorescent multiblock π -conjugated polymer nanoparticles for in vivo tumor targeting," *Advanced Materials*, vol. 25, no. 32, pp. 4504–4510, 2013.
- [80] P. Howes, M. Green, A. Bowers et al., "Magnetic conjugated polymer nanoparticles as bimodal imaging agents," *Journal of the American Chemical Society*, vol. 132, no. 28, pp. 9833–9842, 2010.
- [81] Y.-H. Chan, C. Wu, F. Ye, Y. Jin, P. B. Smith, and D. T. Chiu, "Development of ultrabright semiconducting polymer dots for ratiometric pH sensing," *Analytical Chemistry*, vol. 83, no. 4, pp. 1448–1455, 2011.
- [82] C. Wu, T. Schneider, M. Zeigler et al., "Bioconjugation of ultrabright semiconducting polymer dots for specific cellular targeting," *Journal of the American Chemical Society*, vol. 132, no. 43, pp. 15410–15417, 2010.
- [83] J. Yu, C. Wu, X. Zhang et al., "Stable functionalization of small semiconducting polymer dots via covalent cross-linking and their application for specific cellular imaging," *Advanced Materials*, vol. 24, no. 26, pp. 3498–3504, 2012.
- [84] Y. Rong, C. Wu, J. Yu et al., "Multicolor fluorescent semiconducting polymer dots with narrow emissions and high brightness," *ACS Nano*, vol. 7, no. 1, pp. 376–384, 2013.
- [85] N. A. A. Rahim, W. McDaniel, K. Bardion et al., "Conjugated polymer nanoparticles for two-photon imaging of endothelial cells in a tissue model," *Advanced Materials*, vol. 21, no. 34, pp. 3492–3496, 2009.
- [86] X. Feng, F. Lv, L. Liu et al., "Conjugated polymer nanoparticles for drug delivery and imaging," *ACS Applied Materials and Interfaces*, vol. 2, no. 8, pp. 2429–2435, 2010.
- [87] B. Sun, M.-J. Sun, Z. Gu et al., "Conjugated polymer fluorescence probe for intracellular imaging of magnetic nanoparticles," *Macromolecules*, vol. 43, no. 24, pp. 10348–10354, 2010.

Research Article

A Series of Imidazole Derivatives: Synthesis, Two-Photon Absorption, and Application for Bioimaging

Yingzhong Zhu,¹ Lufei Xiao,^{1,2} Meng Zhao,¹ Jiazheng Zhou,¹ Qiong Zhang,¹
Hui Wang,¹ Shengli Li,¹ Hongping Zhou,¹ Jieying Wu,¹ and Yupeng Tian^{1,3}

¹Department of Chemistry, Key Laboratory of Functional Inorganic Material Chemistry of Anhui Province, Anhui University, Hefei 230601, China

²Department of Food and Environmental Engineering, Chuzhou Vocational and Technical College, Chuzhou 239000, China

³State Key Laboratory of Coordination Chemistry, Nanjing University, Nanjing 210093, China

Correspondence should be addressed to Jieying Wu; jywu1957@163.com and Yupeng Tian; yptian@ahu.edu.cn

Received 18 October 2014; Accepted 30 December 2014

Academic Editor: Yu-Chang Tyan

Copyright © 2015 Yingzhong Zhu et al. This is an open access article distributed under the Creative Commons Attribution License, which permits unrestricted use, distribution, and reproduction in any medium, provided the original work is properly cited.

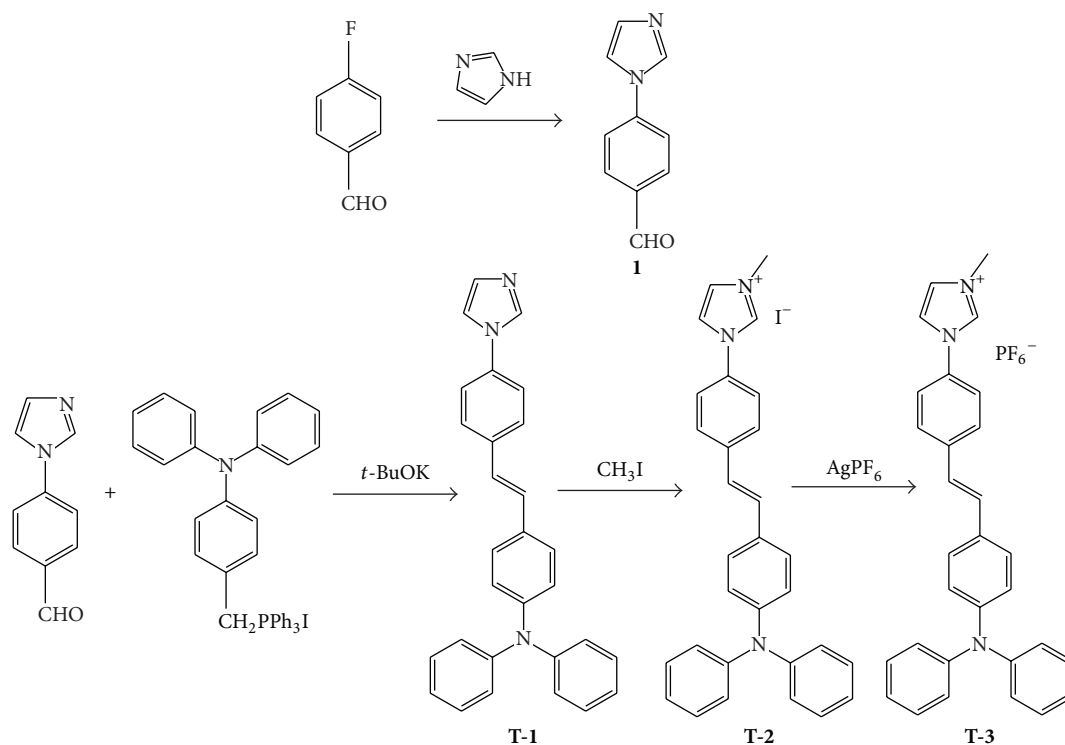
A new series of D- π -A type imidazole derivatives have been synthesized and characterized. Two corresponding imidazolium salts (iodine and hexafluorophosphate) were prepared from the imidazole compound. Their electron-withdrawing ability can be largely tunable by salt formation reaction or ion exchange. UV-vis absorption and single-photon fluorescence spectra have been systematically investigated in different solvents. The two-photon cross sections (δ_{2PA}) of the imidazole derivatives are measured by two-photon excited fluorescence (2PEF) method. Compared with those of T-1 (107 GM) and T-3 (96 GM), T-2 (imidazolium iodine salt) has a large two-photon absorption (2PA) cross section value of 276 GM. Furthermore, the cytotoxicity and applications in bioimaging for the imidazole derivatives were carried out. The results showed that T-1 can be used as a lysosomal tracker with high stability and water solubility within pHs of 4–6, while T-2 and T-3 can be used as probes for cell cytoplasm.

1. Introduction

Fluorescence biomarker has become a powerful tool for the monitoring and investigating of cellular processes in live tissues, as well as *in vivo* clinical related researches. Ideal fluorescence probes offered a unique approach for visualizing morphological details of tissue under subcellular resolution [1], without altering the biological activity of live cells/tissues in long-term range. For more specific cell biological research purpose, probes can be designed to bond with specific organelle of interest and provide guaranteed fluorescence signals. Until now, a variety of new fluorescence probes, such as organic dyes [2, 3], metal complexes [4, 5], and quantum dots [2, 3, 6, 7], have been synthesized for such purpose.

Compared to single-photon imaging, two-photon imaging shows significant benefits, such as deep tissue penetration and less photobleaching [8–11]. These superiorities encouraged researchers to make great efforts to obtain the materials with excellent two-photon absorption (2PA) properties in last

decades. Generally, a large 2PA cross section is prerequisite, which is influenced by electron-donor and withdrawing abilities, conjugation length, and planarity of the π center [12–14]. Imidazole, as an N-heterocycle molecule, has been widely used in many biological processes [15–18]. It has high electron-withdrawing ability and good coplanarity, rendering it to be an ideal building block for nonlinear optical materials [19, 20]. In addition, triphenylamine group was utilized in optical material [21–23] due to a strong electron donor and effective conjugation length. Stryryl groups with excellent coplanarity are beneficial to increase effective conjugation length [24, 25]. Based on the above considerations, at present work, in order to obtain the material with large 2PA cross section, imidazole, triphenylamine, and styryl group were used as link to construct the three D- π -A chromophores. The photophysical properties and the connections between structure and properties of the three chromophores were investigated. Furthermore, potential biological applications of them were carried out.



SCHEME 1: Synthesis routes for compounds T-1, T-2, and T-3.

2. Experiment

See Scheme 1.

2.1. General. All chemicals were commercially available and used without further purification. The solvents were purified by conventional methods before being used. 4-(1H-Imidazol-1-yl)benzaldehyde was synthesized according to the methods reported. The $^1\text{H-NMR}$ and $^{13}\text{C-NMR}$ spectra recorded at 25°C using Bruker Avance 400 spectrometer were reported as parts per million (ppm) from TMS. Mass spectra were determined with a Micromass GCT-MS (EI source).

X-ray diffraction data of single crystals were collected on CCD diffractometer. The determination of unit cell parameters and data collections were performed with $\text{Mo-K}\alpha$ radiation ($\lambda = 0.71073 \text{ \AA}$). Unit cell dimensions were obtained with least-squares refinements, and all structures were solved by direct methods using SHELXS-97. The other nonhydrogen atoms were located in successive difference Fourier syntheses. The final refinement was performed by full-matrix least-squares methods with anisotropic thermal parameters for nonhydrogen atoms on F^2 . The hydrogen atoms were added theoretically and bonded with the concerned atoms.

Electronic absorption spectra were obtained on a UV-265 spectrophotometer. Fluorescence measurements were performed using a Hitachi F-7000 fluorescence spectrophotometer. For time-resolved fluorescence measurements, the fluorescence signals were collimated and focused onto the entrance slit of a monochromator with the output plane equipped with a photomultiplier tube (HORIBA HuoroMax-4P). The decays were analyzed by "least-squares." The quality

of the exponential fits was evaluated by the goodness of fit (χ^2). TPEF spectra were measured using femtosecond laser pulse and Ti: sapphire system (680–1080 nm, 80 MHz, 140 fs, Chameleon II) as the light source.

2.2. Synthesis

2.2.1. 4-(1H-Imidazol-1-yl)benzaldehyde (1). 4-(1H-Imidazol-1-yl)benzaldehyde was prepared according to the literature method [26].

2.2.2. Synthesis of (E)-4-(4-(1H-Imidazol-1-yl)styryl)-N,N-diphenylaniline. *t*-BuOK (2.32 g, 20 mmol), 4-(1H-imidazole-1-yl)benzaldehyde (**1**) (1.72 g, 10 mmol), and 4-((iodotriphenyl phosphoranyl)methyl)-N,N-diphenylaniline (6.47 g, 10 mmol) 150 mL dry THF were added and mixed equally. The mixture was stirred for 10 min and then heated to 65°C for 24 h. The reaction was monitored by TLC. 250 mL CH_2Cl_2 was added after the solvent was removed. The organic layer was washed with water several times and dried over anhydrous MgSO_4 . The residue was purified by flash chromatography on silica gel using petroleum/ethyl acetate (5:1) as eluent and gave green solid T-1 (1.7 g, yield: 47.2%). $^1\text{H-NMR}$: (DMSO, 400 MHz) δ (ppm) 8.30 (s, 1H), 7.78 (s, 1H), 7.70–7.72 (d, 2H, $J = 8.4$), 7.66–7.68 (d, 2H, $J = 8.4$), 7.52–7.54 (d, 2H, $J = 8.4$), 7.31–7.35 (t, 3H, $J = 7.6$), 7.25–7.31 (d, 1H, $J = 16.4$), 7.14–7.18 (d, 1H, $J = 16.4$), 7.19–7.21 (d, 2H, $J = 9.6$), 7.04–7.07 (t, 6H, $J = 7.8$), 6.96–6.98 (d, 2H, $J = 8.4$). $^{13}\text{C-NMR}$ (DMSO, 400 MHz) δ (ppm): 146.90 (CH), 135.91 (CH), 135.37 (CH), 129.58 (CH), 127.65 (CH), 127.47 (CH),

TABLE 1: Photophysical properties of T-1, T-2, and T-3 in several of different polar solvents.

Compound	Solvent	λ_{ab} (nm) ^[a]	log ϵ	λ_{em} (nm) ^[b]	Φ ^[c]	τ (ns) ^[d]	Stokes' shift (cm ⁻¹) ^[e]
T-1	Benzene	299, 377	4.39, 4.55	428	0.61	1.71	10080, 3160
	DCM	296, 375	4.37, 4.52	458	0.67	2.28	11949, 4832
	Ethanol	294, 371	4.42, 4.56	454	0.59	2.33	11987, 4927
	Ethyl acetate	296, 371	4.43, 4.54	444	0.37	1.97	11261, 4431
	DMF	297, 374	4.37, 4.53	466	0.59	2.54	12210, 5278
T-2	Benzene	297, 383	4.46, 4.46	448	0.37	1.66	11348, 3788
	DCM	296, 389	4.47, 4.55	499	0.28	1.86	13743, 5666
	Ethanol	294, 381	4.50, 4.64	494	0.18	1.37	13770, 6003
	Ethyl acetate	294, 375	4.50, 4.56	455	0.35	1.84	12035, 4688
	DMF	296, 380	4.51, 4.65	505	0.23	2.14	13981, 6513
T-3	Benzene	298, 389	4.15, 4.19	460	0.69	1.53	11817, 3967
	DCM	295, 393	4.18, 4.27	509	0.42	1.97	14251, 5798
	Ethanol	294, 381	4.27, 4.40	494	0.33	1.37	13770, 6003
	Ethyl acetate	294, 377	4.36, 4.45	469	0.47	1.92	12691, 5203
	DMF	296, 381	4.16, 4.30	505	0.45	2.21	13981, 6444

^[a]Peak position of the longest absorption band. ^[b]Peak position of SPEF, excited at the absorption maximum. ^[c]Quantum yields determined by using quinine sulfate as standard. ^[d]Fluorescent lifetime in different solutions. ^[e]Stokes' shift in cm⁻¹.

125.63 (CH), 124.15 (CH), 123.29 (CH), 122.88 (CH), 120.36 (CH), 117.79 (CH). MS, m/z : 414.

2.2.3. *Synthesis of (E)-1-(4-(4-(Diphenylamino)styryl)phenyl)-3-methyl-1H-imidazol-3-ium Iodide (T-2)*. T-1 (0.413 g, 1 mmol) and 5 mL CH₃I were mixed together in 50 mL flask. The mixture was stirred overnight and filtered and it gave green solid (T-2) (0.48 g, yield: 85.6). ¹H-NMR: (DMSO, 400 MHz) δ (ppm) 9.77 (s, 1H), 8.31 (s, 1H), 7.96 (s, 1H), 7.83–7.85 (d, 2H, $J = 8$), 7.75–7.77 (d, 2H, $J = 8$), 7.53–7.55 (d, 2H, $J = 8$), 7.32–7.36 (t, 5H, $J = 7.6$), 7.18–7.22 (d, 1H, $J = 16$), 7.05–7.11 (dd, 6H, $J = 9.2, 8$), 6.97–6.99 (d, 2H, $J = 8$), 3.95 (s, 3H). ¹³C-NMR (DMSO, 400 MHz) δ (ppm): 147.18 (CH), 146.81 (CH), 138.81 (CH), 135.71 (CH), 133.18 (CH), 130.62 (CH), 130.03 (CH), 129.61 (CH), 128.29 (CH), 127.88 (CH), 127.56 (CH), 124.90 (CH), 124.31 (CH), 123.45 (CH), 122.61 (CH), 121.88 (CH), 120.75 (CH), 36.14 (CH₃). MS, m/z : 429.

2.2.4. *Synthesis of (E)-1-(4-(4-(Diphenylamino)styryl)phenyl)-3-methyl-1H-imidazol-3-ium Hexafluorophosphate (V) (T-3)*. T-2 (0.561 g, 1 mmol) and 100 mL CH₃CN were added to flask with stirring for 10 min, followed by dropping AgPF₆ (0.253, 1 mmol) which was dissolved in 30 mL CH₃CN. The resulting suspension was further stirred for 2 hours before being filtrated. After removal of the solvent, the yellow-green solid was obtained (0.55 g, 96.0%). ¹H-NMR: (DMSO, 400 MHz) δ (ppm) 9.77 (s, 1H), 8.31 (s, 1H), 7.96 (s, 1H), 7.83–7.85 (d, 2H, $J = 8$), 7.75–7.77 (d, 2H, $J = 8$), 7.53–7.55 (d, 2H, $J = 8$), 7.32–7.35 (t, 5H, $J = 7.6$), 7.18–7.22 (d, 1H, $J = 16$), 7.05–7.11 (dd, 6H, $J = 9.2, 8$), 6.97–6.99 (d, 2H, $J = 8$), 3.95 (s, 3H). ¹³C-NMR (DMSO, 400 MHz) δ (ppm): 147.18 (CH), 146.81 (CH), 138.81 (CH), 135.70 (CH), 133.18 (CH), 130.61 (CH), 130.03 (CH), 129.61 (CH), 128.29 (CH), 127.87 (CH), 127.55 (CH), 124.88 (CH), 124.32 (CH), 123.45 (CH), 122.60 (CH), 121.88 (CH), 120.75 (CH), 36.11 (CH₃). MS, m/z : 429.

3. Results and Discussion

3.1. *Crystal Structures of T-1 and T-3*. The single crystals of T-1 and T-2, suitable for the X-ray analysis, were obtained from slow evaporation of methanol/benzene at room temperature several days later. Crystal data collection and refinement parameters are listed in Table S1 in Supplementary Material available online at <http://dx.doi.org/10.1155/2015/965386>. The crystal structures of T-1 and T-3 are shown in Figure S1.

T-1 crystallizes with two independent molecules in asymmetric unit, and the crystal of T-1 belongs to monoclinic system with $P2_1/n$ space group. The benzene rings of the triarylamine constitute a structure like propeller, with dihedral between two benzene rings 74.84°. The dihedral angle between styryl and benzene ring of triarylamine is 7.97°, while the dihedral angle between imidazole ring and styryl is 9.27°. What is more, all the bond lengths of C-C are located between the normal C=C double bond (1.32 Å) and C-C single bond (1.53 Å), which show a highly π -electron delocalized system in the molecule. With regard to T-2, it crystallizes in triclinic system with $P\bar{1}$ space group and two independent molecules in asymmetric unit. Compared with T-1, the introduction of methyl leads to a larger dihedral angle; the dihedral angle between styryl and benzene ring of triarylamine is 18.80°, while between imidazole ring and styryl it is 22.79°. This means T-1 has a better planarity of π center. The structural features indicate that the coplanarity of the two compounds is appropriate, which is a necessary condition for preferable nonlinear optical properties [27].

3.2. *Linear Absorption and Single-Photon Excited Fluorescence*. The UV-vis absorption spectra of the three chromophores T-1, T-2, and T-3 in different solvents are shown in Figure S2. And the corresponding absorptive data are listed in Table 1. Their absorption spectra show peak maxima at ~295 and ~380 nm, with $\epsilon > 10^4$ dm³ mol⁻¹ cm⁻¹. There is only

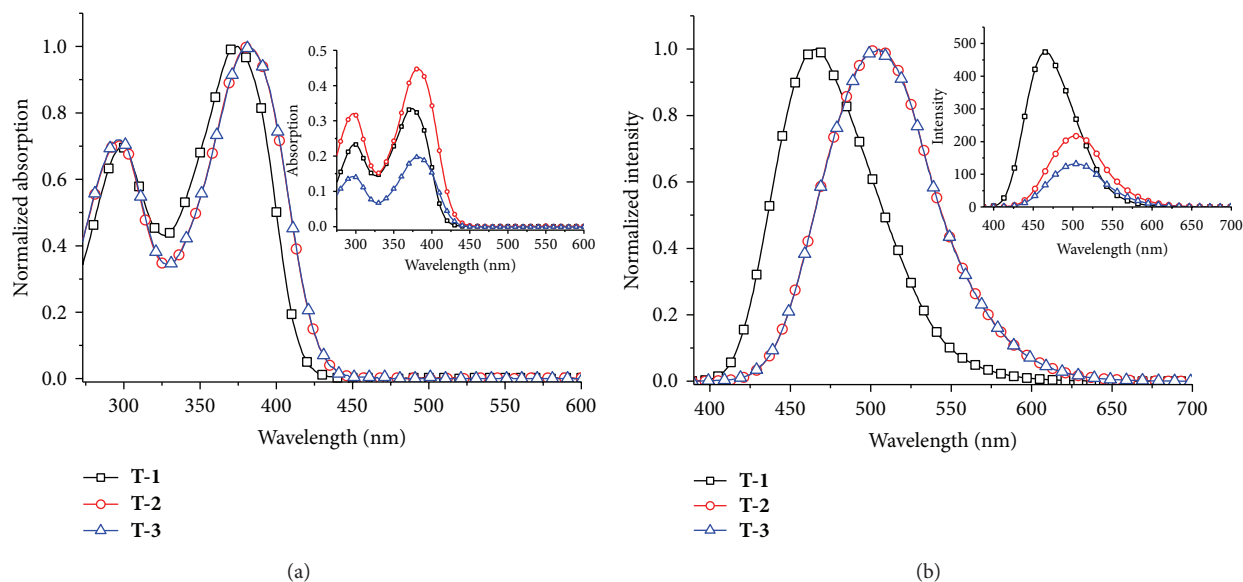


FIGURE 1: The normalized UV-vis spectra (a) and single-photon fluorescence spectra (b) of **T-1**, **T-2**, and **T-3** (1.0×10^{-5} M) in DMF solution; the insert shows the original data of their UV-vis spectra and single-photon fluorescence spectra.

slight solvatochromic shift (± 5 nm) for the absorption spectra of the three chromophores upon changing the solvents from benzene to DMF, indicating that the polarity of solvents has little effect on the ground state and the excited state [28]. Figure 1(a) depicts their UV-vis spectra in DMF. The high energy bands of all the chromophores occur at about 290 nm with little red-shift. The low energy bands appear around 380 nm. The normalized line of **T-2** coincides with that of **T-3**. This means the exchanging anion has no influence on the UV-vis absorption. Nevertheless, compared with **T-1**, imidazolium salts show small red-shift (10 nm) which may be caused by the formation of imidazolium cation as a stronger acceptor. Through calculation of molar absorption coefficient ($\log \epsilon$) the band at about 295 nm can be attributed to the $\pi \rightarrow \pi^*$ transition from triphenylamine moiety, while the band around 480 nm is ascribed to $\pi \rightarrow \pi^*$ transition within the entire molecule.

The single-photon fluorescence spectra of **T-1**, **T-2**, and **T-3** in different solvents are shown in Figure S3. The corresponding emission spectral data are listed in Table 1. It can be seen from Figure S3 that a remarkable bathochromic shift takes place for all the chromophores upon changing the solvent from benzene to DMF, which can be explained that the degree of charge separation in the excited state increase resulting in a larger dipole moment than that in ground state; therefore, the emission spectra of these dipolar chromophores exhibit sensitivity to solvent polarity [29, 30]. Accordingly, the Stokes shifts significantly increase with increasing solvent polarity, ranging from 3196 cm^{-1} in benzene to 5278 cm^{-1} in DMF (**T-1**), 3788 cm^{-1} in benzene to 6444 cm^{-1} in DMF (**T-2**), and 3967 cm^{-1} in benzene to 6444 cm^{-1} in DMF (**T-3**). The emission spectra of **T-1**, **T-2**, and **T-3** in benzene show a well resolved vibrational structure. When increasing solubility and solvent polarity, a loss of

the vibronic structure is observed; a progressive red-shift of the emission wavelength occurs [27]. Compared to **T-1**, both imidazolium salts have an obvious red-shift over 20 nm in nonpolar solvent and 40 nm in polar solvent. This phenomenon was caused by the salt formation to enhance the electron accepted ability of the imidazole group.

The chromophores exhibit high quantum yield (>0.1) in various solvents. Importantly, the quantum yields (Φ) in high polar solvent DMF are 0.59 (**T1**), 0.23 (**T2**), and 0.45 (**T3**), respectively. **T1** with a weaker electron acceptor, imidazole ring, could cause the extra charge-separated in excited state [31], so **T-1** possesses the highest fluorescence quantum yield. The data of fluorescence lifetimes are listed in Table 1; it shows that the chromophores have similar lifetime in the same solvent. This can be attributed to nearly molecular stabilization effect on the excited state in the extended delocalization system of the molecules. With the increasing polarity of the solvents the lifetime prolongs from 1.7 to 2.54 ns for **T-1**, 1.66 to 2.14 ns for **T-2**, and 1.53 to 2.21 ns for **T-3**. That is to say, the conformational stability of the excited molecule is influenced by the polarity of the solvents [32].

The Lippert-Mataga equation (shown in Supplementary Material) is widely used to evaluate the dipole moment changes of the dyes with photoexcitation [33, 34]; the emission of the chromophores, especially, is strongly dependent on solvent polarity. As shown in Figure 2, the Lippert-Mataga plots exhibit a linear behavior; this means no specific interaction exists between the solvent and the chromophores, except for the polarizability as modeled [35, 36]. The slope of the fitting line is related to the dipole moment change between the ground and excited states ($\mu_e - \mu_g$). Larger slope in the Lippert-Mataga plot infers larger dipole moment changes with photoexcitation. The dipole moment changes of the chromophores **T-1**, **T-2**, and **T-3** ($\mu_e - \mu_g$) are calculated

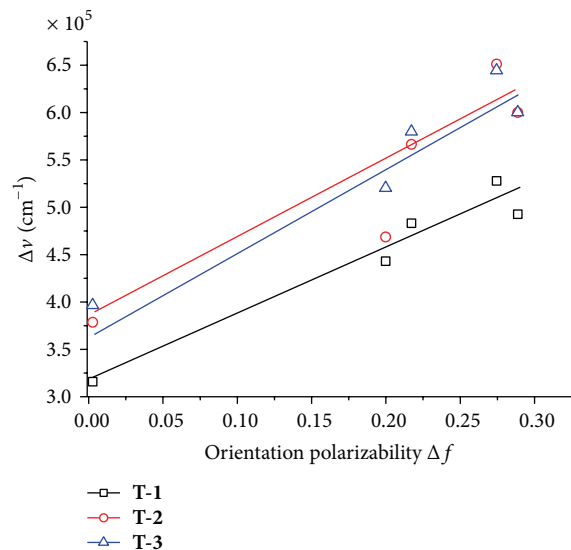


FIGURE 2: Lippert-Mataga plots for T-1, T-2, and T-3.

as 13.07 D, 13.70 D, and 14.47 D, respectively [37]. This means the chromophores in the excited state have large polar structures which provide promising linear and nonlinear optical properties [38].

3.3. Two-Photon Excited Fluorescence (2PEF). 2PA cross sections of the compounds were determined by two-photon excited fluorescence (2PEF) method in near-IR (NIR) range from 700 to 1000 nm. Experiments revealed that linear absorption did not exist from 500 nm to 900 nm for all the chromophores, indicating that there were no molecular energy levels corresponding to an electron transition in this spectral range. Hence, upon excitation from 700 nm to 1000 nm at intervals of 10 nm (similarly hereinafter), it was impossible to produce single-photon excited upconverted fluorescence. If frequency upconverted fluorescence appeared upon excitation with a tunable laser in this range, it should be safely attributed to multiphoton excited fluorescence.

By tuning the pump wavelengths incrementally from 700 to 880 nm, keeping the input power fixed, the 2PEF intensities were recorded. As shown in Figure S5 all of the chromophores exhibit fluorescence in the wavelength range of 720–880 nm. Figure S4 shows the linear dependence on the square of input laser power which suggests a two-photon excitation mechanism at 760 nm for the chromophores. The normalized 2PEF peak positions of 3P-2 and 3P-3 shown in Figure 3 show no difference, which means anions have little influence on the position. But anions can influence their intensity of 2PEF which shown in Figure S6. Nevertheless compared with T-1, imidazolium salts show a clear red-shift for near 30 nm.

The two-photon absorption (2PA) cross section (σ) of the chromophores T-1, T-2, and T-3 in DMF using two-photon-induced fluorescence method with fluorescein as the standard is shown in Figure 4 [39, 40]. The 2PA cross section equation is shown in Supplementary Material. The largest 2PA cross

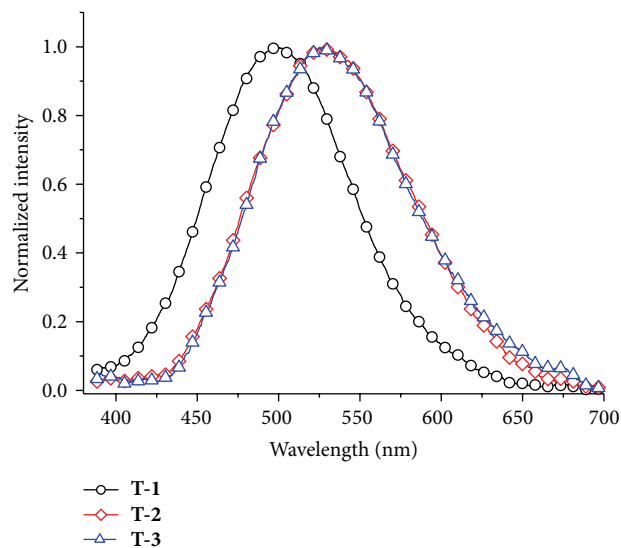


FIGURE 3: The normalized two-photon excited fluorescence spectra of T-1, T-2, and T-3 (excitation wavelength at 760 nm, energy of 500 mW, $c = 1.0 \times 10^{-3} \text{ mol}\cdot\text{L}^{-1}$) in DMF.

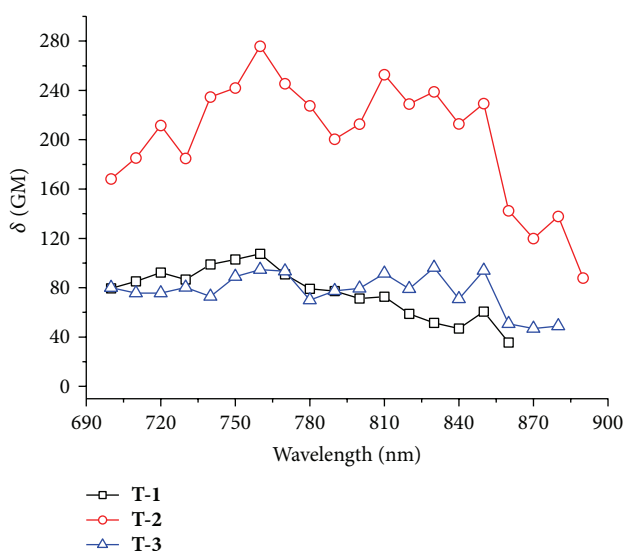


FIGURE 4: Two-photon absorption cross sections of T-1, T-2, and T-3 (excitation wavelength from 700 nm to 890 nm, power of 500 mW, $c = 1.0 \times 10^{-3} \text{ mol}\cdot\text{L}^{-1}$) in DMF.

sections of all the chromophores located at 760 nm with the highest values 107 GM, 276 GM, and 96 GM, respectively, are depicted in Figure 4. T-2 owns the largest 2PA cross section in this spectral range, though T-1 has the largest two-photon fluorescence intensity in Figure 3. The reason is that maybe T-2 has the smallest fluorescence quantum yield.

3.4. Cell Image and Cytotoxicity Assay. Due to their high quantum yield, long fluorescence lifetime, and large 2PA cross section, these three chromophores potentially can be utilized in bioimaging.

Before exploring their biological applications, cytotoxicities of the chromophores were firstly measured toward

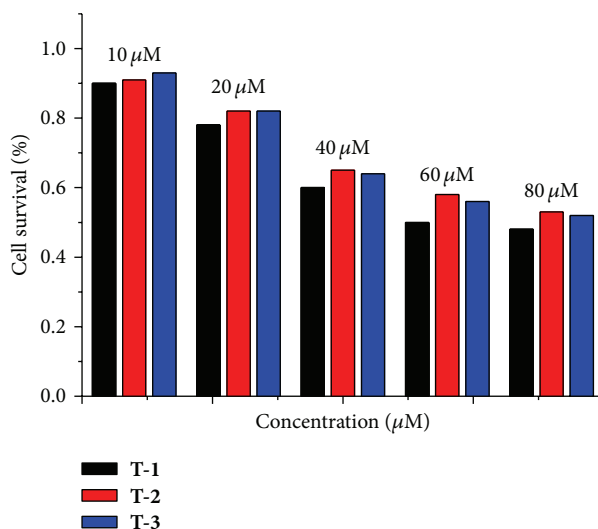


FIGURE 5: Cytotoxicity data results of T-1, T-2, and T-3 obtained from the MTT assay.

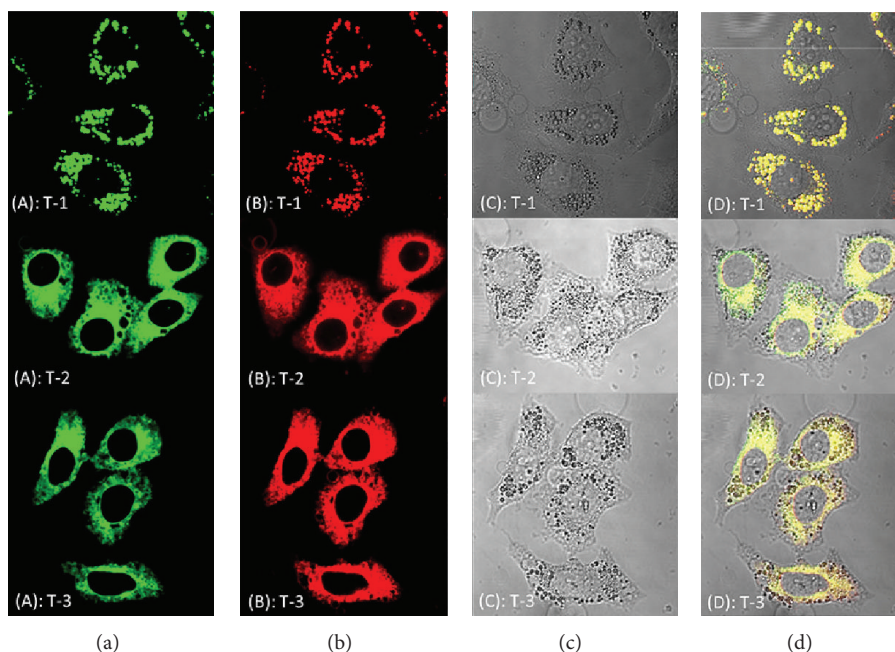


FIGURE 6: (a) One-photon image of HepG2 cells incubated with $20 \mu\text{M}$ after 20 min of incubation, washed by PBS buffer. (b) Two-photon image of HePG2 cells incubated with $20 \mu\text{M}$ after 30 min of incubation, washed by PBS buffer. (c) Bright field image of HePG2 cells. (d) The overlay of (a) to (c). Scale bars represent $10 \mu\text{M}$.

the human cervical carcinoma cells (HepG2) by MTT assay, a standard method to probe cell survival fraction. Figure 5 shows that, in the presence of the probes with the concentration from 10 to $20 \mu\text{M}$, the cellular viabilities of HepG2 cells are greater than 85% after incubation for 24 h. All of the data indicate that low-micromolar concentrations of three probes are essentially low-nontoxic within 24 h. As a result, all the chromophores can safely be used for further bioimaging.

Afterwards, fluorescent images of confocal microscopy and two-photon microscopy of HepG2 cells labeled with

the three fluorescent probes were captured, along with differential interference contrast (DIC) micrographs. As shown in Figure 6, HepG2 cells have successfully uptaken three fluorescent probes and clearly emerged from cellular cytoplasm suggesting that the complexes penetrate the phospholipid bilayer of cellular membrane and closely associated with some parts of the cell.

Confocal fluorescence imaging reveals that T-1 exhibited observable punctate fluorescence around the perinuclear regions in the cell. To further confirm the T-1

subcellular distribution, a commercially available lysosome-specific staining probe (Figure S8) was used to costain cells with **T-1**. It showed that the distribution of **T-1** and Lyso-tracker were highly overlapped (overlapping degree 0.918, measured via ImageJ Plugin, Colocalization Finder), suggesting that **T-1** might have higher affinity binding/aggregate within cellular lysosome. Lysosomes were known to have proton-pumping vacuolar ATPases, which maintain the internal microenvironment at a pH range of 4.6–6.0. As shown in Figure S7, due to the low solubility in water, the fluorescence intensity of **T-1** is only about 50 in aqueous solution with pH = 7. However, when pH in the solution decreases to a range of 3.0–6.0, the fluorescence intensity increases to near 200 and stays with slight change. This means that **T-1** has relatively higher stability and solubility in this pH range. On this basis we speculated that **T-1** selectively concentrated in lysosomes might cause by the protonation of exposed nitrogen atom of imidazole ring, which has parallel mechanism to commercially available lysosome-specific staining probe [41].

For the imidazolium salts (**T-2** and **T-3**) uptake, it showed different cellular destination. The intense fluorescence was mainly evenly distributed in the HepG2 cell cytoplasm and excluded from nuclear region. This suggested the chromophores could label the cell cytoplasm of HepG2, due to their more hydrophobic nature, therefore the chromophores behaved higher distribution degree within aqueous intracellular microenvironment. This binding property might provide a useful tool for monitoring and investigating intracellular process, such as cargo sorting, organelle movement, cell division, and vesicular transportation in live tissue.

4. Conclusion

In this contribution, three imidazole derivatives were designed and synthesized. UV-vis absorption, single-photon fluorescence, two-photon absorption characters, and two-photon fluorescence microscopy (2PFM) are systematically investigated. It was discovered that there is almost no influence on the UV-vis absorption of the chromophores while varying with the polarity of the solvents. However, an obvious influence on their fluorescent spectra can be observed. On account of large 2PA cross sections in the near-IR region, the imidazolium derivatives can selectively stain cell well which make them potential bioimaging applications in the future.

Conflict of Interests

The authors declare that there is no conflict of interests regarding the publication of this paper.

Authors' Contribution

Yingzhong Zhu and Lufei Xiao contributed equally to this work.

Acknowledgments

This work was supported by a grant for the National Natural science Foundation of China (21271004, 51372003, 51432001, and 51271003), Ministry of Education Funded Projects Focus on Returned Overseas Scholar, Program for New Century Excellent Talents in University (China), Doctoral Program Foundation of Ministry of Education of China (20113401110004), Department of Education of Anhui province (KJ2014A190).

References

- [1] Y. Yang, Q. Zhao, W. Feng, and F. Li, "Luminescent chemodosimeters for bioimaging," *Chemical Reviews*, vol. 113, no. 1, pp. 192–270, 2013.
- [2] U. Resch-Genger, M. Grabolle, S. Cavaliere-Jaricot, R. Nitschke, and T. Nann, "Quantum dots versus organic dyes as fluorescent labels," *Nature Methods*, vol. 5, no. 9, pp. 763–775, 2008.
- [3] Z. Guo, S. Park, J. Yoon, and I. Shin, "Recent progress in the development of near-infrared fluorescent probes for bioimaging applications," *Chemical Society Reviews*, vol. 43, no. 1, pp. 16–29, 2014.
- [4] F. Lu and T. Nabeshima, "A highly selective and sensitive turn-on chemodosimeter for hypochlorous acid based on an iridium (iii) complex and its application to bioimaging," *Dalton Transactions*, vol. 43, no. 25, pp. 9529–9536, 2014.
- [5] H.-Y. Shiu, H.-C. Chong, Y.-C. Leung, T. Zou, and C.-M. Che, "Phosphorescent proteins for bio-imaging and site selective bio-conjugation of peptides and proteins with luminescent cyclometalated iridium(iii) complexes," *Chemical Communications*, vol. 50, no. 33, pp. 4375–4378, 2014.
- [6] J. Yu, X. Diao, X. Zhang et al., "Water-dispersible, pH-stable and highly-luminescent organic dye nanoparticles with amplified emissions for in vitro and in vivo bioimaging," *Small*, vol. 10, no. 6, pp. 1125–1132, 2014.
- [7] P. Sharma, S. Brown, G. Walter, S. Santra, and B. Moudgil, "Nanoparticles for bioimaging," *Advances in Colloid and Interface Science*, vol. 123–126, pp. 471–485, 2006.
- [8] Q. Liu, B. Guo, Z. Rao, B. Zhang, and J. R. Gong, "Strong two-photon-induced fluorescence from photostable, biocompatible nitrogen-doped graphene quantum dots for cellular and deep-tissue imaging," *Nano Letters*, vol. 13, no. 6, pp. 2436–2441, 2013.
- [9] Z. Yu, T. Y. Ohulchanskyy, P. An, P. N. Prasad, and Q. Lin, "Fluorogenic, two-photon-triggered photoclick chemistry in live mammalian cells," *Journal of the American Chemical Society*, vol. 135, no. 45, pp. 16766–16769, 2013.
- [10] B. Dumat, G. Bordeau, E. Faurel-Paul et al., "DNA switches on the two-photon efficiency of an ultrabright triphenylamine fluorescent probe specific of AT regions," *Journal of the American Chemical Society*, vol. 135, no. 34, pp. 12697–12706, 2013.
- [11] E. de Meulenaere, N. Nguyen Bich, M. de Wergifosse et al., "Improving the second-order nonlinear optical response of fluorescent proteins: the symmetry argument," *Journal of the American Chemical Society*, vol. 135, no. 10, pp. 4061–4069, 2013.
- [12] J. Xing, J. Liu, T. Zhang et al., "A water soluble initiator prepared through host-guest chemical interaction for microfabrication of 3D hydrogels via two-photon polymerization," *Journal of Materials Chemistry B*, vol. 2, pp. 4318–4323, 2014.
- [13] E. Zojer, D. Beljonne, P. Pacher, and J.-L. Brédas, "Two-photon absorption in quadrupolar π -conjugated molecules: influence

- of the nature of the conjugated bridge and the donor-acceptor separation," *Chemistry—A European Journal*, vol. 10, no. 11, pp. 2668–2680, 2004.
- [14] M. Albota, D. Beljonne, J.-L. Brédas et al., "Design of organic molecules with large two-photon absorption cross sections," *Science*, vol. 281, no. 5383, pp. 1653–1656, 1998.
- [15] R. J. Sundberg and R. B. Martin, "Interactions of histidine and other imidazole derivatives with transition metal ions in chemical and biological systems," *Chemical Reviews*, vol. 74, no. 4, pp. 471–517, 1974.
- [16] L. Kruidenier, C.-W. Chung, Z. Cheng et al., "A selective jumonji H3K27 demethylase inhibitor modulates the proinflammatory macrophage response," *Nature*, vol. 488, no. 7411, pp. 404–408, 2012.
- [17] S. Kumar, J. Boehm, and J. C. Lee, "P38 MAP kinases: key signalling molecules as therapeutic targets for inflammatory diseases," *Nature Reviews Drug Discovery*, vol. 2, no. 9, pp. 717–726, 2003.
- [18] D. Sharma, B. Narasimhan, P. Kumar et al., "Synthesis, antimicrobial and antiviral evaluation of substituted imidazole derivatives," *European Journal of Medicinal Chemistry*, vol. 44, no. 6, pp. 2347–2353, 2009.
- [19] H. Akdas-Kilig, T. Roisnel, I. Ledoux, and H. Le Bozec, "A new class of bipyrimidine-based octupolar chromophores: synthesis, fluorescent and quadratic nonlinear optical properties," *New Journal of Chemistry*, vol. 33, no. 7, pp. 1470–1473, 2009.
- [20] B. Liu, H.-L. Zhang, J. Liu, Y.-D. Zhao, Q.-M. Luo, and Z.-L. Huang, "Novel pyrimidine-based amphiphilic molecules: synthesis, spectroscopic properties and applications in two-photon fluorescence microscopic imaging," *Journal of Materials Chemistry*, vol. 17, no. 28, pp. 2921–2929, 2007.
- [21] P. Hrobárik, V. Hrobáriková, I. Sigmundová et al., "Benzothiazoles with tunable electron-withdrawing strength and reverse polarity: a route to triphenylamine-based chromophores with enhanced two-photon absorption," *The Journal of Organic Chemistry*, vol. 76, no. 21, pp. 8726–8736, 2011.
- [22] G. Wang, K.-Y. Pu, X. Zhang et al., "Star-shaped glycosylated conjugated oligomer for two-photon fluorescence imaging of live cells," *Chemistry of Materials*, vol. 23, no. 20, pp. 4428–4434, 2011.
- [23] R. Li, D. Li, W. Fei et al., "Synthesis, prodigious two-photon absorption cross sections and electrochemical properties of a series of triphenylamine-based chromophores," *Optical Materials*, vol. 36, no. 8, pp. 1281–1288, 2014.
- [24] W. Zhou, S. M. Kuebler, K. L. Braun et al., "An efficient two-photon-generated photoacid applied to positive-tone 3D microfabrication," *Science*, vol. 296, no. 5570, pp. 1106–1109, 2002.
- [25] T.-C. Lin, C.-Y. Liu, M.-H. Li et al., "Synthesis and characterization of a highly two-photon active dendrimer derived from 2,3,8-trifunctionalized indenoquinoxaline units," *Journal of Materials Chemistry C*, vol. 2, no. 5, pp. 821–828, 2014.
- [26] Z. Zheng, Z. Yu, M. Yang et al., "Substituent group variations directing the molecular packing, electronic structure, and aggregation-induced emission property of isophorone derivatives," *The Journal of Organic Chemistry*, vol. 78, no. 7, pp. 3222–3234, 2013.
- [27] C. Tang, Q. Zhang, D. Li et al., "Synthesis, crystal structures, two-photon absorption and biological imaging application of two novel bent-shaped pyrimidine derivatives," *Dyes and Pigments*, vol. 99, no. 1, pp. 20–28, 2013.
- [28] X. Y. Shen, Y. J. Wang, E. Zhao et al., "Effects of substitution with donor-acceptor groups on the properties of tetraphenylethene trimer: Aggregation-induced emission, solvatochromism, and mechanochromism," *The Journal of Physical Chemistry C*, vol. 117, no. 14, pp. 7334–7347, 2013.
- [29] B. Liu, Q. Zhang, H. J. Ding et al., "Synthesis, crystal structures and two-photon absorption properties of a series of terpyridine-based chromophores," *Dyes and Pigments*, vol. 95, no. 1, pp. 149–160, 2012.
- [30] B. Wang, Y. C. Wang, J. L. Hua et al., "Starburst triarylamine donor-acceptor-donor quadrupolar derivatives based on cyano-substituted diphenylaminestryrylbenzene: tunable aggregation-induced emission colors and large two-photon absorption cross sections," *Chemistry—A European Journal*, vol. 17, no. 9, pp. 2647–2655, 2011.
- [31] J. P. Richard, T. L. Amyes, L. Bei, and V. Stubblefield, "The effect of β -fluorine substituents on the rate and equilibrium constants for the reactions of α -substituted 4-methoxybenzyl carbocations and on the reactivity of a simple quinone methide," *Journal of the American Chemical Society*, vol. 112, no. 26, pp. 9513–9519, 1990.
- [32] M. Y. Berezin and S. Achilefu, "Fluorescence lifetime measurements and biological imaging," *Chemical Reviews*, vol. 110, no. 5, pp. 2641–2684, 2010.
- [33] S. A. Patel, M. Cozzuol, J. M. Hales et al., "Electron transfer-induced blinking in Ag nanodot fluorescence," *The Journal of Physical Chemistry C*, vol. 113, no. 47, pp. 20264–20270, 2009.
- [34] S. Ji, J. Yang, Q. Yang, S. Liu, M. Chen, and J. Zhao, "Tuning the intramolecular charge transfer of alkynylpyrenes: effect on photophysical properties and its application in design of OFF-ON fluorescent thiol probes," *The Journal of Organic Chemistry*, vol. 74, no. 13, pp. 4855–4865, 2009.
- [35] M. Schaffroth, B. D. Lindner, V. Vasilenko, F. Rominger, and U. H. F. Bunz, "Alkynylated diazadioxacenes: syntheses and properties," *The Journal of Organic Chemistry*, vol. 78, no. 7, pp. 3142–3150, 2013.
- [36] A. Jiménez-Sánchez, M. Rodríguez, R. Métivier et al., "Synthesis and crystal structures of a series of Schiff bases: a photo-, solvato- and acidochromic compound," *New Journal of Chemistry*, vol. 38, no. 2, pp. 730–738, 2014.
- [37] F. Han, L. Chi, W. Wu, X. Liang, M. Fu, and J. Zhao, "Environment sensitive phenothiazine dyes strongly fluorescence in protic solvents," *Journal of Photochemistry and Photobiology A: Chemistry*, vol. 196, no. 1, pp. 10–23, 2008.
- [38] M. Irie and K. Sayo, "Solvent effects on the photochromic reactions of diarylethene derivatives," *The Journal of Physical Chemistry*, vol. 96, no. 19, pp. 7671–7674, 1992.
- [39] X. Li, X. Zhang, W. Li et al., "Synthesis and enhanced two-photon absorption properties of tetradonor-containing anthracene-centered 2-D cross-conjugated polymers," *Journal of Materials Chemistry*, vol. 21, no. 11, pp. 3916–3924, 2011.
- [40] Q. Q. Li, J. Huang, Z. G. Pei et al., "Synthesis and two-photon absorption properties of conjugated polymers with N-arylpyrrole as conjugated bridge and isolation moieties," *Journal of Polymer Science, Part A: Polymer Chemistry*, vol. 49, no. 12, pp. 2538–2545, 2011.
- [41] H. Zhu, J. Fan, Q. Xu et al., "Imaging of lysosomal pH changes with a fluorescent sensor containing a novel lysosome-locating group," *Chemical Communications*, vol. 48, no. 96, pp. 11766–11768, 2012.

Research Article

Development of the 1.2 T~1.5 T Permanent Magnetic Resonance Imaging Device and Its Application for Mouse Imaging

Guangxin Wang,¹ Huantong Xie,² Shulian Hou,¹ Wei Chen,¹ Qiang Zhao,¹ and Shiyu Li¹

¹College of Science, Hebei United University, Tangshan 063000, China

²Shanghai Shining Global Science and Education Equipment Co., Ltd., Shanghai 201806, China

Correspondence should be addressed to Shulian Hou; houshulian@163.com

Received 20 October 2014; Revised 14 December 2014; Accepted 14 December 2014

Academic Editor: Jiangbo Yu

Copyright © 2015 Guangxin Wang et al. This is an open access article distributed under the Creative Commons Attribution License, which permits unrestricted use, distribution, and reproduction in any medium, provided the original work is properly cited.

By improving the main magnet, gradient, and RF coils design technology, manufacturing methods, and inventing new magnetic resonance imaging (MRI) special alloy, a cost-effective and small animal specific permanent magnet-type three-dimensional magnetic resonance imager was developed. The main magnetic field strength of magnetic resonance imager with independent intellectual property rights is 1.2~1.5 T. To demonstrate its effectiveness and validate the mouse imaging experiments in different directions, we compared the images obtained by small animal specific permanent magnet-type three-dimensional magnetic resonance imager with that obtained by using superconductor magnetic resonance imager for clinical diagnosis.

1. Introduction

Magnetic resonance imaging (MRI) can provide nondestructive and high quality CT images that are superior to images yielded by other devices. MRI has been widely used in a series of realms, such as pathology, physiology, and pharmacology. It has brought medical researches into a new era. Due to the complexity of human diseases, many experiments cannot be applied to patients directly. Thus, small animal models are used to simulate the clinical condition of the human body and then applied in medical and clinical researches [1].

Although the animal model MRI in China is still in its infant stage [2], molecular geneticists are doing their best to use animal models to simulate human diseases. In order to develop new drugs and dosage forms, the pharmaceutical industry needs a lot of transgenic or gene-deficient mice as reliable candidates of in vivo detection. Since the transgenic mice are very expensive, traditional monitoring methods such as histomorphology examination are cost-ineffective. Fortunately, MRI technology is becoming mature. Owing to its noninvasion and replicability, MRI technology can help us to save the cost and get encouraging results. Of course, there are great differences between a 20 g mouse and a 70 kg person

[3]. When we investigate the mice using the MRI technique which is used for investigations of human body, we will face a dilemma, that is, high cost and poor image quality.

In other countries, scientists have already invented superconductive MRI techniques for the dedicated small animals, which have a dedicated coil with the field strength up to 7.0 T [4]. However, this technique has higher operating costs and it is only used in research without the high cost recovery. Many scientific research institutes and universities cannot afford to operate it. Therefore, there is only a very small amount of such MRI devices in China. Although the technology of permanent magnet device is complex, its cost is low and there are no operating costs. Hence, permanent magnet machine will be the mainstream products for developing countries and regions in a long time. Recently, many research institutes in China began to study the principles of permanent MRI. However, there are only few reports about the application of this technology to manufacture products. Moreover, products with the independent intellectual property are rare. In this paper, we will present the permanent MRI Series (1.2~1.5 T) which is developed by Shanghai Huan Tong Science and Education Equipment Co., Ltd., and Hebei United University.

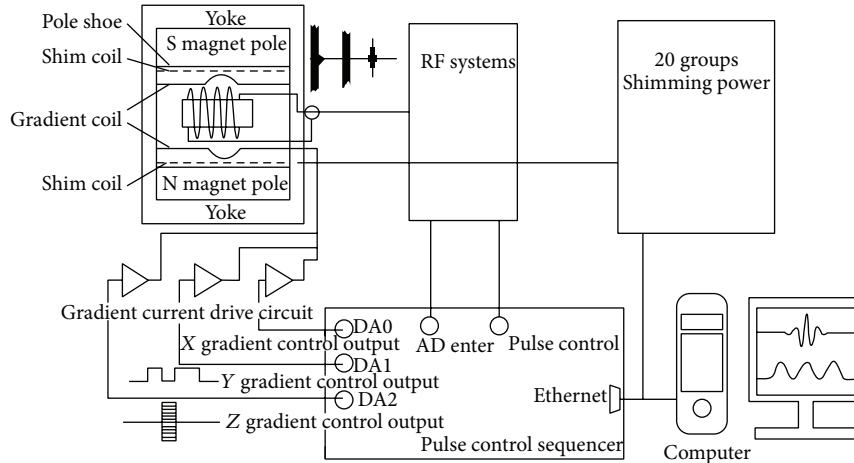


FIGURE 1: Schematic diagram of MRI structure.

2. Materials and Methods

2.1. Materials. 50 N, BH 50 MG Nd-Fe-B steel, gradient coils RF coils, and 12 healthy male mice used in our study were obtained from Shanghai Experimental Animal Center. They are all 4 weeks old with the weight between 17 and 20 grams. The dosage of urethane anesthesia injected into the healthy male mice abdominal is 1 g/kg. The imaging scan was performed 5 minutes later. As a control group, another two Kunming mice (one of them as a spare) with the weight of 20 grams were selected. The abdominal injection of 10% chloral hydrate was performed. Three minutes later, the coronal and sagittal scanning was carried out by using the human body superconducting 1.5 T MRI machine with FOV 100×100 mm. The schematic diagram of MRI structure is depicted in Figure 1.

2.2. Main Magnet System. As a major component of the MRI device, main magnet system which directly affects the image quality is the key indicators to the entire imaging system. The permanent magnet system used 50 MG energy product Nd-Fe-B magnets. By using numerical analysis and referring to the related references [5–10], we calculated the magnetic pole size depending on the circumstances and obtained the strongest magnetic field with the minimum size.

According to MRI theory, main magnetic field must be uniform. However, the main magnet after that processing cannot meet the requirement. Uniform magnetic fields are mentioned in [8, 9, 11]. Shimming method is firstly proposed by Wenston Anderson in his work [10], in which it gives us the details of the active shim technology. Later on, Dorri et al. described the details of superconducting magnets for passive shim technology [12]. With the development of MRI technology, passive shim technology research is constantly improved [13, 14] especially after the emergence of permanent magnet devices. Our research focused on passive shim technology and combined the use of active and passive shim methods. We impose x , y , z , R^2 , $x^2 - y^2$, R^3 , R^2z , y^3 , and xyz , and other shim coils to build active shim technology. Passive shim technology is built by the complex processing technology including the

calculation through the high-precision calculation, the point by point precision measurement, and subnanometer manual processing technology. We developed measurement mold point by point and choose 2048 measuring point number for measuring accurately and continuously.

Main magnet which is made of sintered Nd-Fe-B permanent magnetic materials has the high magnetic property, but the temperature stability of sintered Nd-Fe-B is poor and it is greatly influenced by environmental temperature [5]. One reason is that the permanent magnet geometry parameters will change with the variation of temperatures. On the other hand, the uniformity of the magnetic field and magnetic field strength are also temperature dependent. Therefore, we cannot get any images. To overcome the disadvantages of poor temperature stability of the permanent magnet, stimulated by the electronic equipment “self-locking” control technology, we developed a self-locking circuit to control the floating of main magnet field strength caused by temperature changes and obtained a steady magnetic field. We have developed the main magnet with independent intellectual property rights, and the main magnetic structures are as follow: the magnet gap is less than 70 mm, the magnetic field strength is 1.2~1.5 T, the diameter of the spherical space is less than 60 mm, the uniformity is 1~0.5 ppm, and the weight is less than 1200 kg.

2.3. Gradient Coils and Gradient Field. Shim coils are composed of many directions, namely, x , y , z , R^2 , $x^2 - y^2$, R^3 , R^2z , y^3 , and xyz , of which the three coils in x , y , and z directions are used as gradient coils. There is a certain gradient because the magnetic field after the passive shim is uneven. When the gradient coil magnetic field just offsets the gradient magnetic field of the magnet itself in a certain direction, the gradient coil can be regarded as a shim coil. Therefore, we need to set gradient coils at zero for adjusting the resonant frequency. When the resonance frequencies of different positions are identical and the magnetic field is uniform mostly, we can get the best result of maximum resonance amplitude and resonance signal. According to this principle, we developed adjusting computer software which

can be used through the interface buttons to achieve uniform field debugging. We can measure the time stability of the magnetic field as Larmor drift frequency of Hertz per hour. The instrument in this study does not exceed 100 Hz/h. There are a lot of studies of the gradient coil design [15–19] and the permanent magnet-type magnetic field gradient coils [20]. Our study aimed to design self-shielded gradient coils surface with the wavy surface structure. And the new device has the advantages of low eddy current, high efficiency, and high linearity.

2.4. RF Coil for Transmitting and Receiving a Signal. RF coil (RF) is used to transmit and receive signal. In order to get the high quality image, the transmitting coil requires not only a faster and higher efficiency of energy conversion but also a uniform RF field that can guarantee the uniform intensity of biological samples. It is essential for receiving coil to have a higher detection sensitivity and ability to reflect the tissue adjacent to the appropriate minor differences so that it can guarantee sufficient signal-to-noise ratio. Only images that can reflect minor differences within the same organization and different organizations in terms of gray difference with distinguishable resolutions are useful. But it cannot simultaneously satisfy the transmitting coil high uniformity and high sensitivity and high signal-to-noise ratio of the receiving coil. According to Biot-Savart law, the magnetic field strength is inversely proportional to the square of the distance. The smaller the distance between the coil and the sample is, the stronger the magnetic field is, and the poorer the uniformity of the RF is. If we divide it into two groups of coils, they will be coupled with each other and lead to the reduction of signal-to-noise ratio. Therefore, the optimization of RF coil has been one of the hot issues in the research of MRI [21, 22]. The shape of the coil has been considered to be the most important factor affecting the coil quality [23]. Our designed RF coil absorbs the advantage which the saddle shaped coil can provide the uniform RF field in the vertical direction of main magnetic field. It also absorbs the advantage of high sensitivity and uniformity field from the solenoid coil. Theoretically, the transmission and acquisition are two groups of coils. In order to save valuable space of main magnetic field, they are integrated together. The current direction is controlled through the circuit, so that the deformation is equivalent to the saddle shaped coil signal transmission along the x -axis. The received signal is equivalent to the solenoid coil deformation along the z -axis. Thus, the transmitting and receiving signals are orthogonal and without coupling interferences. In order to eliminate the nonuniformity of the launch site, we employed the weighted correction method. By using our revised computer software [24], we obtained the brightness distribution function of the water mode image and then divided it by the function of the actual image. By setting a RF coil into 4 groups of coils in parallel as shown in Figures 2 and 3, we can reduce resistance and loss and increase the magnetic field uniformity and the sensitivity of the coils.

RF coil is fixed on the main magnet cavity, which produces hard and soft pulses. The frequency of RF coil has the adjustment range of 0 to 70 MHz with adjustment accuracy in the step of 0.01 Hz. Since the DDS technology is used, the frequency will have a high stability (10^{-8}).

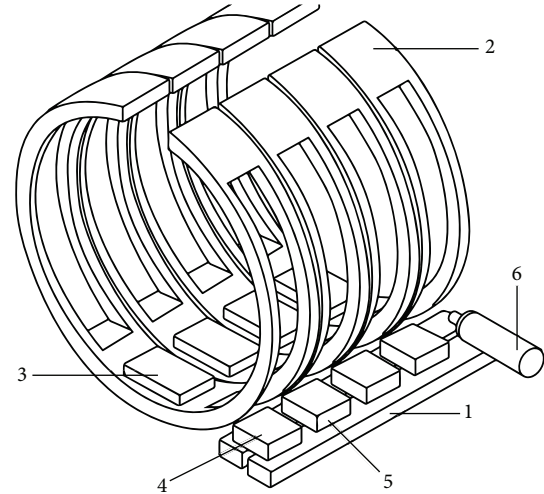


FIGURE 2: A schematic diagram of the RF coil structure, “1”: backbone transmission wires, “2”: four segments of the coil, “3”: resonant capacitor, “4”: decoupling capacitor, “5”: coupling capacitor, and “6”: wiring as input-output interface with the circuit connection.

2.5. Mouse Imaging. The instrument parameters are as follows: (1) the main magnetic field strength is 1.5 T, shimming volume diameter 35 mm ball, SE weighted T1 sequence, TR = 100 ms, TE = 15.5 ms, and FOV 35×35 mm; (2) the main magnetic field strength is 1.2 T, shimming volume diameter 60 mm ball, SE weighted T1 sequence, TR = 100 ms, TE = 15.5 ms, and FOV 50×60 mm. Number of excitations NEX = 2.

Cross-sectional scanning is as follows: (x and y directions phase codes, z direction frequency code) data matrix is $32 \times 512 \times 256$ and image matrix is 1024×1024 . And coronal section scanning is as follows: data matrix is $32 \times 512 \times 256$ and image matrix is 512×512 . We completed T1-weighted images as scan mode 3D, the sinc RF pulse. The 12 healthy male mice we used in this study were obtained from Shanghai Experimental Animal Center. They are 4 weeks old with the weight between 17 and 20 grams. The dosage of urethane anesthesia injected into the healthy male mice abdominal is 1 g/kg. The imaging scan was performed 5 minutes later. As a control group, another two Kunming mice (one of them as a spare) with the weight of 20 grams were selected. The abdominal injection of 10% chloral hydrate was performed. Three minutes later, the coronal and sagittal scanning was carried out by using the human body superconducting 1.5 T MRI machine with FOV 100×100 mm.

2.6. Phantom Making. Two water plexiglass cylindrical molds containing 0.3% aqueous solution were made. One is with a diameter of 22 mm and height of 30 mm, the other is with a diameter of 48 mm and height of 60 mm.

3. Results

The self-developed instrument is a device which is very complex, having not only the magnetic system of high quality but also a software system of high quality, research and development of computer integration software, and other

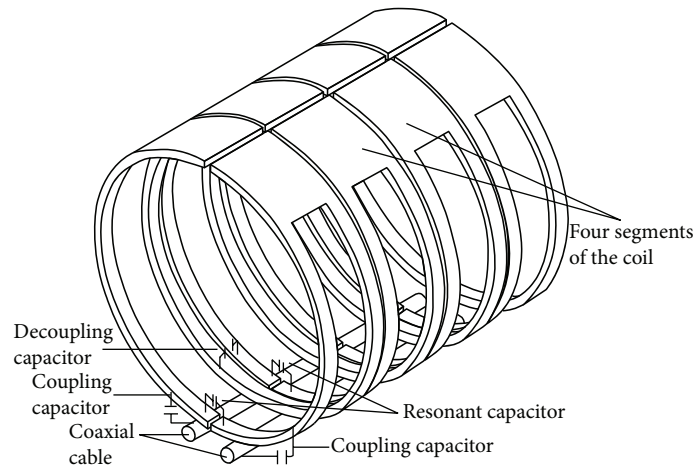


FIGURE 3: RF coil capacitor connection mode.

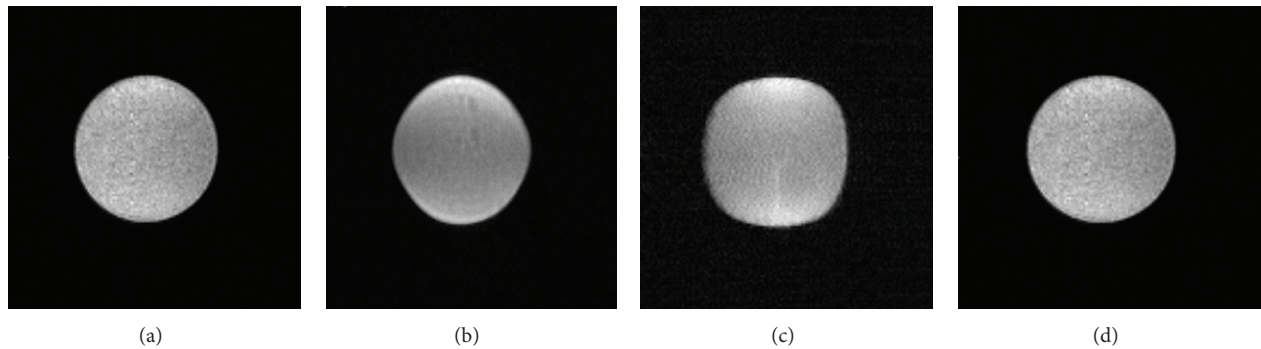


FIGURE 4: Comparison of axial T1-weighted phantom images with different linearity of gradient field: (a) nonlinearity 0.3%; (b) nonlinearity 5%; (c) nonlinearity 10%; (d) RF coil phantom image 48 mm aperture, 1.2 T.

supporting devices. The software includes the computer control system and the order of accuracy control, release, and storage and accepts a programmable pulse sequence generator, pulse sequence control, image data acquisition and control, data processing system, and signal visualization system. We also successfully developed other types of equipment such as the preamplifier, power amplifier, switch circuit, 3D display software, and 3D NMR integration software [24]. A series of 1.2 T~1.5 T MRI instrument was developed. Select the two instruments for imaging experiments: in the first instrument the magnetic pole gap is 42 mm, weight 400 kg, the magnetic field strength 1.5 T, and shimming 35 mm diameter spherical volume of space, and in the second instrument the magnetic pole gap is 70 mm, weight 1200 kg, the magnetic field strength 1.2 T, and shimming 60 mm diameter spherical volume of space.

3.1. Phantom Imaging. In order to determine the gradient field suitable linearity of the permanent magnetic field, phantom image suitable gradient field was obtained through computer simulation [24] and phantoms adjustments. Figure 4 shows phantom images: (a) nonlinearity 0.3%, (b) nonlinearity 5%, and (c) nonlinearity 10%.

We further improved the uniformity of the RF field through the water mask weighted imaging correction (RF coil

research and development (R & D)). In order to ensure the quality of image, the brightness distribution of computer software is divided by the field. The final phantom image is shown in Figure 4(d). As shown in Figure 4(d), a homogeneous solution state without distortion was well demonstrated.

3.2. Mice Image. In this study, the three-dimensional imaging technology was employed. Therefore, we can achieve continuous acquisition of a magnetic resonance signal, make the slices closely co-coordinated, and overcome the problem of signal leakage between slices. In order to stimulate the entire slices of blocks at the same time, we put RF pulse width as 50 KHz, which can greatly shorten the pulse duration and reduce the TE, which further reduced the relaxation of the signal loss and yielded a higher signal-to-noise ratio (SNR). Thus, we can get high quality images in the moderate intensity field (1.2~1.5 T). We obtained similar images by using different mice and different test time. This result indicates that the performance of the developed instrument is repeatable and stable. In each test, the number of slices is 128. The chest and abdomen imaging is obtained by cross-sectional scans (imager: 1.5 T, 35 mm) with the slice thickness of 0.3 mm and is shown in Figure 5. Figure 5 shows the axial T1-weighted mouse images. Although they are not as clear as the high-field picture, at the level from the chest to abdomen,

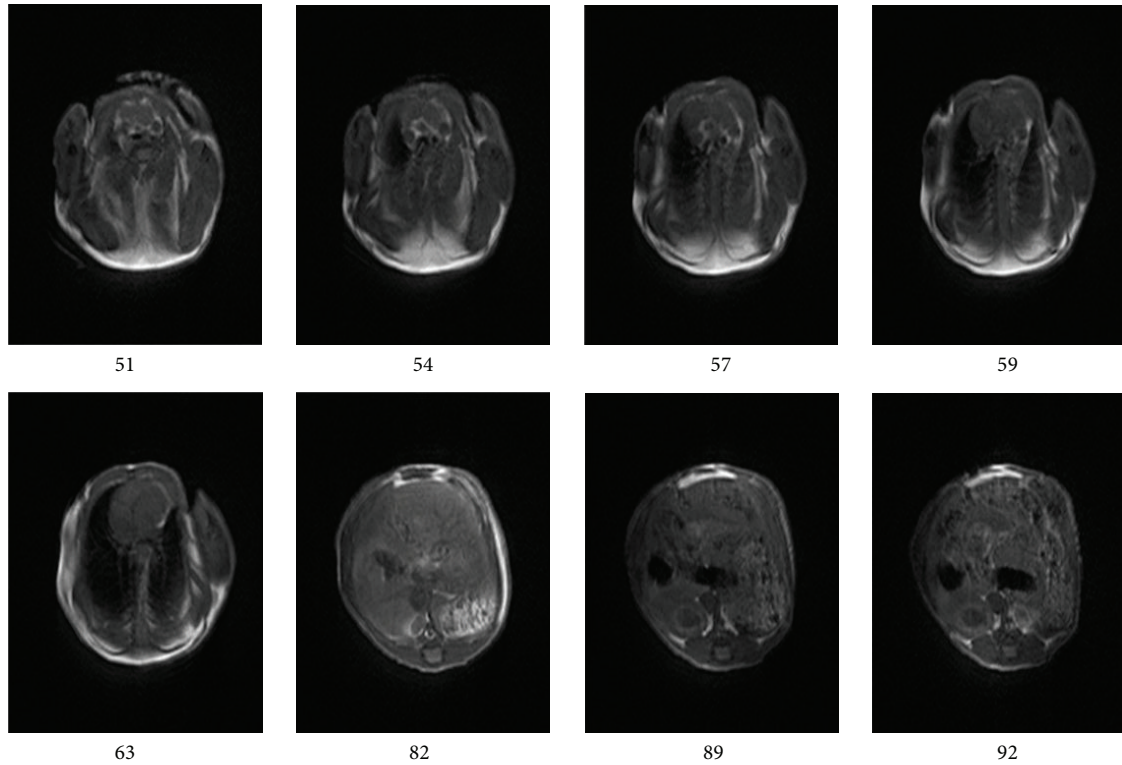


FIGURE 5: The eight axial T1-weighted mouse images, thoracic abdominal segment levels. Internal organs were clearly observed (1.5 T, 35 mm).

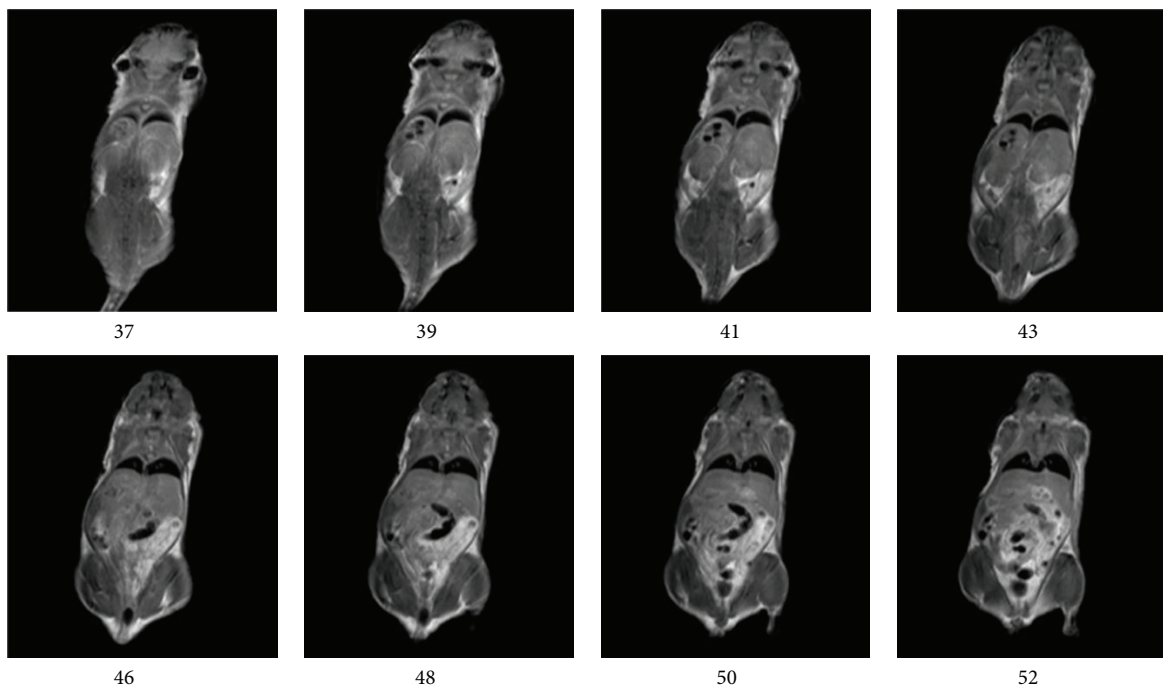


FIGURE 6: The 8 coronal T1-weighted images, all clear images from head to tail were clearly obtained (1.2 T, 60 mm).

the stomach, the large intestine, muscles, jejunum, cecum, heart, vertebra, and spinal cord could all be well observed. The body image is obtained by coronal scans (imager: 1.2 T, 60 mm) with the slice thickness of 0.4 mm and is shown in Figure 6. Figure 6 shows 8 coronal T1-weighted images,

all of which are relatively clear images from the head to the tail of mouse. In addition, it is possible to distinguish clearly anatomical structures including the muscles, brain, ear, kidney, liver, stomach, jejunum, cecum, and internal organs and, overall, the entire body of the mouse was seen on

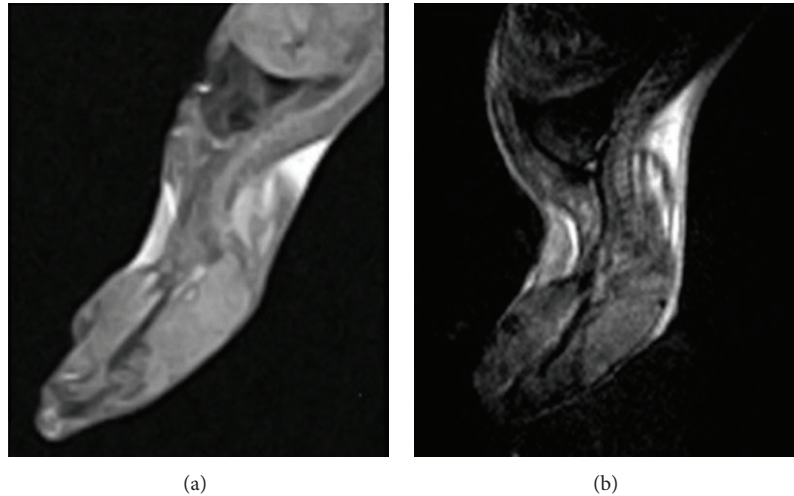


FIGURE 7: Comparison with human body's superconducting instrument. The left figure is obtained using human device, and the right is obtained in this study.

one image homogeneously, and the digital under the picture indicates the order to be cut.

4. Discussion

4.1. Field System. In this study, the development of the magnetic field system is based on previous micromagnetic resonance imaging teaching instrument. The magnetic system is the most important part of MRI, especially the main magnetic field intensity and uniformity. For the permanent magnet type, the improvement of the core magnetic field strength depends on the techniques of alloy. For shimming, in the same magnetic field uniformity, the stronger the main magnetic field is, the greater the bias of magnetic field is. The passive shimming is more detailed. The active shimming of 60 mm aperture may achieve the third-order shimming by applying 20 groups shim coils; therefore, the nonlinearity of the magnetic field can attain 0.8 ppm, and the image quality has been greatly improved.

Since the size of mouse is small, in order to get clear images showing details of the internal organization, we must choose thin slice (0.5 mm or less). Therefore, the requirement of the gradient field linearity should be much higher than that proposed in the literature (<5%) [7]. In this study, the linearity is 0.3%. Since the imaging quality is affected by the linearity of the gradient field, the methods of how to determine the linearity of the gradient field have been discussed in the past [25]. However, when the primary magnetic field strength is 1.5 T, the presence of the pole shoe and the yoke of ferromagnetic material can lead to the dramatic increase of eddy current. Therefore, the coil can not solve the self-shielding properties. By improving the pole shoe blocking-up magnetic induction, the eddy currents control is in the acceptable range.

Instead of the conversion ratio of signal to noise, previous studies paid more attention to the coil Q value. However, we realize that the most important is the coil sensitivity. The higher the sensitivity, the better the signal-to-noise ratio,

which is the basis of yielding the high resolution images. However, the sensitivity is determined by the induction coupling degree and resistance coupling efficiency. Impedance coupling efficiency comprises a coil resistance, sample conductivity decay. Since the conductivity of small animals is higher than human beings, the detected signal will be dramatically decrease. Absorption of phased array coil advantage [26], with small coils which are combined into a large coil, on one hand reduces the resistance of the coil to reduce the loss and on the other hand is decomposed into multiple small coils which are combined together, and the received signals overlap with each other to reduce reflection loss and improve the sensitivity of the coil. The invention of the connection of alloy for high conductive MRI [27] for coil production, between the various components, further reduces the loss. Coil using single channel retains the advantages of low noise single coil, avoiding the multichannel acquisition for the elimination of small coil coupling and acquire complex matching circuit. Our equipment is different from that of conventional RF coil (keel single channel RF coil) [28]. Our equipment retains not only the phased array coil and high filling rate and high sensitivity, but also the single channel properties of body coil as shown in Figure 3. The main characteristics and advantages of the novel equipment are as follows: the load coil Q value decreased slightly; the signal sensitivity is two times higher than other signal interfaces; single input and output interface features, and coils in the equipment can mutually inductance and decouple.

4.2. Comparison with Human Body's Superconducting Instrument. We used the superconducting 1.5 T device with the data matrix 256×256 , TI = 750.0 ms, TR = 2118.8 ms, and TE = 10.7 ms. We selected minimal wrist surface coil in our hospital and chose the thinnest slice of 3 mm. The T1-weighted images are shown in the left of Figure 7. And the image on the right of Figure 7 is the image obtained by the instrument used in our studies. Because of different position in the machine, mouse is supine in the human body's

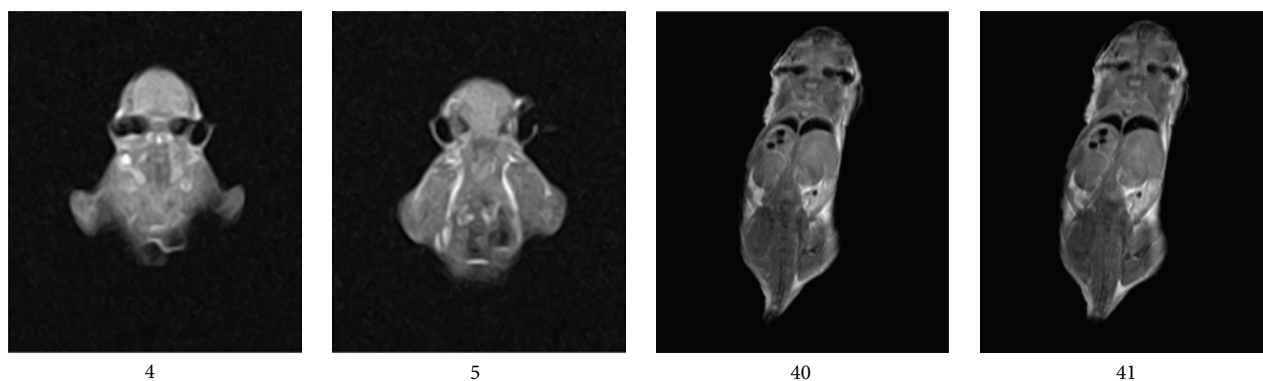


FIGURE 8: Comparing the slice jump between the fourth and fifth slices with thickness of 3 mm and the fortieth and forty-first slices with thickness of 0.4 mm.

machine. But in this study, mice were hanging upside down in a magnetic field. The sagittal planes have made a different width under the action of the gravity. Thus, we can only take roughly the same level compared with the position. Figure 7 shows that the human body's MRI device has a very good signal-to-noise ratio. But it cannot distinguish the details. Therefore, if the human body's device is with no special configuration, it cannot be directly used for mouse imaging. On the other hand, wrist coil is too large for a mouse, but the coil is too expensive, and the coils dedicated to a small animal in general hospital generally cannot be configured. The body's tissues and organs are larger, so we generally select the thinnest slice of 3 mm. However, there still exist the following three problems. The 3 mm is too thick mice. There are imaging slice gaps for 2D imaging. The change of imaging slice gaps is so fast that it is inconvenient for further researches. Therefore, 3D imaging can be a very good solution to this problem. In this study, the slice of cutting mouse head is about 60 slices. Figure 8 shows the fourth and fifth slices with thickness of 3 mm and the fortieth and forty-first slices with thickness of 0.4 mm, respectively. Human device is not easy to be used directly on mice, and the general research institutes cannot afford the cost. Therefore, the development of permanent significance of small animal MRI is urgent.

For the convenience of the vast majority of experimental scientists, we developed a suite of software package to help users to get the desired results. The software package includes the computer control system and the order of accuracy control, release, and storage and accepts a programmable pulse sequence generator, pulse sequence control, image data acquisition and control, data processing system, signal visualization system, the preamplifier, power amplifier, switch circuit, and 3D display software [24].

5. Summary

In summary, the study of 1.2~1.5 T permanent MRI obtained a preliminary success. We can see that the tissues and organs of the head or abdomen and the body of the mouse can be clearly distinguished (Figures 6 and 7). But for the levels close to the initial or end of the slice, there is high noise so that we cannot observe the organizational structure. This is due

to the fact that our uniform field space is spherical with a diameter of 35 mm (1.5 T) and 60 mm (1.2 T) space but not a cylindrical space. In addition, the SNR decreases along with the increase of RF coil size. The best performance can be obtained at the spiral coil intermediate position, where the SNR achieved the highest value. Because it is three-dimensional imaging, we can adjust the position of mouse in the main magnetic field to the best region of interest. But there are still some shortcomings. Firstly, there is only T1-weighted for the relatively mature sequence, and T2-weight images are not stable enough in vivo. Since T2-weighted is widely used in disease analysis, we will develop more imaging sequence in the future. Secondly, we will improve mouse fixtures and unify the mouse body so that the image will be more comparable.

Conflict of Interests

The authors declare that there is no conflict of interests regarding the publication of this paper.

Acknowledgment

This work was supported by the Hebei Science and Technology Agency (08202133D and 13202001D).

References

- [1] D. Sappey-Marini er, O. Beuf, C. Billotey et al., "The ANIMAGE project: a multimodal imaging platform for small animal research," *Nuclear Instruments and Methods in Physics Research, Section A: Accelerators, Spectrometers, Detectors and Associated Equipment*, vol. 527, no. 1-2, pp. 117-123, 2004.
- [2] M. X. Zhang and J. S. Wang, "Study progress on animal model for tumor imaging," *Chinese Journal of Current Advances in General Surgery*, vol. 10, no. 6, pp. 520-523, 2007.
- [3] W. L. Zheng and S. Zheng, *Application and value of micromagnetic resonance imaging in the experimental study of oncology [Ph.D. students dissertation]*, 2007, volume 1, pp: 4-5.
- [4] X. Chen, J. F. Lei, Y. Y. Zhao, and J. L. Zhang, "7.0T small animal magnetic resonance imaging instrument facilities construction," *Computers and Applied Chemistry*, vol. 31, no. 2, pp. 141-145, 2014.

- [5] S. Z. Zhou and Q. F. Dong, *Super Permanent Magnet: Rare Earth Iron Series Permanent Magnet*, vol. 1, Metallurgical Industry Press, Beijing, China, 2004.
- [6] P. C. Ji, *Permanent Magnet Mechanism*, Beijing University of Technology Press, 2000.
- [7] H. T. Xie, "Nuclear magnetic resonance magnet equipment," *China Patent*, no. 01276446, 2002.
- [8] M. Cavenago and M. F. Moiso, "Iron shimming of superconductive rotating dipoles," *IEEE Transactions on Magnetism*, vol. 30, no. 4, pp. 1923–1926, 1994.
- [9] G. T. Danby and J. W. Jackson, "Shimming techniques for the ultraprecise muon g-2 storage ring at the AGS," *IEEE Transactions on Magnetism*, vol. 30, no. 4, pp. 1710–1713, 1994.
- [10] W. A. Anderson, "Electrical current shims for correcting magnetic fields," *The Review of Scientific Instruments*, vol. 32, no. 3, pp. 241–250, 1961.
- [11] R. Vodovic, "Magnetic field correction using magnetized shims," *IEEE Transactions on Magnetism*, vol. 25, no. 4, pp. 3313–3319, 1989.
- [12] B. Dorri, M. E. Vermilyea, and W. E. Toffolo, "Passive shimming of MR magnets. Algorithm, hardware, and results," *IEEE Transactions on Applied Superconductivity*, vol. 3, no. 1, pp. 254–257, 1993.
- [13] L. Wang, *The passive shimming technique research a special application of the permanent magnet [M.S. thesis]*, Shenyang University of Technology, Shenyang, China, 2007.
- [14] Y. Zhang, D. Xie, B. Bai, H. S. Yoon, and C. S. Koh, "A novel optimal design method of passive shimming for permanent MRI magnet," *IEEE Transactions on Magnetism*, vol. 44, no. 6, pp. 1058–1061, 2008.
- [15] E. M. Haacke, R. W. Brown, M. R. Thompson, and R. Venkatesan, *Magnetic Resonance Imaging: Physical Principles and Sequence Design*, Wiley-Liss Publisher, New York, NY, USA, 1st edition, 1999.
- [16] B. J. Fisher, N. Dillon, T. A. Carpenter, and L. D. Hall, "Design of a biplanar gradient coil using a genetic algorithm," *Magnetic Resonance Imaging*, vol. 15, no. 3, pp. 369–376, 1997.
- [17] A. M. Peters and R. W. Bowtell, "Biplanar gradient coil design by simulated annealing," *Magnetic Resonance Materials in Physics, Biology, and Medicine*, vol. 2, no. 3, pp. 387–389, 1994.
- [18] D. Tomasi, E. C. Caparelli, H. Panepucci, and B. Foerster, "Fast optimization of a biplanar gradient coil set," *Journal of Magnetic Resonance*, vol. 140, no. 2, pp. 325–339, 1999.
- [19] L. K. Forbes and S. Crozier, "Novel target-field method for designing shielded biplanar shim and gradient coils," *IEEE Transactions on Magnetism*, vol. 40, no. 4, pp. 1929–1938, 2004.
- [20] W. Liu, D. Zu, X. Tang, and H. Guo, "Target-field method for MRI biplanar gradient coil design," *Journal of Physics D: Applied Physics*, vol. 40, no. 15, pp. 4418–4424, 2007.
- [21] J. W. Carlson and L. Kaufman, "Radio frequency coil for magnetic resonance imaging system—comprises a high strength, stiff internally self-supporting conductor formed into a radio frequency resonant coil," Toshiba America MRI Inc (TOKE), US, no. 1997883083A 19970626, 2013.
- [22] A. Trakic, H. Wang, E. Weber et al., "Image reconstructions with the rotating RF coil," *Journal of Magnetic Resonance*, vol. 201, no. 2, pp. 186–198, 2009.
- [23] P. T. While, L. K. Forbes, and S. Crozier, "An inverse method for designing loaded RF coils in MRI," *Measurement Science and Technology*, vol. 17, no. 9, pp. 2506–2518, 2006.
- [24] H. T. Xie, *Huantong Three-Dimensional NMR Integration Software Integration*, No. 2012SRO03945, National Copyright Administration of People's, Republic of China Computer Software Copyright, 2012.
- [25] S. L. Hou, H. T. Xie, X. W. Hou, S. Y. Li, and W. Chen, "Gradient coil of permanent magnet mini-magnetic resonance imager and image quality," *Chinese Journal of Magnetic Resonance*, vol. 29, no. 4, pp. 508–520, 2012.
- [26] T. W. Peter, K. F. Larry, and C. Stuart, "An inverse method for designing RF phased array coils in MRI—theoretical considerations," *Measurement Science and Technology*, vol. 18, no. 1, pp. 245–259, 2007.
- [27] H. T. Xie, "Special alloy with a magnetic resonance spectrometer and its preparation method," China Patent no. ZL 201110250105.9, 2011.
- [28] H. T. Xie, "An RF coil for magnetic resonance imaging apparatus," China Patent, no. ZL 20112032 5257.6, 2012.

Research Article

Expression of HE4 in Endometrial Cancer and Its Clinical Significance

Xiao Li, Yiping Gao, Mingzi Tan, Huiyu Zhuang, Jian Gao, Zhenhua Hu, Huimin Wang, Liancheng Zhu, Juanjuan Liu, and Bei Lin

Department of Obstetrics and Gynecology, Shengjing Hospital of China Medical University, Shenyang, Liaoning 110004, China

Correspondence should be addressed to Bei Lin; linbei88@hotmail.com

Received 11 December 2014; Accepted 11 January 2015

Academic Editor: Xuanjun Zhang

Copyright © 2015 Xiao Li et al. This is an open access article distributed under the Creative Commons Attribution License, which permits unrestricted use, distribution, and reproduction in any medium, provided the original work is properly cited.

The main aims of this study were to determine the expression of human epididymis protein 4 (HE4) in endometrial cancer and to explore the relationships between HE4 expression, clinicopathological parameters, and prognosis. Immunohistochemistry was used to detect HE4 expression in 102 cases of endometrial cancer, 30 cases of endometrial atypical hyperplasia, and 20 cases of normal endometrium. The positive expression rate of HE4 in endometrial carcinoma was 84.62%, significantly higher than 66.67% in atypical hyperplasia ($P < 0.05$) and 15.00% in normal endometrium ($P < 0.01$). With the exception of stage II, HE4 expression in endometrial cancer showed an increasing tendency with increased clinical stage ($P < 0.05$). The positive expression rate of HE4 increased with a decrease in the degree of differentiation. A statistically significant difference was observed between the highly differentiated group and the poorly differentiated group ($P < 0.05$). Mortality in endometrial cancer patients with high HE4 expression was significantly higher than that in patients with low HE4 expression ($P < 0.05$). Endometrial cancer patients with high HE4 expression have a poor prognosis.

1. Introduction

Endometrial cancer is a malignant cancer with endometrial epithelial origin, accounting for 20% to 30% of malignant tumors in the female reproductive system. In recent years, due to increased obesity, hypertension, diabetes, and prolonged life expectancy, the incidence and mortality of endometrial cancer have risen, with a tendency for onset at a younger age [1]. The development of endometrial cancer is a multifactorial and multistep process. With an early manifestation of vaginal bleeding after menopause, approximately 70% of patients are diagnosed by fractional curettage at an early stage. However, the remaining 30% of patients with high risk factors are diagnosed with endometrial cancer at an advanced stage [2]. Thus, increasing the rate of early diagnosis is not only an important way of improving prognosis but also the key to increasing overall survival in patients with endometrial cancer. Up to now, no serum tumor markers with high sensitivity and specificity have been identified. Human epididymis protein 4 (HE4) is also known as whey

acidic protein (WFDC2). In 1999, Schummer et al. [3] first observed HE4 overexpression in ovarian cancer tissue. In 2003, HE4 was approved by the FDA as a serum tumor marker for ovarian cancer and attracted great attention [4]. The detection of HE4 alone or combined with CA125 can improve the diagnostic sensitivity and specificity of epithelial ovarian cancer [5, 6]. Recent studies have shown that HE4 is highly expressed in ovarian cancer tissue, as well as in other malignant tumors including lung adenocarcinoma, stomach cancer, and pancreatic cancer [7, 8]. In 2011, Yang et al. [9] performed an immunohistochemical assay and enzyme-linked immunosorbent assay to determine HE4 expression in tissue and peripheral blood from 31 cases of endometrial cancer for the first time, and the results indicated that the positive expression rate of HE4 and serum level of HE4 in the malignant group were significantly higher than those in the normal endometrium group (20 cases) and the endometrial hyperplasia group (19 cases), and the difference was statistically significant.

Our previous studies showed that high expression of HE4 was observed in ovarian cancer [10] and the positive expression rate in fallopian tube cancer was significantly higher than that in normal fallopian tube tissue [to be published]. The uterus, fallopian tubes, and ovaries originate from the urogenital ridge, and the former two originate from the paramesonephric duct; thus they possess similar embryogenic properties. Therefore, based on the above-mentioned theory, this study detected the expression of HE4 in endometrial cancer, endometrial atypical hyperplasia, and normal endometrium tissue samples with an adequate sample size and explored the relationship between HE4 expression and histological type, stage, differentiation, and prognosis of endometrial cancer, in order to provide a theoretical basis for an in-depth mechanism study of endometrial cancer development.

2. Materials and Methods

2.1. Patients. The paraffin-embedded samples examined in this study were collected during surgery from 173 cases treated in the Department of Obstetrics and Gynecology, Shengjing Hospital of China Medical University from 2004 to 2013. The pathological diagnosis of all tissue sections was determined by experts from the Department of Pathology, Shengjing Hospital of China Medical University. Of these 173 cases, there were 102 cases of endometrial cancer, 30 patients with atypical endometrial hyperplasia (10 cases each in the severe, moderate, and mild subgroups), and 20 patients with normal endometrium (10 cases each in the secretory and proliferative phase, resp.). Normal endometrium was donated by females with no fertility requirements, who underwent hysterectomy or removal of the uterus plus double annex due to cervical lesions. Enrollment criteria specifically excluded patients with uterine fibroids, ovarian cysts, and other uterine or ovarian diseases. Endometrial cancer patients were aged between 31 and 79 years old, mean 58.09 years; the patients with atypical endometrial hyperplasia were aged between 30 and 66 years old, mean 44.67 years; the patients with normal endometrium were aged between 34 and 53 years old, mean 44.50 years. The difference in age between the groups was not statistically significant ($P > 0.05$). In the endometrial cancer group, the pathological types consisted of 49 cases of endometrial adenocarcinoma, 22 cases of papillary serous adenocarcinoma, 21 cases of clear cell carcinoma, and 10 cases with other pathological types (including mucinous carcinoma, squamous cell carcinoma, undifferentiated cancer, and small cell carcinoma). With regard to the histological grade, there were 23 cases of highly differentiated cancer, 21 cases of moderately differentiated cancer, and 51 cases of poorly differentiated cancer. According to the staging of the International Federation of Gynecology and Obstetrics (FIGO) in 2009, there were 61 cases at stage I (38 cases at stage Ia and 23 cases at stage Ib), 7 at stage II, 28 at stage III, and 6 at stage IV. There were 27 patients with lymph node metastasis and 59 without lymph node metastasis. All patients had primary endometrial cancer, with complete clinical and pathological data and received no preoperative chemotherapy or hormone therapy.

2.2. Immunohistochemistry. Histologic sections of each group of fallopian tube tissues were 5 μm . The pattern of expression of HE4 in endometrial carcinoma tissues was analyzed via immunohistochemical streptavidin-peroxidase staining. Positive and negative immunohistochemistry controls were used. Ovarian carcinoma tissue served as a positive control. The negative control was incubated with phosphate-buffered saline instead of primary antibody. The working concentrations of primary antibodies against HE4 were 1:400 (rabbit polyclonal anti-HE4 antibody; Abcam, Cambridge, UK). The empirical procedure was performed based on the manufacturer's instructions.

2.3. Assessment Criteria. Immunohistochemical staining results, brown-stained granules on the cell membrane and cytoplasm, were regarded as positive. Based on the strength of color, uncolored, light yellow, yellowish brown, and brown were scored as 0, 1, 2, and 3, respectively. The percentage of stained cells in the field of view was calculated as follows: five consecutive high-powered fields in each section were observed under a 400x optical microscope, and then the scores were averaged. The proportion of positive cells <5% was recorded as 0, 5%–25% as 1, 21%–50% as 2, 51%–75% as 3, and >75% as 4. The final score was equal to the multiplication of the two scores: 0–2 as negative (–), 3–4 as weakly positive (+), and 5–12 as strongly positive (2+/3+) expression. For error control, the pathological section was evaluated by two observers separately; if any disagreement occurred, the result was judged by the third pathologist.

2.4. Statistical Analysis. Using the SPSS17.0 software system, χ^2 test and Fisher exact test were conducted. The *t*-test was used for comparisons between two groups and analysis of variance for multiple group comparisons. Kaplan-Meier analysis and the log-rank test were applied for the survival curve. $P < 0.05$ was considered statistically significant.

3. Results

3.1. HE4 Expression in Endometrial Tissue. HE4 was mainly expressed in the cell membrane, and the cytoplasm also showed slight expression. The positive expression rate of HE4 was 84.62% in the endometrial cancer group, significantly higher than 66.67% in the endometrial atypical hyperplasia group, and 15.00% in the normal endometrium group ($P = 0.014, 0.001$). The positive expression rate of HE4 was 40.00% in the mild atypical hyperplasia group, 80.00% in the moderate atypical hyperplasia group, and 80.00% in the severe atypical hyperplasia group, respectively. The positive rate of HE4 expression in the moderate and severe atypical hyperplasia groups was significantly higher than that in the mild atypical hyperplasia group ($P = 0.045$) and normal endometrium group ($P < 0.001$). The positive expression rate of HE4 in the proliferative phase was higher than that in the secretory phase (20% versus 10%), but there was no significant difference between them ($P > 0.05$).

HE4 expression intensity increased with increased degree of malignancy. The strongly positive (2+/3+) expression rate in endometrial cancer was 55.98%, significantly higher

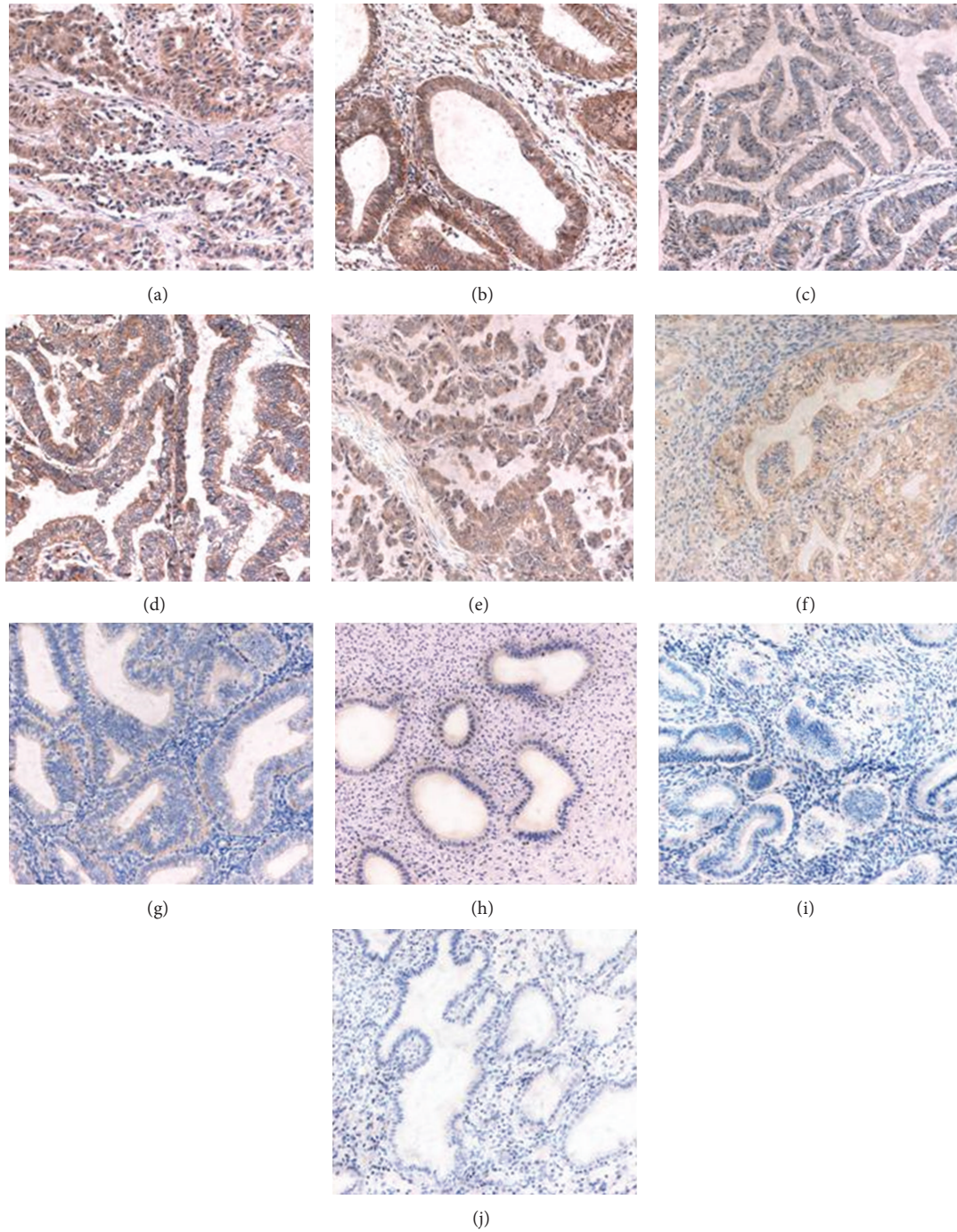


FIGURE 1: Immunohistochemical micrographs of HE4 in different endometrial tissues (200x). The expression level of HE4 was higher in endometrial cancer than in endometrial atypical hyperplasia and normal endometrium. (a) Poorly; (b) moderately; and (c) highly differentiated adenocarcinoma. (d) Clear cell carcinoma and (E) uterine papillary serous carcinoma. (f) Severe; (g) moderate; and (h) mild atypical hyperplasia. (i) Secretory phase and (j) proliferative phase normal endometrium.

than that in the atypical hyperplasia group (20.00%) ($P = 0.003$), and in the normal endometrium group (0.00%) ($P = 0.033$). The strongly positive expression rate of HE4 was 0.00% in the mild atypical hyperplasia group, 20.00% in the moderate atypical hyperplasia group, and 40.00% in the severe atypical hyperplasia group, respectively, which showed an increasing tendency with aggregation of the disease.

The strongly positive expression rate of HE4 in the severe hyperplasia group was significantly higher than that in the mild hyperplasia group ($P = 0.025, <0.05$). The strongly positive expression rate of HE4 in the moderate and severe atypical hyperplasia groups was significantly higher than that in the normal endometrium group ($P = 0.031, 0.002$, all $P < 0.05$) (Figure 1, Table 1).

TABLE 1: HE4 expression in endometrial tissue.

Groups	Cases	-	+	++	+++	Positive cases	Positive rate (%)	Strong positive cases	Strong positive rate (%)
Endometrial cancer group	102	14	36	32	20	88	84.62*	52	55.98 ^ϕ
Endometrial atypical hyperplasia group	30	10	14	6	0	20	66.67	6	20.00
Severe	10	2	4	4	0	8	80.00**	4	40.00**
Moderate	10	2	6	2	0	8	80.00**	2	20.00 ^δ
Mild	10	6	4	0	0	4	40.00	0	0.00
Normal endometrium group	20	17	3	0	0	3	15.00	0	0.00
Secretory phase	10	8	2	0	0	2	20.00	0	0.00
Proliferative phase	10	9	1	0	0	1	10.00	0	0.00

Note: * compared with the atypical hyperplasia group and normal group, $P < 0.01$; ** compared with the mild hyperplasia group, $P < 0.05$; compared with the normal group, $P < 0.01$; ^ϕ compared with the atypical hyperplasia group, $P < 0.05$; compared with the normal group $P < 0.01$; ^δ compared with the normal group, $P < 0.05$.

3.2. Relationship between HE4 Expression and Clinicopathological Parameters of Endometrial Cancer. HE4 expression in endometrial cancer was 76.32% at stage Ia, 91.30% at stage Ib, 71.43% at stage II, 96.43% at stage III, and 100.00% at stage IV, respectively, which showed an increasing tendency with increased clinical stage. Interestingly, the positive expression rate of HE4 at stage Ia was similar to that at stage II; the positive expression rate of HE4 at stage Ib was close to that at stage III or IV, indicating that the expression of HE4 was closely related to the invasion depth of the affected myometrium. Statistical analysis showed that there was a statistically significant difference in HE4 expression between stages III and Ia ($P_{Ia:III} = 0.024$), stages III and II ($P_{II:III} = 0.035$), stages IV and I ($P_{I:IV} = 0.009$), and stages III-IV and I-II ($P_{(I+II):(III+IV)} = 0.007$). The strongly positive expression rate of HE4 showed a similar trend. The strongly positive expression rate of HE4 in endometrial cancer was 31.57% at stage Ia, 56.52% at stage Ib, 28.57% at stage II, 71.42% at stage III, and 83.33% at stage IV, respectively, which showed an increasing tendency with increased clinical stage ($P_{Ia:III} = 0.001$, $P_{Ia:IV} = 0.016$, $P_{I:III} = 0.008$, $P_{I:IV} = 0.047$, $P_{II:III} = 0.035$, $P_{II:IV} = 0.048$, and $P_{(I+II):(III+IV)} = 0.001$).

HE4 expression in endometrial cancer was 72.72% in the highly differentiated group, 85.71% in the moderately differentiated group, and 92.31% in the poorly differentiated group, respectively. With a decrease in the degree of differentiation, the HE4 positive expression rate increased, and HE4 expression in the poorly differentiated group was significantly higher than that in the highly differentiated group ($P_{high:low} = 0.024$, $P_{high:middle} = 0.348$, and $P_{middle:low} = 0.254$). HE4 expression intensity was also closely related to the degree of differentiation. The strongly positive rate of HE4 expression was 34.62% in the highly differentiated group, 46.43% in the moderately differentiated group, and 57.69% in the poorly differentiated group, respectively, and showed no statistically significant differences between the groups ($P_{high:low} = 0.186$, $P_{high:middle} = 0.696$, and $P_{middle:low} = 0.335$).

HE4 positive expression rate in patients with lymph node metastasis was 89.66%, close to 84.93% in patients without lymph node metastasis ($P = 0.532$), whereas

the strongly positive expression rate of HE4 in patients with lymph node metastasis (73.33%) was significantly higher than that in patients without lymph node metastasis (41.40%) ($P = 0.002$). HE4 positive expression rate was 82.14% in type I endometrial cancer and 87.84% in type II ($P = 0.456$); HE4 positive expression rates in endometrial adenocarcinoma, serous papillary carcinoma, clear cell carcinoma of the uterus, and other special pathological types were 91.84%, 71.43%, and 86.36%, respectively, and showed no significant statistical difference between the groups ($P > 0.05$) (Figure 1, Table 2).

3.3. Prognosis Analysis. Up to May 2014, all patients were followed up for 9–116 months. Among 102 patients with endometrial cancer, 18 died due to tumor recurrence and metastasis. Kaplan-Meier survival analysis showed that endometrial cancer patients with strongly positive expression of HE4 had significantly higher mortality than those without strongly positive expression of HE4 ($P = 0.027$, Figure 2(a)); with an increase in endometrial cancer stage, mortality also showed a rising trend, and the mortality of endometrial cancer at FIGO stages III-IV was significantly higher than that in patients at FIGO stages I-II; the difference was statistically significant ($P = 0.010$, Figure 2(b)). Mortality in the poorly differentiated group and in patients with lymph node metastasis was also higher than that in the moderately or highly differentiated group and in patients without lymph node metastasis ($P = 0.160$, 0.081), but the difference was not statistically significant; therefore further follow-up is necessary (Figures 2(c) and 2(d)).

4. Discussion

In recent years, HE4 has been used as a tumor marker, and a number of serological tests have proved its early diagnostic value in epithelial ovarian tumors [3–5, 11]. The “2012 NCCN guidelines for the diagnosis and treatment of ovarian cancer” clearly indicate its clinical value as a tumor marker for epithelial ovarian cancer.

As the uterus and ovaries share the same embryonic origin, some pathological subtypes of ovarian cancer

TABLE 2: HE4 expression in endometrial cancer with different clinical parameters.

Features		Cases	Positive cases	Positive rate (%)	Strong positive cases	Strong positive rate (%)	*P	**P
EC type	I	28	23	82.14	15	53.57	0.456	0.747
	II	74	65	87.84	37	50.00		
Pathological type	Endometrial adenocarcinoma	49	45	91.84	26	53.06	<i>P</i> > 0.05	<i>P</i> > 0.05
	Uterine papillary serous carcinoma	21	15	71.43	8	38.10		
	Clear cell carcinoma	22	19	86.36	11	50.00		
	Mucous carcinoma	4	4	100.00	3	75.00		
	Undifferentiated carcinoma	3	2	66.67	2	66.67		
	Squamous cell carcinoma	2	2	100.00	1	50.00		
	Small cell carcinoma	1	1	100.00	1	100.00		
FIGO stage	Ia	38	29	76.32	12	31.57	<i>P</i> _{Ia:III} = 0.024 <i>P</i> _{I:IV} = 0.009 <i>P</i> _{II:III} = 0.035 <i>P</i> _{(I+II):(III+IV)} = 0.007 Others <i>P</i> > 0.05	<i>P</i> _{Ia:III} = 0.001 <i>P</i> _{Ia:IV} = 0.016 <i>P</i> _{I:III} = 0.008 <i>P</i> _{I:IV} = 0.047 <i>P</i> _{II:III} = 0.035 <i>P</i> _{II:IV} = 0.048 <i>P</i> _{(I+II):(III+IV)} = 0.001 Others <i>P</i> > 0.05
	Ib	23	21	91.30	13	56.52		
	II	7	5	71.43	2	28.57		
	III	28	27	96.43	20	71.42		
	IV	6	6	100	5	83.33		
Differentiation level	High	22	16	72.72	9	34.62	<i>P</i> _{high:low} = 0.024 Others <i>P</i> > 0.05	<i>P</i> > 0.05
	Middle	28	24	85.71	13	46.43		
	Low	52	48	92.31	30	57.69		
Lymphatic metastasis	No	59	48	81.36	22	59.46	<i>P</i> = 0.532	<i>P</i> = 0.001
	Yes	27	26	96.30	21	77.78		
	No lymph node cleaning	16	14	87.50	9	56.25		

Note: * comparison of HE4 positive rate in each group; ** comparison of strongly positive HE4 expression rate in each group.

are endometrial adenocarcinomas, and both are malignant female reproductive system tumors. Thus, the determination of serum HE4 level in endometrial cancer patients has aroused wide attention. Moore et al. [12] determined multiple tumor markers in 156 healthy subjects and in 171 patients with endometrial cancer and found that HE4 expression at each stage of endometrial cancer was increased; the sensitivity of serum HE4 was higher than that of CA125. Angioli et al. [13] regarded serum HE4 concentration > 70 pmol/L as a quantitative indicator of endometrial cancer as this value showed the best sensitivity, specificity, and positive predictive value. Zanotti et al. [14] detected serum HE4 levels in 193 patients with endometrial carcinoma and in 125 healthy controls, and the results showed that a preoperative increase in HE4 is an independent prognostic factor for decreased overall survival, disease-free survival, and tumor progression-free survival in patients with endometrial cancer. In 2011, based on preliminary studies, Moore et al. [15]

proposed the use of serum HE4 level to predict invasion depth of the myometrium to assess the necessity of preoperative lymph node dissection as a preoperative index. In 2011, Yang et al. [9] used an immunohistochemical method to detect the expression of HE4 in 31 cases of endometrial cancer, 19 cases of endometrial hyperplasia, and 20 cases of normal endometrial tissue, and the results showed that the positive expression rate of HE4 in the malignant group was significantly higher than that in the normal group and hyperplasia group and a statistically significant difference was observed between the groups. However, due to the small number of specimens and few subtypes in the cases (only four cases of special pathological types), the specimens did not explain the relationship between HE4 expression and lymph node metastasis. In addition, this study lacked a group with endometrial cancer FIGO IV stage and, in particular, lacked an atypical endometrial hyperplasia group, an important transitional pathological type.

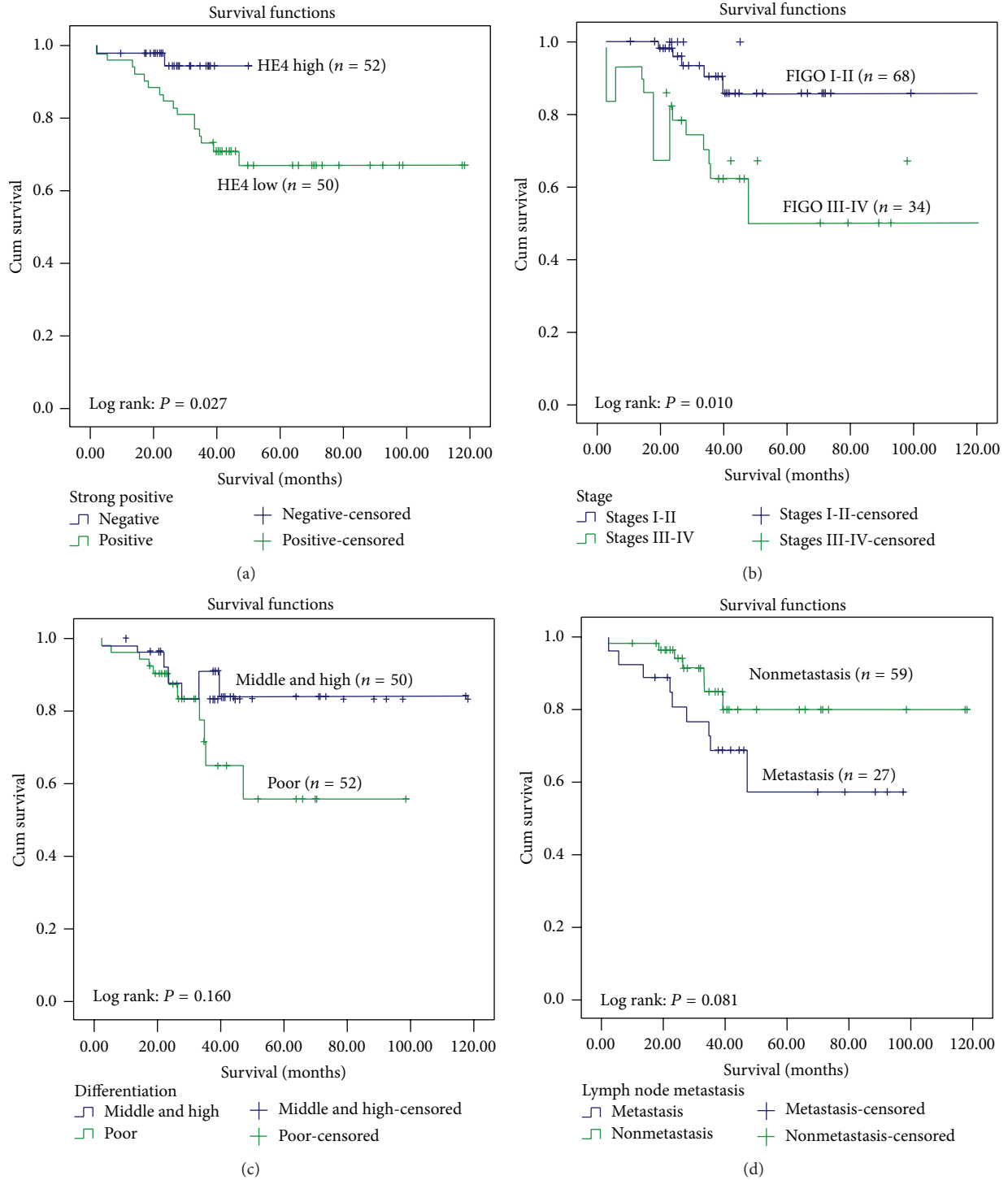


FIGURE 2: Comparison of survival rates. Curves of deaths stratified by (a) HE4 strong positive; (b) stage; (c) differentiation; and (d) lymphatic metastasis.

In the present study, HE4 expression was detected on a larger scale: in 102 cases of endometrial cancer, 30 cases of atypical hyperplasia, and in 20 cases with normal endometrial tissue. The results showed that the positive expression rate of HE4 in endometrial cancer was significantly higher than that in atypical hyperplasia and normal endometrium

($P < 0.05$). The positive expression rate in atypical hyperplasia was significantly higher than that in the normal group, and the strongly positive expression rate in the severe hyperplasia group was significantly higher than that in the mild or moderate hyperplasia group. The HE4 expression level in normal, precancerous, and malignant tissues gradually

increased as follows: normal tissues < precancerous lesions < malignant tissues, suggesting that HE4 may be involved in the development and progression of tumors. Li et al. [16] established endometrial cancer cell lines with HE4 overexpression and demonstrated that overexpression of HE4 enhanced the malignant behavior of cancer cells including proliferation, invasion, and colony formation. Real-time PCR showed that the mRNA and protein expression of HE4 in endometrial cancer tissue increased and immunofluorescence indicated that most of cells remained in the S phase of the cell cycle. These findings explain our results at the cellular and protein levels; however, the exact mechanism mediating the above-mentioned behavior requires further study.

Most endometrioid adenocarcinomas are estrogen-dependent (Type I), while other special histological types such as serous papillary carcinoma and clear cell carcinoma are nonestrogen-dependent (Type II). Our results show that HE4 is not correlated with pathological subtypes and estrogen-sensitivity; thus, unlike estrogen, to some extent, HE4 does not affect those at high risk of endometrial cancer, patients with obesity or diabetes and breast cancer patients on long-term administration of estrogen; that is [17], HE4 expression rate does not affect the pathological types of endometrial cancer and estrogen dependency. Therefore, we speculated that preoperative serum HE4 level cannot predict the histological subtypes of endometrial cancer, which is consistent with the findings of Bignotti et al. [18]. According to FIGO staging of endometrial cancer in 2009, cervical gland involvement is classified as stage I, rather than IIa. Stage II is defined as involvement of the cervical stroma, but without ectopic invasion. Cancerous tissues spread downwards to the stroma outside the cervical glands; however, because cervical tissue itself is much thinner than the myometrium, malignant tissue infiltration depth at stage II endometrial cancer may be less than that at stage I. Theoretically, the expression level of HE4 may be lower than that at stage I, which is in accordance with our study: with the exception of stage II, the positive expression and strongly positive expression rate of HE4 increased with increasing stage. The positive expression rate of HE4 in stage I endometrial cancer was higher than that at stage II, the strongly positive expression rate of HE4 at stages III and IV was significantly higher than that at stages I and II, the positive expression rate of HE4 at stages III and IV was higher than that at stage Ia, and the positive expression and strongly positive expression rate of HE4 in advanced endometrial cancer were significantly higher than that at earlier stages. It was noted that when stage FIGO Ia and Ib were compared, although no statistically significant difference was observed between the two, the HE4 expression rate and strongly positive expression rate differed greatly (91.30% versus 76.32%, 56.52% versus 31.57%, resp.), suggesting that the expression level of HE4 is not only related to the degree of ectopic metastasis but also associated with myometrial invasion depth. The larger the area and greater the depth of invasion, the more malignant cells are present and the higher the HE4 expression in corresponding tissues. Thus, as a secreted protein, more HE4 enters the blood, thereby increasing the peripheral blood concentration of HE4, which is consistent with findings in the literature

[15, 16, 18]. However, a larger sample size in further studies is required to confirm these findings. As the degree of endometrial cancer differentiation decreased, the HE4 level increased, and the HE4 positive expression rate in the poorly differentiated group was significantly higher than that in the highly differentiated group, which demonstrated that HE4 expression in endometrial cancer is related to the degree of differentiation of the tumor. Prognostic analysis showed that mortality in patients with advanced endometrial cancer was significantly higher than that in patients at earlier stages and mortality in patients with high expression of HE4 was significantly higher than that in those with low expression, suggesting that HE4 may be involved in the recurrence, metastasis, and other adverse events of endometrial cancer. However, its mechanism needs to be clarified.

In recent studies, using overexpression and knockout of HE4 related genes, the malignant biological behavior such as cell adhesion, invasion, and proliferation was enhanced or inhibited in ovarian cancer cell lines. This was achieved through the EGFR-MAPK signal transduction pathway [19]. Following HE4 gene knockout, the phosphorylation levels of EGFR and Erk1/2 in ovarian cancer were affected; when HE4 was added to the cell culture, the phosphorylation levels of EGFR and Erk1/2 were restored. However, the mechanism involved is not yet clear. Lewis y antigen (a double-fucosylated oligosaccharide, located at the ends of many glycoproteins and glycolipids as a tumor-associated carbohydrate antigen) is part of the EGFR structure. Increased expression of Lewis y antigen activates EGFR and HER2/neu receptor tyrosine kinases, which further activate the PI3K/Akt and Raf/MEK/MAPK signal transduction pathways downstream of EGFR, resulting in accelerated transcription of HER2/neu genes in the nucleus and stimulation of DNA synthesis and ultimately promotes the cells to skip G1 phase into S phase, promoting cell proliferation and other kinds of malignant behavior [20]. Our previous studies confirmed the existence of the Lewis y structure on HE4, and ovarian cancer experiments showed that glycosylated HE4 had a stronger impact on cytobiology than nonglycosylated HE4 [to be published]. The modification of HE4 by Lewis y antigen enhanced tumor cell invasion, proliferation, adhesion, and other kinds of malignant behavior [10, 11, 16]. However, the mechanisms of HE4 mediating the occurrence and development of endometrial cancer require further study.

5. Conclusions

In summary, we conducted a large scale study and proved that the positive expression of HE4 in patients with endometrial cancer was significantly higher than that in patients with atypical hyperplasia and in those with normal endometrial tissue, which provides a preliminary theoretical reference for basic research on the role of HE4 in the development of endometrial cancer. However, whether HE4 mediates the biological behavior of endometrial cancer via the corresponding signal transduction pathways, as seen in ovarian cancer, thereby affecting the occurrence and development of endometrial cancer, requires further research.

Conflict of Interests

The authors declare no conflict of interests.

Authors' Contribution

Xiao Li and Bei Lin had the idea for this research, took responsibility for the design of this work, and wrote the paper. Mingzi Tan, Yiping Gao, and Huiyu Zhuang have made substantial contributions in acquisition of data. Liancheng Zhu and Juanjuan Liu performed all statistical analyses. Jian Gao, Zhenhua Hu, and Huimin Wang participated in its design and coordination and helped draft the paper. All authors have given final approval of the version to be published.

Acknowledgments

This work was supported by the National Natural Science Foundation of China (nos. 81172491, 81101527, and 81472437); Ph.D. Programs Foundation of Ministry of Education of China (nos. 20112104110016, 20112104120019); Shengjing Free Researcher Project (no. 201303).

References

- [1] D. J. Brennan, A. Hackethal, A. M. Metcalf et al., "Serum HE4 as a prognostic marker in endometrial cancer—a population based study," *Gynecologic Oncology*, vol. 132, no. 1, pp. 159–165, 2014.
- [2] J. Li, S. Dowdy, T. Tipton et al., "HE4 as a biomarker for ovarian and endometrial cancer management," *Expert Review of Molecular Diagnostics*, vol. 9, no. 6, pp. 555–566, 2009.
- [3] M. Schummer, W. V. Ng, R. E. Bumgarner et al., "Comparative hybridization of an array of 21,500 ovarian cDNAs for the discovery of genes overexpressed in ovarian carcinomas," *Gene*, vol. 238, no. 2, pp. 375–385, 1999.
- [4] I. Heliström, J. Raycraft, M. Hayden-Ledbetter et al., "The HE4 (WFDC2) protein is a biomarker for ovarian carcinoma," *Cancer Research*, vol. 63, no. 13, pp. 3695–3700, 2003.
- [5] S. K. Saarelainen, N. Peltonen, T. Lehtimäki, A. Perheentupa, M. H. Vuento, and J. U. Mäenpää, "Predictive value of serum human epididymis protein 4 and cancer antigen 125 concentrations in endometrial carcinoma," *American Journal of Obstetrics and Gynecology*, vol. 209, no. 2, pp. 142.e1–142.e6, 2013.
- [6] T. van Gorp, I. Cadron, E. Despierre et al., "HE4 and CA125 as a diagnostic test in ovarian cancer: prospective validation of the Risk of Ovarian Malignancy Algorithm," *British Journal of Cancer*, vol. 104, no. 5, pp. 863–870, 2011.
- [7] K. Tokuishi, S.-I. Yamashita, K. Ohbo, and K. Kawahara, "Splice variant HE4-V3 expression is associated with favorable prognosis in pulmonary adenocarcinoma," *Tumor Biology*, vol. 33, no. 1, pp. 103–109, 2012.
- [8] R. L. O'Neal, K. T. Nam, B. J. Lafleur et al., "Human epididymis protein 4 is up-regulated in gastric and pancreatic adenocarcinomas," *Human Pathology*, vol. 44, no. 5, pp. 734–742, 2013.
- [9] C. H. Yang, Y. H. Xu, and X. Y. Zhang, "Expression and significance of human epididymis gene product 4 in tissue and serum of patients with endometrial cancer," *Chinese Journal of Clinical Oncology*, vol. 38, no. 9, pp. 516–519, 2011.
- [10] H. Zhuang, J. Gao, Z. Hu, J. Liu, D. Liu, and B. Lin, "Co-expression of Lewis y antigen with human epididymis protein 4 in ovarian epithelial carcinoma," *PLoS ONE*, vol. 8, no. 7, Article ID e68994, 2013.
- [11] R. Angioli, F. Plotti, S. Capriglione et al., "Can the preoperative HE4 level predict optimal cytoreduction in patients with advanced ovarian carcinoma?" *Gynecologic Oncology*, vol. 128, no. 3, pp. 579–583, 2013.
- [12] R. G. Moore, A. K. Brown, M. C. Miller et al., "The use of multiple novel tumor biomarkers for the detection of ovarian carcinoma in patients with a pelvic mass," *Gynecologic Oncology*, vol. 108, no. 2, pp. 402–408, 2008.
- [13] R. Angioli, F. Plotti, S. Capriglione et al., "The role of novel biomarker HE4 in endometrial cancer: a case control prospective study," *Tumor Biology*, vol. 34, no. 1, pp. 571–576, 2013.
- [14] L. Zanotti, E. Bignotti, S. Calza et al., "Human epididymis protein 4 as a serum marker for diagnosis of endometrial carcinoma and prediction of clinical outcome," *Clinical Chemistry and Laboratory Medicine*, vol. 50, no. 12, pp. 2189–2198, 2012.
- [15] R. G. Moore, C. M. Miller, A. K. Brown, K. Robison, M. Steinhoff, and G. Lambert-Messerlian, "Utility of tumor marker HE4 to predict depth of myometrial invasion in endometrioid adenocarcinoma of the uterus," *International Journal of Gynecological Cancer*, vol. 21, no. 7, pp. 1185–1190, 2011.
- [16] J. Li, H. Chen, A. Mariani et al., "HE4 (WFDC2) promotes tumor growth in endometrial cancer cell lines," *International Journal of Molecular Sciences*, vol. 14, no. 3, pp. 6026–6043, 2013.
- [17] J. Watanabe, Y. Kamata, N. Seo, I. Okayasu, and H. Kuramoto, "Stimulatory effect of estrogen on the growth of endometrial cancer cells is regulated by cell-cycle regulators," *The Journal of Steroid Biochemistry and Molecular Biology*, vol. 107, no. 3–5, pp. 163–171, 2007.
- [18] E. Bignotti, M. Ragnoli, L. Zanotti et al., "Diagnostic and prognostic impact of serum HE4 detection in endometrial carcinoma patients," *British Journal of Cancer*, vol. 104, no. 9, pp. 1418–1425, 2011.
- [19] R. Lu, X. Sun, R. Xiao, L. Zhou, X. Gao, and L. Guo, "Human epididymis protein 4 (HE4) plays a key role in ovarian cancer cell adhesion and motility," *Biochemical and Biophysical Research Communications*, vol. 419, no. 2, pp. 274–280, 2012.
- [20] J.-J. Liu, B. Lin, Y.-Y. Hao et al., "Lewis(y) antigen stimulates the growth of ovarian cancer cells via regulation of the epidermal growth factor receptor pathway," *Oncology Reports*, vol. 23, no. 3, pp. 833–841, 2010.

Research Article

Neuroprotective Effect of Simvastatin via Inducing the Autophagy on Spinal Cord Injury in the Rat Model

Kai Gao,¹ Guannan Wang,² Yansong Wang,¹ Donghe Han,³ Jing Bi,³ Yajiang Yuan,¹ Tianchen Yao,¹ Zhanghui Wan,¹ Haihong Li,¹ and Xifan Mei¹

¹Department of Orthopedics, First Affiliated Hospital of Liaoning Medical University, Jinzhou 121000, China

²College of Pharmacy, Liaoning Medical University, Jinzhou 121000, China

³Department of Neurobiology and Key Laboratory of Neurodegenerative Diseases of Liaoning Province, Liaoning Medical University, Jinzhou 121000, China

Correspondence should be addressed to Xifan Mei; meixifan1971@163.com

Received 3 March 2015; Accepted 31 March 2015

Academic Editor: Jiangbo Yu

Copyright © 2015 Kai Gao et al. This is an open access article distributed under the Creative Commons Attribution License, which permits unrestricted use, distribution, and reproduction in any medium, provided the original work is properly cited.

Simvastatin, an inhibitor of 3-hydroxy-3-methylglutaryl-coenzyme A reductase, is invariably used to treat cardiovascular diseases. Simvastatin has been recently demonstrated to have a neuroprotective effect in nervous system diseases. The present study aimed to further verify the neuroprotection and molecular mechanism of simvastatin on rats after spinal cord injury (SCI). The expression of Beclin-1 and LC3-B was evidently enhanced at postoperation days 3 and 5, respectively. However, the reduction of the mTOR protein and ribosomal protein S6 kinase p70 subtype (p70S6K) phosphorylation level occurred at the same time after SCI. Simvastatin significantly increased the expression of brain-derived neurotrophic factor (BDNF) and glial cell line-derived neurotrophic factor (GDNF). Meanwhile, immunofluorescence results indicated that the expression of chondroitin sulfate proteoglycan (CSPG) and caspase-3 protein was obviously reduced by simvastatin. Furthermore, Nissl staining and Basso, Beattie, and Bresnahan (BBB) scores showed that the quantity and function of motor neurons were visibly preserved by simvastatin after SCI. The findings of this study showed that simvastatin induced autophagy by inhibiting the mTOR signaling pathway and contributed to neuroprotection after SCI.

1. Introduction

Spinal cord injury (SCI) is a medical problem worldwide [1]. Secondary injury significantly affects SCI and is induced by several factors, such as inflammation, oxidative stress, apoptosis, and autophagy [2, 3]. Autophagy is an important process to maintain cellular homeostasis and protects against a variety of diseases in the central nervous system [4, 5].

Simvastatin is widely used as the first-line therapeutic drug to reduce cholesterol and prevent coronary heart diseases and atherosclerosis. In recent years, an increasing number of studies have investigated the pleiotropic effects of statins, such as anti-inflammation, immunoregulation, and the induction in autophagy [6, 7]. Stüve et al. [8, 9] demonstrated that simvastatin has an effective therapeutic effect on multiple sclerosis, Alzheimer's disease, ischemic stroke, and rheumatoid arthritis. However, clinical observation showed

that these effects cannot be attributed to the beneficial aspects of cholesterol-lowering activity [10].

Recent studies have shown that autophagy is activated by simvastatin through inhibiting the mTOR signaling pathway, which alleviates myocardial cell damage, promotes regeneration of myocardial cells, and prevents the occurrence of atherosclerosis [11]. Simultaneously, some reports also indicated that simvastatin promotes functional recovery after SCI by lowering the activity of astrocytes and the expression of inflammatory factors [12–14]. However, the molecular mechanism of the neuroprotection after SCI has not been elucidated.

In the present study, the effect of simvastatin on autophagy after SCI is initially proposed. We attempted to provide evidence that further validates the neuroprotection of simvastatin and investigate the molecular mechanism of the neuroprotection after SCI.

2. Materials and Methods

2.1. Animal Care and Groups. Eighty-one adult male Sprague-Dawley rats (240–260 g) were purchased from the Laboratory Animal Center of the Liaoning Medical University. The rats were raised in the SPF laboratory animal center at constant environment of $23 \pm 0.5^\circ\text{C}$, with an alternating 12 h light-dark cycle. All experimental procedures were carried out in accordance with the Guidelines for the Care and Use of Laboratory Animals published by the US National Institutes of Health. All efforts were made to minimize the number of animals used and their suffering.

The rats were randomly divided into three groups: (1) simvastatin, (2) vehicle, and (3) sham. Simvastatin (10 mg/kg) and vehicle were administered via intraperitoneal injection at 1 h after SCI and then once daily for 2 days [6, 12].

2.2. SCI. The rats were operated on as previously described [15]. In brief, the rats were anesthetized with intraperitoneal injection of chloral hydrate (0.33 mL/kg) and the spinal cord was aseptically exposed after laminectomy at T9–10. Subsequently, a 2 mm diameter impounder (weight: 10 g) was dropped from a height of 25 mm and struck at the surface of T9–10 spinal cord, which led to spinal cord congestion. The sham-operated animals underwent laminectomy alone. After SCI, manual bladder expression was performed thrice daily until the bladder function of the rats was reestablished.

2.3. Simvastatin Treatment. Simvastatin (Catalog number 567020; Calbiochem, Germany) was dissolved in 100% ethanol and activated by 0.1 N NaOH after heating at 50°C for 2 h. pH was then adjusted to 7.2, and stock solution was maintained at 4°C prior to use [16, 17].

2.4. Locomotion Recovery Assessment. The Basso, Beattie, and Bresnahan (BBB) open-field locomotor rating scale was employed to evaluate the recovery condition of motor function after SCI [18]. In brief, three independent examiners were blinded to assess the BBB scores before operation and at 1, 3, 7, 14, 21, 28, and 35 d after SCI. The BBB scores ranged from 0 to 21 points. The minimum points (0) indicated complete paralysis, and the maximum points implied normal function. The average scores were calculated according to the progress in locomotion recovery after SCI.

2.5. Western Blot Analysis. At 3, 5, and 7 d after SCI, the rats were anesthetized, and the damaged spinal cord (2 mm cephalad and caudally around the injury epicenter) was removed. The tissues were dissolved in RIPA lysis buffer, and the final protein concentration ($2 \mu\text{g}/\mu\text{L}$) was quantified using the BCA kit. Protein samples ($40 \mu\text{g}$) were then emitted into different lanes. The proteins were separated by SDS-PAGE and transferred into PVDF membranes. Subsequently, the membranes were incubated at 4°C overnight with primary antibodies including anti-mTOR antibody (1:1000; Novus Biologicals, USA), anti-phospho-p70S6 antibody (1:500; Abcam, Cambridge, UK), anti-LC3 antibody (1:1000; Novus Biologicals, USA), anti-Beclin-1 antibody (1:1000; Abcam),

anti-brain-derived neurotrophic factor (BDNF) antibody (1:1000; Novus Biologicals, USA), anti-glia cell line-derived neurotrophic factor (GDNF) antibody (1:1000; Novus Biologicals, USA), and anti- β -actin antibody (1:1000; Abcam, Cambridge, UK). On the second day, the membranes were incubated at room temperature for 2 h with secondary antibodies (1:2000; Abcam, Cambridge, UK). The membranes were developed using ChemiDoc-It TS2 Imager (UVP, LLC, Upland, CA, USA), and relative optical density was performed using ImageJ2x software (National Institutes of Health, Bethesda, MD, USA).

2.6. Immunofluorescence Analysis. The rats were anesthetized and perfused with 0.9% saline and then with 4% paraformaldehyde at 1 week after SCI. The T8–T12 segments of the spinal cord were excised from the rats and steeped into 4% paraformaldehyde. The $5 \mu\text{m}$ crosswise sections (3 mm rostral to the epicenter) were cut using a cryostat microtome. The sections were dried at room temperature and were placed into 0.01 M citric acid (pH 6.0) for antigen retrieval. Next, the sections were blocked with blocking buffer (5% normal goat serum and 0.1% Triton X-100 in PBS) at 4°C for 1 h and incubated overnight with primary antibodies including anti-CSPG antibody (1:400; Sigma-Aldrich) and anti-caspase-3 antibody (1:100; Novus Biologicals, USA). The following day, the sections were incubated with FITC goat anti-rabbit/mouse IgG, and the nucleus was redyed with DAPI solution. All slides were observed under a fluorescence microscope (Leica, Heidelberg, Germany) after being mounted with Permount TM mounting medium (Sigma-Aldrich, St. Louis, MO, USA). The optical density of fluorescence was analyzed using ImageJ2x software.

2.7. Nissl Staining. The rats were perfused with 0.9% saline and 4% paraformaldehyde at 7 d after SCI. The $20 \mu\text{m}$ crosswise sections (3 mm rostral to the epicenter) were cut using a cryostat microtome. The sections were dried and then soaked directly into the mixed liquor (1:1 alcohol/chloroform) overnight. The sections were successively rehydrated with 100% alcohol, 95% alcohol, and distilled water. Subsequently, the sections were stained in 0.1% Cresyl violet (Sigma-Aldrich) solution. The sections were then differentiated in 95% ethyl alcohol, dehydrated in 100% alcohol, and rinsed in xylene. Finally, the sections were mounted and observed under a light microscope. The average quantity of neurons was calculated by randomly selecting five Nissl-stained sections at the same site from each rat.

2.8. Statistical Analysis. All data were expressed as mean \pm SD and analyzed using the Graph Prism Program, Version 5.0 (GraphPad Software, Inc., La Jolla, USA). Unpaired Student's *t*-test was used for the comparison among groups. The discrepancy of the multiple groups was tested using one-way ANOVA, and the BBB scores were analyzed with the Mann-Whitney *U* test. *p* values less than 0.05 were considered statistically significant, and the discrepancy was statistically significant if $p < 0.01$.

3. Results

3.1. Simvastatin Improves Motor Functional Recovery after SCI.

We assessed the locomotor performance of rats by using the BBB locomotor rating scale at 0, 1, 3, 7, 14, 21, 28, and 35 d. The curve graph shows the tendency to change based on the scores (Figure 1). We found that the locomotor function was drastically reduced in the first day after SCI and gradually recovered with time, whereas the resumptive levels were distinct between the simvastatin and vehicle groups. At 3 and 7 d, the recovery of motor function in the simvastatin group was similar to the vehicle group ($p > 0.05$). Nevertheless, at 14 d after SCI, the simvastatin-treated rats (BBB scores: 11.3 ± 2.1) showed a more significant recovery than the vehicle group (BBB scores: 7.5 ± 1.3 ; $p < 0.05$). Similarly, the significant tendency also increased at 21, 28, and 35 d (BBB: 21 d after operation: simvastatin group (12.8 ± 1.3) compared with the vehicle group (10.5 ± 1.3); 28 d after operation: simvastatin group (14.8 ± 2.2) compared with the vehicle group (11.3 ± 1.7); and 35 d after operation: simvastatin group (15.3 ± 1.7) compared with the vehicle group (11.5 ± 1.3); $p < 0.05$). The trend revealed that the motor function of the rats is increasingly restored, and recovery was faster after 14 d with simvastatin treatment.

3.2. Simvastatin Induces Autophagy by Inhibiting the mTOR Signaling Pathway after SCI. Western blot detected the expression of Beclin-1, LC3, mTOR, and p-p70S6K proteins for observing the alteration of autophagy in the three groups (Figure 2(a)). Upon formation of the autophagy membrane, conversion from the nonlipidated form (LC3-A) to the lipidation form (LC3-B) is considered to be an important symbol of autophagic activation. LC3-B is the form incorporated in autophagosomes and thus often used as a marker for autophagosomes [19–21]. At the same time, Beclin-1 protein is commonly used for autophagy detection, which is a unique autophagy-related protein [22]. The expression levels of Beclin-1 and LC3-B proteins significantly increased in the presence of simvastatin compared with the absence of simvastatin at 3 and 5 d (Figures 2(d) and 2(e)). However, the results were not statistically different at 7 d after SCI (Figures 2(d) and 2(e), $p > 0.05$ compared with the vehicle). In addition, to examine whether simvastatin suppressed the mTOR signal pathway, western bolt showed that the expressions of mTOR protein and p70S6K phosphorylation level were distinctly lower in the simvastatin-treated group in contrast to the vehicle and sham groups at 3 and 5 d (Figures 2(b) and 2(c)). Similarly, the statistical difference was not evident at postoperation day 7 (Figures 2(b) and 2(c), $p > 0.05$ compared with the vehicle group).

3.3. Expression of BDNF and GDNF Is Upregulated by Simvastatin after SCI. The spinal cord tissues were obtained from the rats at 3, 5, and 7 d after SCI for the western blot to detect the expression of BDNF and GDNF (Figure 3(a)). The consequences revealed that simvastatin treatment significantly improved the expression levels of BDNF and GDNF after

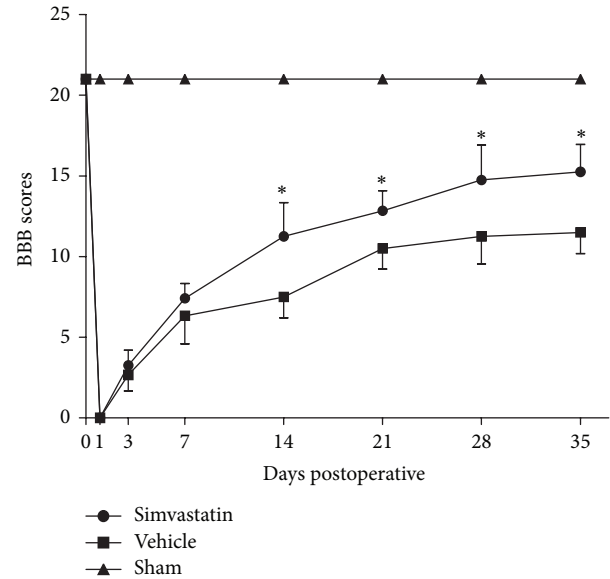


FIGURE 1: The BBB scores was evaluated at 0, 1, 3, 7, 14, 21, 28, and 35 d severally for observing the recovery situation of motor functional after SCI. Data are means \pm SD of 6 rats for each group. (* $p < 0.05$ compared with vehicle group).

injury. By contrast, the two neurotrophic factors were weak in the vehicle and sham groups at the same time (Figures 3(b) and 3(c): $p < 0.05$ compared with the vehicle group; $p < 0.01$ compared with the sham group).

3.4. Simvastatin Decreases the Expression of CSPG Protein. Immunofluorescence assay was performed to observe the CSPG expression level at 1 week after SCI (Figure 4(a)). Figure 4(b) shows that compared with the vehicle group, the relative staining intensity of CSPG was dramatically reduced by simvastatin after SCI.

3.5. Apoptosis Is Inhibited by Simvastatin after SCI. Immunofluorescence analysis was used to detect the staining intensity of caspase-3 at 7 d after SCI (Figure 5(a)). In comparison to the sham group, the expression level of caspase-3 was clearly upregulated after SCI. Nevertheless, simvastatin treatment evidently decreased the expression level of caspase-3 after SCI (Figure 5(b)), indicating that simvastatin treatment obviously inhibited the apoptosis after SCI.

3.6. Simvastatin Reduces the Loss of Nissl Bodies in Rats after SCI. Nissl staining showed that the quantities of Nissl bodies in the rat spinal cord were evidently reduced in the vehicle group after SCI compared with the sham group. By contrast, compared with the saline group, the injury was distinctly improved and the damaged tissue was also clearly reduced by simvastatin (Figure 6(A), (a); (B), (b); and (C), (c)). Meanwhile, the quantities of motor neurons in the anterior horns were significantly increased by simvastatin compared with the vehicle group (Figure 6(D), $p < 0.05$).

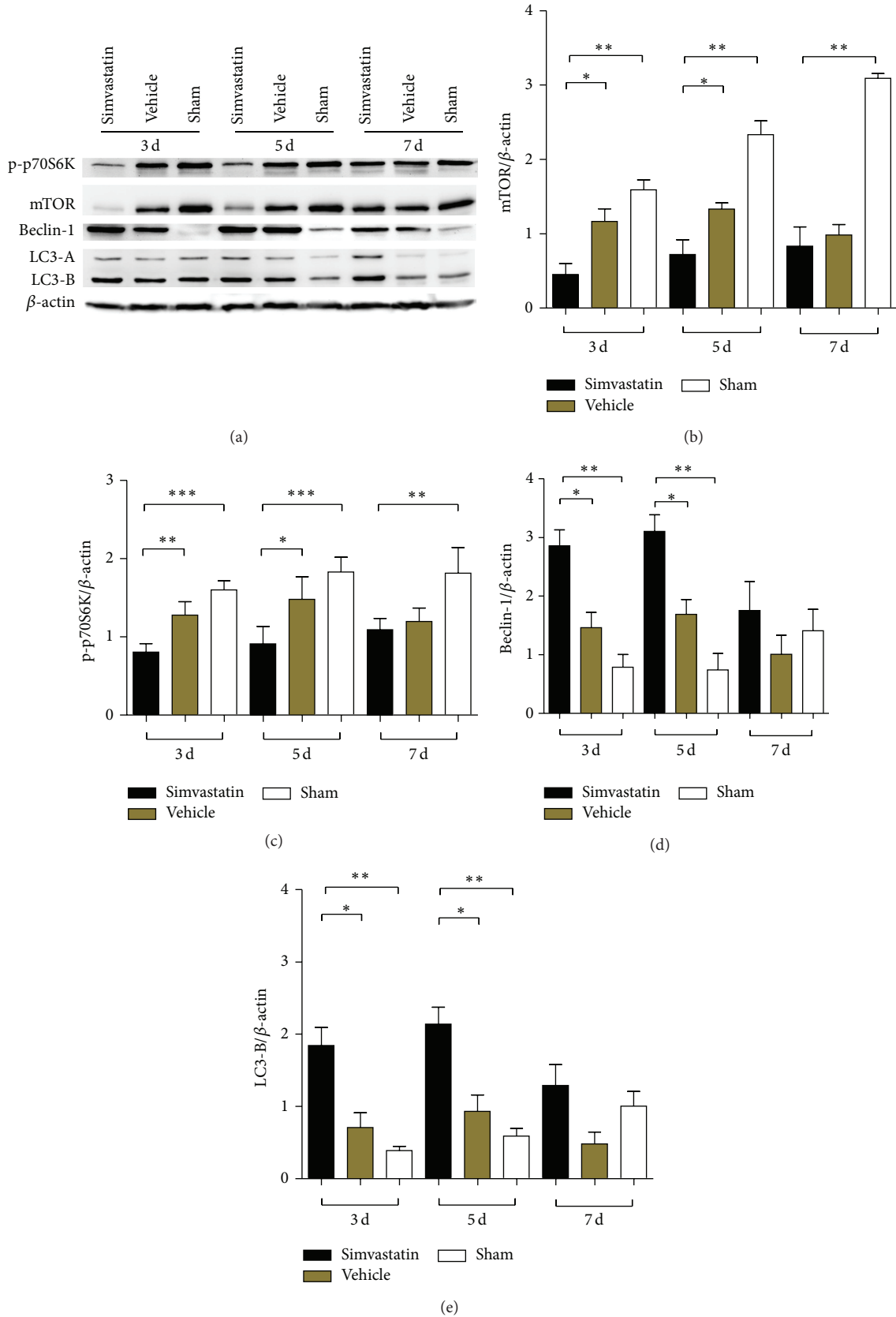


FIGURE 2: The western blot was utilized to detect the expression of mTOR, p-p70S6K, Beclin-1, and LC3-B at 3, 5, and 7 d after SCI (a). (b), (c), (d), and (e), respectively, showed the average relative gray of mTOR, p-p70S6K, Beclin-1, and LC3-B compared to the β -actin protein. Data are expressed as the mean \pm SD ($n = 4$ /group, * $p < 0.05$, ** $p < 0.01$, *** $p < 0.001$).

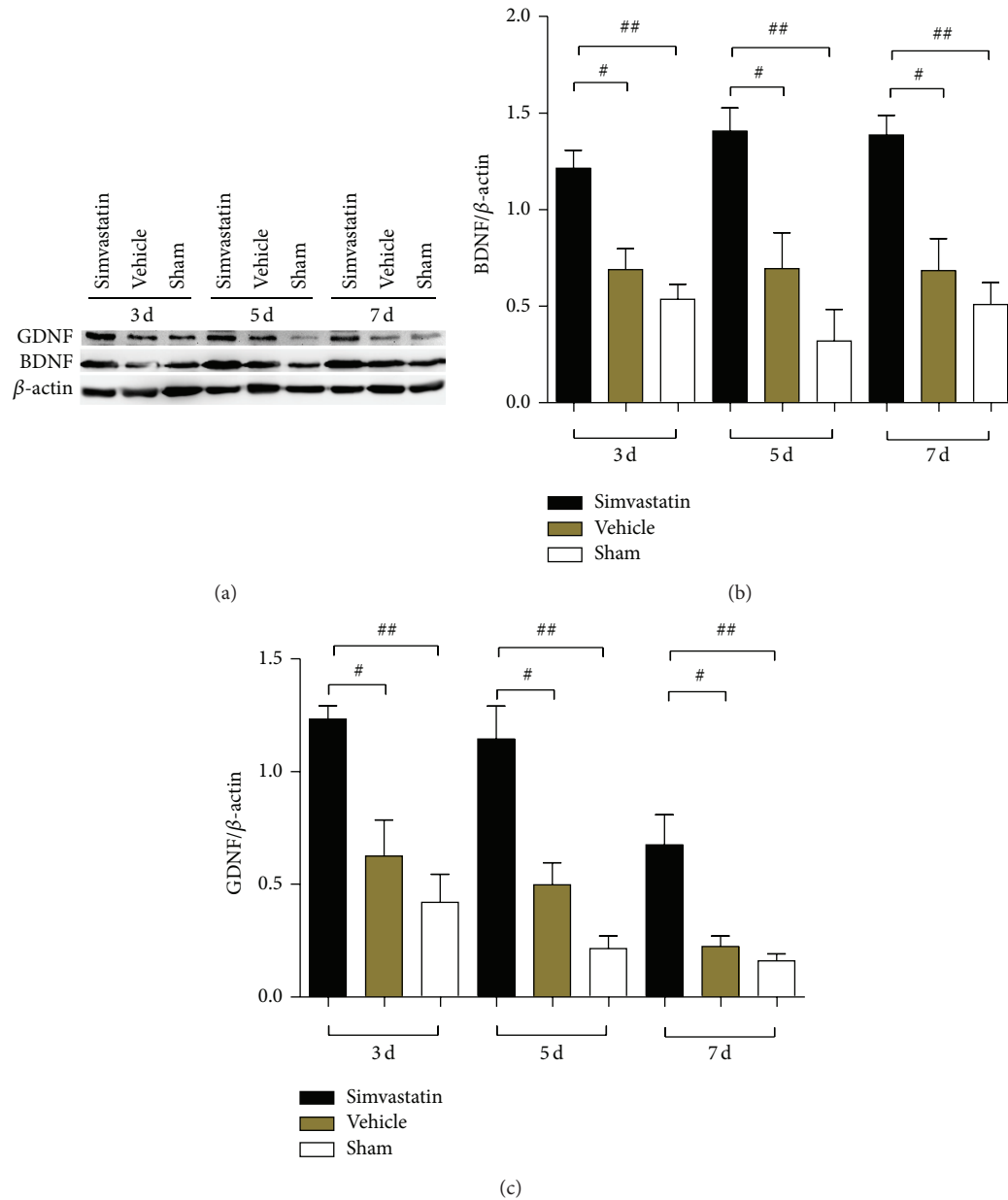


FIGURE 3: The effect of simvastatin on the BDNF and GDNF expression at 3, 5, and 7 d after SCI (a). The expression levels of BDNF and GDNF were markedly improved at 3, 5, and 7 d, respectively, in the presence of simvastatin compared with the absence of simvastatin (b) and (c). All experiments were repeated 4 times and # $p < 0.05$; ## $p < 0.01$.

4. Discussion

Statins are first-line therapeutic drugs that reduce cholesterol and prevent coronary heart disease and atherosclerosis. Recently, the multiple effects of simvastatin, including anti-inflammation and immunoregulation and, especially, the positive effects on the central nervous system, have attracted more researchers [12, 23]. Favorable effects of simvastatin on the nervous system diseases are accepted. However, according to some scholars, simvastatin failed to improve the functional recovery after SCI [24, 25]. In the present study, the optimum dose of simvastatin (10 mg/kg) was selected based on previous

reports [11, 12, 16]. In addition, the molecular mechanism of simvastatin regulating autophagy after SCI was initially observed in this study. The study may further sustain the views that simvastatin has an underlying neuroprotective effect and may promote the progress of clinical research of simvastatin for treating SCI.

Over the past few years, autophagy has played an important role in the process of motor functional recovery after SCI [26, 27]. Autophagy has a significant effect in many neurodegenerative diseases as well as in traumatic and ischemic brain injuries [28]. Meanwhile, the mTOR signaling pathway plays a significant role in activating autophagy.

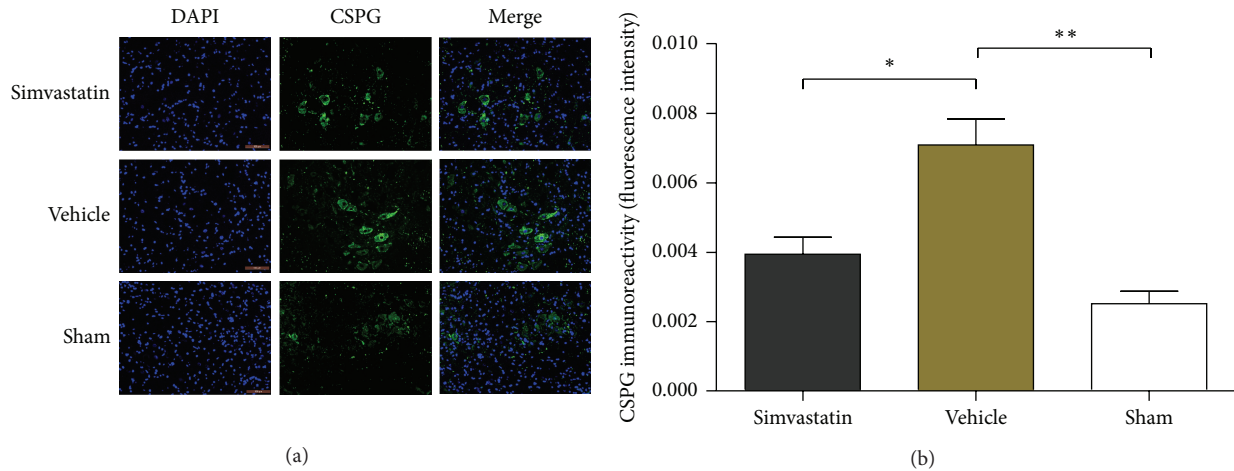


FIGURE 4: The immunoreactivity of CSPG by the immunofluorescence analysis in the three groups (a); the expression of CSPG protein in the presence of simvastatin compared to the vehicle treatment (b). Data are means \pm SD ($n = 4/\text{group}$, * $p < 0.05$, ** $p < 0.01$).

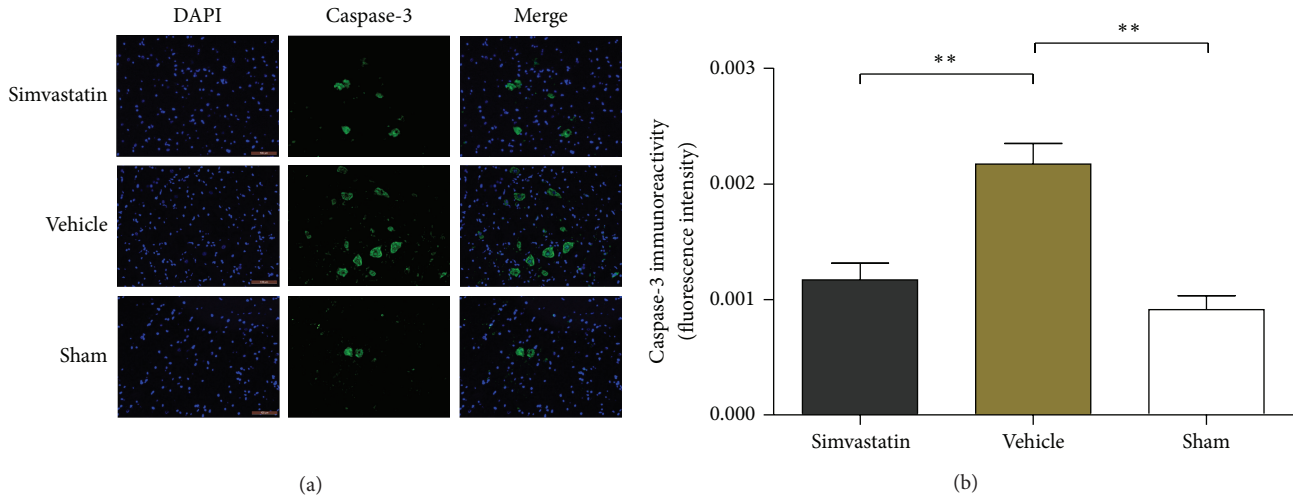


FIGURE 5: The condition of apoptosis was reflected by the expression level of caspase-3 in the three groups (a); the expression of caspase-3 in the rats with the different treatment after SCI (b). Data are means \pm SD ($n = 4/\text{group}$; scale bar: $100 \mu\text{m}$, ** $p < 0.01$).

Other reports also demonstrated that the mTOR signaling pathway has a significant function in neurodegenerative diseases, such as Alzheimer's disease, Parkinson's disease, Huntington's disease, and SCI [29, 30].

Previous studies considered that autophagy is strengthened via inhibiting the mTOR signaling pathway in coronary arterial myocytes and colchicine-induced muscle toxicity with simvastatin treatment [6, 11, 31]. However, no relevant reports exist about the effect of simvastatin on autophagy after SCI. In the present study, western blot results exhibited that the expression levels of Beclin-1 and LC3-B proteins were significantly increased at 3 and 5 d by simvastatin after SCI. By contrast, the p70S6K phosphorylation level (the downstream effector of mTOR signaling) [29, 32] and the mTOR protein level were significantly inhibited by simvastatin. Results revealed that autophagy was significantly activated by inhibiting the mTOR signaling pathway after SCI with simvastatin treatment, consistent with the effect

of simvastatin on autophagy in other diseases and reports [11, 33, 34]. Interestingly, our results also demonstrated that the alteration of Beclin-1, LC3-B, mTOR, and p-p70S6K expression level was not statistically significant at 7 d in the simvastatin-treated group compared with the vehicle-treated group after SCI. Therefore, a novel hypothesis was proposed that autophagy is likely to be evidently influenced by simvastatin in the acute phase of SCI. Thus, the role of simvastatin in autophagy in the different phases of SCI needs further study.

The inhibition of axon regeneration generates unfavorable recovery environment for neurological function and restricts the functional rehabilitation after injury in the central nervous system. Some researchers reported that CSPG occupies a consequential restrictive effect on axonal growth and regeneration [14, 35]. In addition, numerous studies also show that the neurotrophic factors BDNF and GDNF play important roles in neuronal survival process, improving the

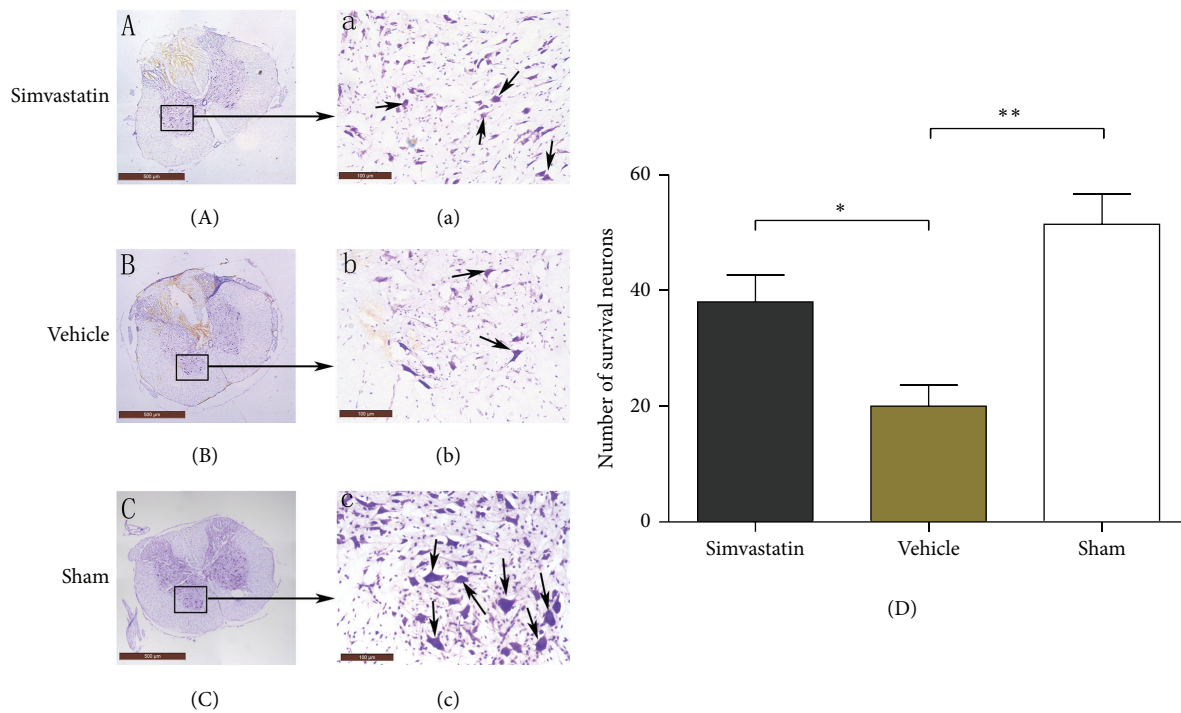


FIGURE 6: Survival of neurons in the spinal cord at postoperative week 1 was shown by Nissl staining (A–D). (Scale bar: (A), (B), and (C), 500 μm; (a), (b), and (c), 100 μm; $n = 5/\text{group}$, * $p < 0.05$, ** $p < 0.01$).

remyelination of injured axons and neuronal regeneration after SCI [36–38]. In the current study, the influence of simvastatin on the expression of CSPG, BDNF, and GDNF was assessed using immunofluorescence and western blot analysis. The results demonstrated that simvastatin treatment had the potential for neurological functional recovery after SCI.

Increasing evidence has shown that apoptosis plays a critical role in the diseases of nervous system, such as Alzheimer's disease and SCI [39]. The presence of apoptosis imposes restrictions on the neural functional recovery. The low expression of caspase-3 protein, a critical regulator of apoptosis, indicates that the activity of apoptosis is inhibited, which plays a neuroprotective role in the central nervous system [40]. In present study, the immunofluorescence results revealed that simvastatin apparently downregulated the expression of caspase-3. This downregulation of expression implies that apoptosis was inhibited and neurological function may be ameliorated by simvastatin.

To further confirm our hypothesis that simvastatin could improve neurological function, we used Nissl staining and BBB scores to observe the functional rehabilitation of motor neurons in different groups. The vehicle group showed that the quantity and function of motor neurons were visibly improved by simvastatin. The study results validated our hypothesis that simvastatin exhibits neuroprotection on SCI. Significantly, in our current study, the neuroprotective effect of simvastatin has been further verified on SCI, which is consistent with other reports [12, 13, 16]. Furthermore, a novel molecular mechanism of neuroprotection of simvastatin may have also been discovered after SCI and the significant results

may provide a potential of clinical application of simvastatin for treating SCI.

5. Conclusions

Simvastatin induced autophagy by inhibiting the mTOR signaling pathway and had the potential for neuroprotection after SCI. However, further verification on the comprehensive effects and molecule mechanism of simvastatin on animals and various nerve cells after injury is necessary.

Conflict of Interests

The authors declare that there is no conflict of interests regarding the publication of this paper.

Acknowledgments

This work was supported by the National Natural Science Foundation of China (NSFC) (nos. 81171799 and 81471854). The authors thank the other researchers for the valuable technical assistance in this work.

References

- [1] M. Wyndaele and J.-J. Wyndaele, "Incidence, prevalence and epidemiology of spinal cord injury: what learns a worldwide literature survey?" *Spinal Cord*, vol. 44, no. 9, pp. 523–529, 2006.
- [2] M.-A. Déry, G. Rousseau, M. Benderdour, and E. Beaumont, "Atorvastatin prevents early apoptosis after thoracic spinal

- cord contusion injury and promotes locomotion recovery," *Neuroscience Letters*, vol. 453, no. 1, pp. 73–76, 2009.
- [3] M. Hayashi, T. Ueyama, K. Nemoto, T. Tamaki, and E. Senba, "Sequential mRNA expression for immediate early genes, cytokines, and neurotrophins in spinal cord injury," *Journal of Neurotrauma*, vol. 17, no. 3, pp. 203–218, 2000.
 - [4] J.-J. Chen, F. Lin, and Z.-H. Qin, "The roles of the proteasome pathway in signal transduction and neurodegenerative diseases," *Neuroscience Bulletin*, vol. 24, no. 3, pp. 183–194, 2008.
 - [5] M. Komatsu, S. Waguri, T. Chiba et al., "Loss of autophagy in the central nervous system causes neurodegeneration in mice," *Nature*, vol. 441, no. 7095, pp. 880–884, 2006.
 - [6] J. K. Ching, J. S. Ju, S. K. Pittman, M. Margeta, and C. C. Weihl, "Increased autophagy accelerates colchicine-induced muscle toxicity," *Autophagy*, vol. 9, no. 12, pp. 2115–2125, 2013.
 - [7] P. J. Millar and J. S. Floras, "Statins and the autonomic nervous system," *Clinical Science*, vol. 126, no. 5, pp. 401–415, 2014.
 - [8] M. A. Maggard, B. Ke, T. Wang et al., "Effects of pravastatin on chronic rejection of rat cardiac allografts," *Transplantation*, vol. 65, no. 2, pp. 149–155, 1998.
 - [9] O. Stüve, S. Youssef, L. Steinman, and S. S. Zamvil, "Statins as potential therapeutic agents in neuroinflammatory disorders," *Current Opinion in Neurology*, vol. 16, no. 3, pp. 393–401, 2003.
 - [10] M. Crisby, "Modulation of the inflammatory process by statins," *Timely Topics in Medicine. Cardiovascular Diseases*, vol. 9, article E3, 2005.
 - [11] Y.-M. Wei, X. Li, M. Xu et al., "Enhancement of autophagy by simvastatin through inhibition of Rac1-mTOR signaling pathway in coronary arterial myocytes," *Cellular Physiology and Biochemistry*, vol. 31, no. 6, pp. 925–937, 2013.
 - [12] E. Esposito, B. Rinaldi, E. Mazzone et al., "Anti-inflammatory effect of simvastatin in an experimental model of spinal cord trauma: Involvement of PPAR- α ," *Journal of Neuroinflammation*, vol. 9, article 81, 2012.
 - [13] X. Han, N. Yang, Y. Xu et al., "Simvastatin treatment improves functional recovery after experimental spinal cord injury by upregulating the expression of BDNF and GDNF," *Neuroscience Letters*, vol. 487, no. 3, pp. 255–259, 2011.
 - [14] E. Holmberg, S.-X. Zhang, P. D. Sarmiere, B. R. Kluge, J. T. White, and S. Doolen, "Statins decrease chondroitin sulfate proteoglycan expression and acute astrocyte activation in central nervous system injury," *Experimental Neurology*, vol. 214, no. 1, pp. 78–86, 2008.
 - [15] A. Yacoub, M. C. Hajec, R. Stanger, W. Wan, H. Young, and B. E. Mathern, "Neuroprotective effects of perflurocarbon (oxycyte) after contusive spinal cord injury," *Journal of Neurotrauma*, vol. 31, no. 3, pp. 256–267, 2014.
 - [16] T. Saito, M. Tsuchida, S. Umehara, T. Kohno, H. Yamamoto, and J.-I. Hayashi, "Reduction of spinal cord ischemia/reperfusion injury with simvastatin in rats," *Anesthesia and Analgesia*, vol. 113, no. 3, pp. 565–571, 2011.
 - [17] X. Q. Shi, T. K. Y. Lim, S. Lee, Y. Q. Zhao, and J. Zhang, "Statins alleviate experimental nerve injury-induced neuropathic pain," *Pain*, vol. 152, no. 5, pp. 1033–1043, 2011.
 - [18] D. M. Basso, M. S. Beattie, and J. C. Bresnahan, "A sensitive and reliable locomotor rating scale for open field testing in rats," *Journal of Neurotrauma*, vol. 12, no. 1, pp. 1–21, 1995.
 - [19] Y. Kabeya, N. Mizushima, T. Ueno et al., "LC3, a mammalian homologue of yeast Apg8p, is localized in autophagosomal membranes after processing," *The EMBO Journal*, vol. 19, no. 21, pp. 5720–5728, 2000.
 - [20] Y. Lai, R. W. Hickey, Y. Chen et al., "Autophagy is increased after traumatic brain injury in mice and is partially inhibited by the antioxidant γ -glutamylcysteinyl ethyl ester," *Journal of Cerebral Blood Flow and Metabolism*, vol. 28, no. 3, pp. 540–550, 2008.
 - [21] H.-C. Chen, T.-H. Fong, A.-W. Lee, and W.-T. Chiu, "Autophagy is activated in injured neurons and inhibited by methylprednisolone after experimental spinal cord injury," *Spine*, vol. 37, no. 6, pp. 470–475, 2012.
 - [22] B. Levine and G. Kroemer, "Autophagy in the pathogenesis of disease," *Cell*, vol. 132, no. 1, pp. 27–42, 2008.
 - [23] E. Holmberg, T. Nordstrom, M. Gross, B. Kluge, S.-X. Zhang, and S. Doolen, "Simvastatin promotes neurite outgrowth in the presence of inhibitory molecules found in central nervous system injury," *Journal of Neurotrauma*, vol. 23, no. 9, pp. 1366–1378, 2006.
 - [24] J. H. T. Lee, S. Tigchelaar, J. Liu et al., "Lack of neuroprotective effects of simvastatin and minocycline in a model of cervical spinal cord injury," *Experimental Neurology*, vol. 225, no. 1, pp. 219–230, 2010.
 - [25] C. M. Mann, J. H. T. Lee, J. Hillyer, A. M. T. Stammers, W. Tetzlaff, and B. K. Kwon, "Lack of robust neurologic benefits with simvastatin or atorvastatin treatment after acute thoracic spinal cord contusion injury," *Experimental Neurology*, vol. 221, no. 2, pp. 285–295, 2010.
 - [26] S. Park, S.-K. Lee, K. Park et al., "Beneficial effects of endogenous and exogenous melatonin on neural reconstruction and functional recovery in an animal model of spinal cord injury," *Journal of Pineal Research*, vol. 52, no. 1, pp. 107–119, 2012.
 - [27] P. Tang, H. Hou, L. Zhang et al., "Autophagy reduces neuronal damage and promotes locomotor recovery via inhibition of apoptosis after spinal cord injury in rats," *Molecular Neurobiology*, vol. 49, no. 1, pp. 276–287, 2014.
 - [28] S. Erlich, A. Alexandrovich, E. Shohami, and R. Pinkas-Kramarski, "Rapamycin is a neuroprotective treatment for traumatic brain injury," *Neurobiology of Disease*, vol. 26, no. 1, pp. 86–93, 2007.
 - [29] H.-C. Chen, T.-H. Fong, P.-W. Hsu, and W.-T. Chiu, "Multifaceted effects of rapamycin on functional recovery after spinal cord injury in rats through autophagy promotion, anti-inflammation, and neuroprotection," *The Journal of Surgical Research*, vol. 179, no. 1, pp. E203–E210, 2013.
 - [30] E. Santini, M. Heiman, P. Greengard, E. Valjent, and G. Fisone, "Inhibition of mTOR signaling in parkinson's disease prevents L-DOPA-induced dyskinesia," *Science Signaling*, vol. 2, no. 80, article ra36, 2009.
 - [31] P.-M. Yang, Y.-L. Liu, Y.-C. Lin, C.-T. Shun, M.-S. Wu, and C.-C. Chen, "Inhibition of autophagy enhances anticancer effects of atorvastatin in digestive malignancies," *Cancer Research*, vol. 70, no. 19, pp. 7699–7709, 2010.
 - [32] A. Sekiguchi, H. Kanno, H. Ozawa, S. Yamaya, and E. Itoi, "Rapamycin promotes autophagy and reduces neural tissue damage and locomotor impairment after spinal cord injury in mice," *Journal of Neurotrauma*, vol. 29, no. 5, pp. 946–956, 2012.
 - [33] A. M. Andres, G. Hernandez, P. Lee et al., "Mitophagy is required for acute cardioprotection by simvastatin," *Antioxidants & Redox Signaling*, vol. 21, no. 14, pp. 1960–1973, 2014.
 - [34] M. Araki and K. Motojima, "Hydrophobic statins induce autophagy in cultured human rhabdomyosarcoma cells," *Biochemical and Biophysical Research Communications*, vol. 367, no. 2, pp. 462–467, 2008.
 - [35] S. J. A. Davies, M. T. Fitch, S. P. Memberg, A. K. Hall, G. Raisman, and J. Silver, "Regeneration of adult axons in white

- matter tracts of the central nervous system,” *Nature*, vol. 390, no. 6661, pp. 680–683, 1997.
- [36] B. I. Awad, M. A. Carmody, and M. P. Steinmetz, “Potential role of growth factors in the management of spinal cord injury,” *World Neurosurgery*, vol. 83, no. 1, pp. 120–131, 2015.
- [37] M. S. Ramer, “Endogenous neurotrophins and plasticity following spinal deafferentation,” *Experimental Neurology*, vol. 235, no. 1, pp. 70–77, 2012.
- [38] M. Yaguchi, S. Ohta, Y. Toyama, Y. Kawakami, and M. Toda, “Functional recovery after spinal cord injury in mice through activation of microglia and dendritic cells after IL-12 administration,” *Journal of Neuroscience Research*, vol. 86, no. 9, pp. 1972–1980, 2008.
- [39] J. Yuan and B. A. Yankner, “Apoptosis in the nervous system,” *Nature*, vol. 407, no. 6805, pp. 802–809, 2000.
- [40] M. Li, V. O. Ona, C. Guegan et al., “Functional role of caspase-1 and caspase-3 in an ALS transgenic mouse model,” *Science*, vol. 288, pp. 335–339, 2000.

Research Article

A Pyrene@Micelle Sensor for Fluorescent Oxygen Sensing

Yan-xia Yuan, Hong-shang Peng, Jian-tao Ping, Xiao-hui Wang, and Fang-tian You

Key Laboratory of Luminescence and Optical Information, Ministry of Education, Institute of Optoelectronic Technology, Beijing Jiaotong University, Beijing 100044, China

Correspondence should be addressed to Hong-shang Peng; hshpeng@bjtu.edu.cn

Received 9 March 2015; Accepted 28 April 2015

Academic Editor: Xuanjun Zhang

Copyright © 2015 Yan-xia Yuan et al. This is an open access article distributed under the Creative Commons Attribution License, which permits unrestricted use, distribution, and reproduction in any medium, provided the original work is properly cited.

For most fluorescent oxygen sensors developed today, their fabrication process is either time-consuming or needs specialized knowledge. In this work, a robust fluorescent oxygen sensor is facilely constructed by dissolving pyrene molecules into CTAB aqueous solution. The as-prepared pyrene@micelle sensors have submicron-sized diameter, and the concentration of utilized pyrene can be reduced as low as 0.8 mM but still can exhibit dominant excimer emission. The excimer fluorescence is sensitive to dissolved oxygen in both intensity and lifetime, and the respective Stern-Volmer plot follows a nonlinear behavior justified by a two-site model. Because of the merits of large Stokes shift (~140 nm), easy fabrication, and robustness, the pyrene@micelle sensors are very attractive for practical determination of oxygen.

1. Introduction

Determination of oxygen concentration is important for a number of applications ranging from clinical analysis to environment monitoring [1, 2]. Among the various sensing methods, fluorescence-based techniques have attracted considerable interest because they can be noninvasive and sensitive and work in even strong electromagnetic fields [3, 4]. These fluorescent oxygen sensors usually were constructed by incorporating probe dyes into an inert matrix, taking the form of strip [5], film [6], and nanoparticles [7–9]. Since the probe dyes are trapped by solid matrix, their collision probability with oxygen molecules (e.g., fluorescence quenching) is reduced to some extent, and oxygen sensitivity is undermined accordingly. As an alternative, oxygen sensors based on free probed dyes should have higher sensitivity.

Pyrene is an aromatic, polycyclic hydrocarbon with planer structure, which is widely used as fluorescent chemosensor because of the characteristic photophysical properties such as high quantum yield, long singlet lifetime, and environment-sensitive fluorescence. In terms of oxygen sensing, the long lifetime enhances the chance of pyrene molecules in excited states to collide with oxygen molecules and renders oxygen-sensitive fluorescence. Particularly, pyrene molecules can form excimer at higher molar concentrations, which

give rise to longer-wavelength emission (at ~480 nm) than that of pyrene monomer (370–430 nm), that is, large Stokes shift. The above merits make pyrene and its derivatives very attractive oxygen probes. Pyrene and/or pyrene derivatives have been reported to detect oxygen after being incorporated into polymer matrix [10–12] or dissolved in solution [13]. It is noticed that, however, high concentration of pyrene molecules usually is needed in those oxygen sensors, with the aim of forming excimers. For example, 2 mM pyrene was adopted in toluene-based oxygen sensing [12, 13], and the concentration was further raised up to 10 mM in polymer-based sensors that the solid matrix precluded the free diffusion of probe dyes [11, 12].

With the recent progress of nanotechnology, novel pyrene-based oxygen sensors with high sensitivity have been developed, wherein pyrene derivatives are either chemisorbed onto nanoporous aluminium plate [14–16] or attached to quantum dots [17, 18]. Although the concentration of utilized probe dyes is greatly reduced, the synthesis of pyrene derivatives and related nanomaterials is not easy for nonchemists and is time-consuming. It is known that pyrene molecules can form excimers in micelles of nonionic detergents [19]. Such a self-assembly approach is commonly used to load dyes into biologically based nanocarriers [20, 21]. Different from solid polymers, the dissolved pyrene

molecules can move freely inside micelles, and, on the other hand, oxygen molecules diffuse more efficiently to and fro the submicron-sized micelles. Those merits inspire us to adopt micelle to host pyrene molecules, so as to facilitate construct a fluorescent oxygen sensor.

In this work, pyrene molecules are directly dissolved into hexadecyltrimethylammonium bromide (CTAB) micelle (pyrene@micelle) to build fluorescent oxygen sensors. The resultant pyrene@micelle sensors have nanosized dimension with dominant excimer emission. Their oxygen-sensitive fluorescence is investigated in terms of both intensity and lifetime, and respective calibration line is plotted. The merits of large Stokes shift, easy fabrication, and good oxygen sensitivity make the pyrene@micelle sensors very attractive for fluorescent oxygen sensing.

2. Material and Methods

2.1. Materials. Pyrene (98%) was procured from Sigma Aldrich. Cetyltrimethylammonium bromide (CTAB, 99%) and absolute ethyl alcohol (99.7%) were procured from Beijing Lanyi Chemical Corporation (Beijing, China). All reagents were commercially available and used as received without further purification. High-purity deionized water (18.25 M Ω -cm) was produced using Aquapro EDI2-3002-U ultrapurified water system (<http://www.aicwater.com.cn/>).

2.2. Preparation of Pyrene@Micelle Oxygen Sensor. To 3 mL CTAB water solution (20 mM), different amounts of pyrene ethanol solution (5000 ppm) were added to result in pyrene@micelle with a concentration of 0.02, 0.06, 0.2, 0.4, 0.6, and 0.8 mM, respectively. The mixing took place under sonication for 20 minutes at 25°C and then was left still for 2 hours before further characterization including hydrodynamic size measurement and oxygen sensitivity test.

2.3. Characterization. Hydrodynamic size of pyrene@micelle aqueous dispersion was determined by dynamic light scattering (DSL), using a Zetasizer Nano instrument (Malvern Instruments, Malvern, UK). Steady-state fluorescence spectra were recorded on a LS55 fluorescence spectrophotometer (PerkinElmer). The fluorescence decay curves were measured by a time-correlated single-photon counting system (TCSPC), Fluorocube-01-NL (HORIBA Scientific), and the sample was excited by a pulsed ultraviolet light-emitting diode (373 nm, Nichia NSHU590E). The sample was placed in a 1 cm quartz cuvette and all the characterizations were performed at 25°C.

2.4. Pyrene@Micelle Calibration and Experimental Setup. The calibration was carried out in a cuvette filled with 2 mL of pyrene@micelle aqueous dispersion (0.8 mM), which was put inside a sealed plastic bag (vol. = 80 L) with an inlet and outlet. The plastic bag was vacuumed firstly before each operation and then inflated with an O₂ (99.6%)/N₂ (99.6%) gas mixture with various ratios, provided by a WITT gas mixer (type KM60-2, <http://www.wittgas.com/>, Germany), in the range of 1–25% with an accuracy of 1% absolute. In addition, 50%

O₂/N₂ mixture, pure O₂ and N₂ were provided. Different dissolved oxygen (DO) concentrations were obtained by aerating the sample solution with the gas mixture for 3 h. All spectra measurements were performed at 25°C. The DO concentrations in pyrene@micelle dispersion were deduced according to that in oxygen-saturated solutions (43 ppm) based on the solubility equation of oxygen in water.

3. Results and Discussion

3.1. Synthesis and Characterization of Pyrene@Micelle Sensors. Initially, the CTAB micelle solution was turbid with the addition of pyrene and then became transparent again after being ultrasonicated for 20 minutes, with slightly opalescent color. Such a solubility transition indicates that pyrene molecules are completely dissolved in CTAB micelles; that is, pyrene@micelle is formed. It is important to note that the pyrene@micelle sensors are very robust as they can be recovered from turbid state after longtime storage simply by ultrasonication.

In order to construct pyrene@micelle oxygen sensors, different amounts of pyrene were dissolved into CTAB micelles in order to render dominant excimer emission. Figure 1(a) shows emission spectra of the resultant pyrene@micelle at different concentrations. The well-defined emission at 370–430 nm is attributed to pyrene monomer, and the broad band emission peaked at ~474 nm to pyrene excimer. Basically, with the increase of pyrene concentration, the excimer emission of pyrene@micelle is gradually enhanced at the expense of monomer emission. But it needs to point out that the monomer emission increases concomitantly with the excimer at low concentrations (e.g., 0.02–0.06 mM). The reason may be that the increased quantity of pyrene molecules is much bigger than that consumed through formation of excimer. Such a transition from monomer to excimer in pyrene@micelle can be clearly observed by the concentration-dependent fluorescence, as displayed in Figure 1(b). It can be seen from the figure that in pyrene@micelle the excimer emission is dominant over monomer when the concentration is higher than 0.3 mM. With the consideration that too much ethanol introduced by pyrene solution may influence the stability of CTAB micelle, 0.8 mM pyrene was adopted to build pyrene@micelle sensor in this work.

Hydrodynamic size of CTAB micelles before and after addition of pyrene is characterized by a Zetasizer analyzer, as shown in Figure 2. The size is determined to be around 386 nm and 348 nm, respectively. Apparently, the size of CTAB micelles is decreased, instead of increasing, after encapsulation of pyrene. This abnormal phenomenon is attributed to the influence of introduced ethanol, which increases the CMC in mixed solution [22].

3.2. Oxygen Sensitivity and Calibration of Pyrene@Micelle Sensors. Pyrene@micelle solution was equilibrated with a gas mixture with various O₂/N₂ ratios, and their oxygen sensitivity was firstly tested on the basis of steady-state fluorescence. Figure 3(a) shows the response of the emission

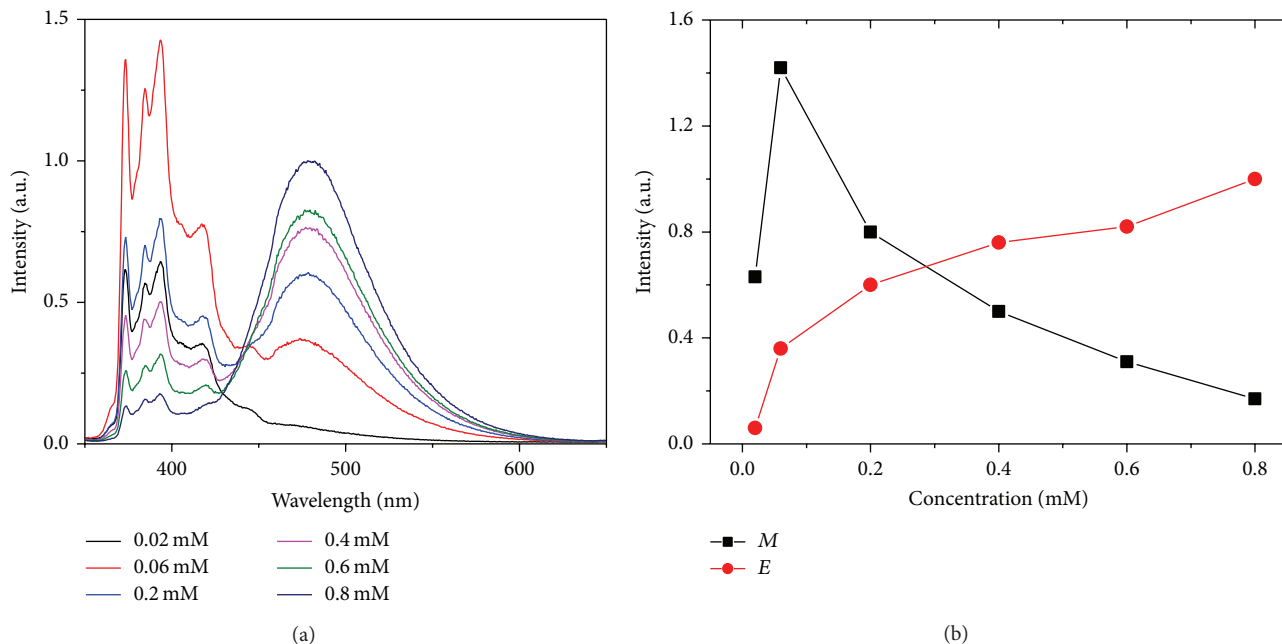


FIGURE 1: (a) Emission spectra ($\lambda_{ex} = 337$ nm) of pyrene@micelle solution with different concentrations of pyrene (0.02–0.8 mM). (b) Concentration-dependent fluorescent intensity of pyrene monomer ($\lambda_{em} = 393$ nm, the highest peak in monomer emission labeled as M) and excimer ($\lambda_{em} = 474$ nm, labeled as E). Data are calculated from (a).

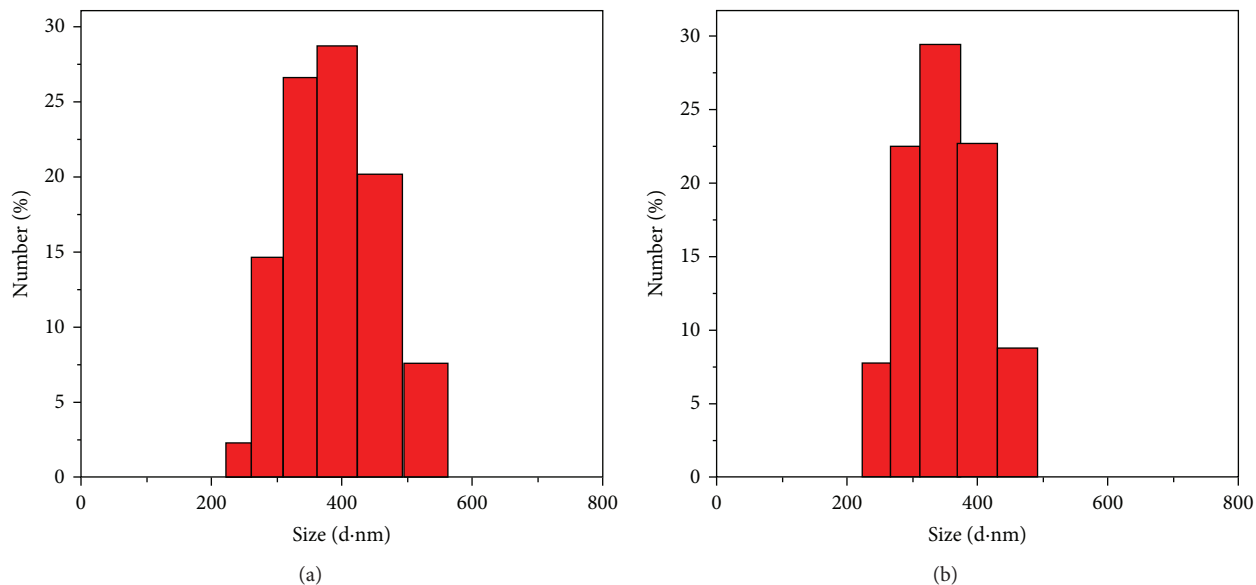


FIGURE 2: Hydrodynamic size of the CTAB micelles before (a) and after (b) addition of pyrene solution (measured at 25°C).

spectra towards dissolved oxygen (DO) under 337 nm excitation. From the top to the bottom lines, the DO concentrations are 0.0 (nitrogen saturated), 2.21, 4.43, 6.64, 9.3, 11.07, 22.15, and 44.3 ppm (oxygen-saturated) in sequence. It can be seen clearly that the monomer and excimer emission of pyrene@micelle are both sensitive to oxygen. By defining R as the emission intensity, the sensitivity of the sensor can

be expressed by the overall quenching response to dissolved oxygen [23],

$$Q = \frac{(R_{N_2} - R_{O_2})}{R_{N_2}}, \tag{1}$$

where R_{N_2} and R_{O_2} represent the emission intensity of the sensor in fully deoxygenated and fully oxygenated solutions,

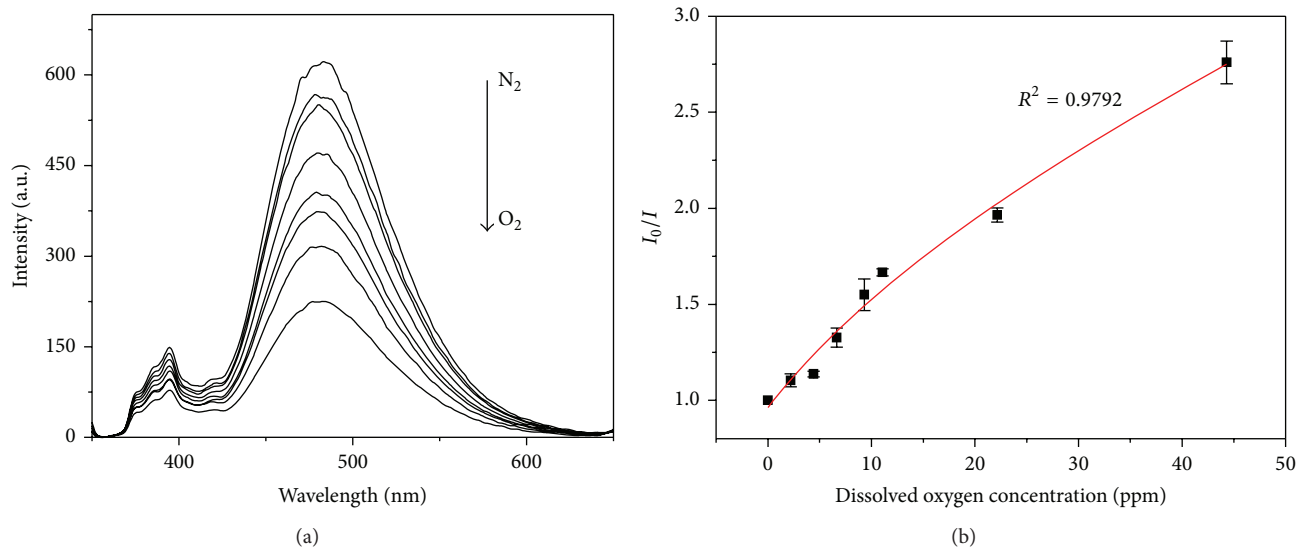


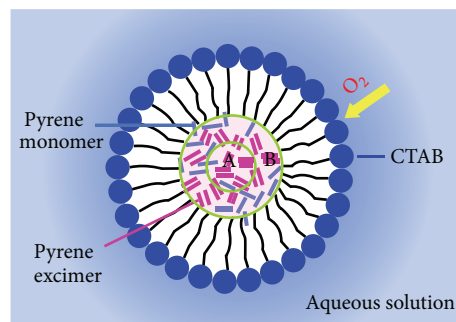
FIGURE 3: Oxygen sensitivity of pyrene@micelle solution (0.8 mM): (a) emission spectra at 337 nm excitation at various oxygen concentrations; (b) Stern-Volmer plot of fluorescence intensity of pyrene excimer. The experiment data were calculated from (a).

respectively. The as-obtained value of Q of monomer and excimer is around 47% and 65%, respectively. Apparently, the excimer emission is more sensitive to oxygen than monomer emission. It is necessary to note that oxygen sensitivity of pyrene excimer in micelles is lower than that in silicon polymer ($Q = 92.5\%$) [12]. This reduced sensitivity might be due to the predissolved gas in CTAB micelles which weakens the fluorescence quenching by oxygen.

In previously reported pyrene- (or pyrene derivatives-) based oxygen sensors, the oxygen-quenching process can be described by either linear [12, 17, 18] or nonlinear Stern-Volmer equation [16], corresponding to homogeneous and heterogeneous microenvironments of probe dye, respectively. Figure 3(b) depicts the Stern-Volmer plot between the excimer emission intensity at 474 nm and DO concentration. It is observed that the plot follows a nonlinear behavior, which can be fitted by the following Stern-Volmer equation based on a two-site model (with a correlation coefficient of >0.979) [24–27]:

$$\frac{\tau_0}{\tau} = \frac{I_0}{I} = \left[\frac{f_1}{1 + K_{SV_1} [O_2]} + \frac{f_2}{1 + K_{SV_2} [O_2]} \right]^{-1}, \quad (2)$$

where I_0 and τ_0 are fluorescence intensity and lifetime in the absence of oxygen, I and τ are the fluorescent intensity and lifetime at a given DO concentration $[O_2]$, f_1 and f_2 are the emission fraction of the probes in different environment, and K_{SV} is the Stern-Volmer quenching constant of the different components. The line is the fitting function described by (2) and yields K_{SV_1} ($f_1 = 0.33$) and K_{SV_2} ($f_2 = 0.67$), 0.01 and 0.1, respectively. Since oxygen molecules are inwards diffused into pyrene@micelle from aqueous solution, the emissive pyrene excimers that are close to hydrophobic tail of CTAB (denoted as site B) are prone to be quenched in comparison to those in the core (site A), as illustrated in Scheme 1.



SCHEME 1: Cross-section of pyrene@micelle sensor (not to scale). The encapsulated pyrene monomers (labeled as blue bars) are free to form into excimers (pink bars), which can be approximately grouped as site A or site B according to their accessibility to oxygen.

Fluorescence intensity-based measurements usually suffer from variation of the sensor concentration and drifts of the optoelectronic system, such as lamps and detectors. In contrast, lifetime-based techniques can overcome these drawbacks and are more reliable. The excimer fluorescence decay curves of pyrene@micelle at different concentrations of DO are then measured, and a representative one is displayed in Figure 4(a). The growth part reflects the transition of pyrene molecules from excited monomer to excimer [18]. Since most of the pyrene monomers within micelles are converted into excimers under this concentration (demonstrated by the dominant excimer emission in Figure 1), the growth component is coincident with the decay kinetics of the monomer. By fitting the decay curve with a two-exponential equation,

$$I = I_0 \left[\exp\left(-\frac{t}{\tau_1}\right) - \exp\left(-\frac{t}{\tau_2}\right) \right]. \quad (3)$$

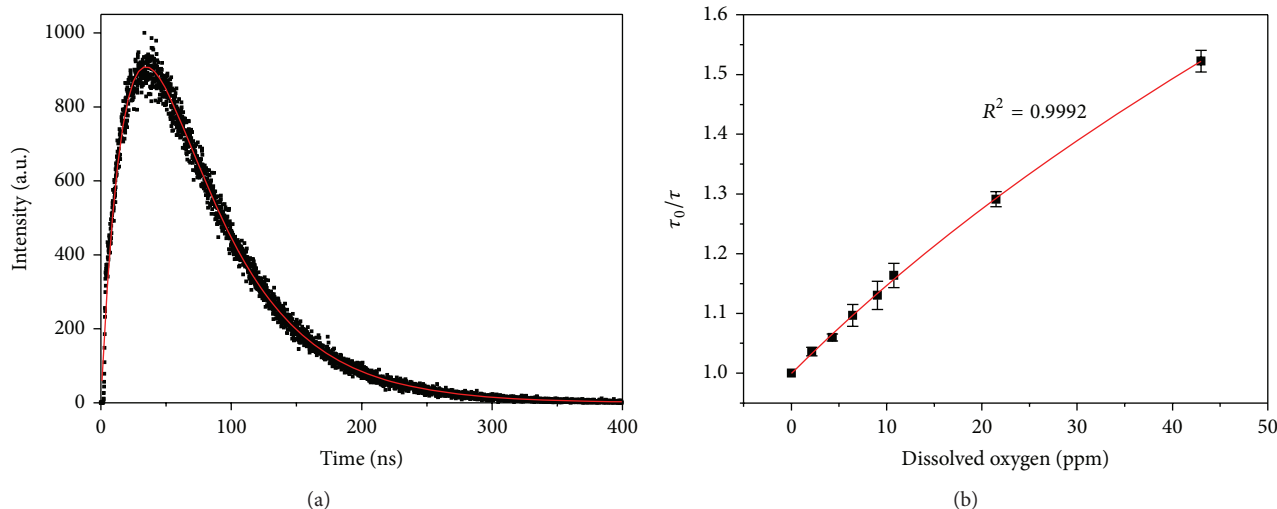


FIGURE 4: (a) A representative fluorescence decay curve of pyrene@micelle sensors monitored at 474 nm ($\lambda_{\text{ex}} = 373$ nm, at 25°C). The red line is the fitting function of (3). (b) Stern-Volmer plot of lifetime of excimer in pyrene@micelle sensors. The experiment data were acquired by fitting oxygen-sensitive decay curves.

Lifetime of pyrene excimer can be determined, that is, τ_2 , along with that of monomer, τ_1 . Figure 4(b) depicts the Stern-Volmer plot of the excimer lifetime of pyrene@micelle versus DO concentration. It can be well fitted by the nonlinear Stern-Volmer equation (2) and gives rise to K_{SV_1} ($f_1 = 0.41$) and K_{SV_2} ($f_2 = 0.59$), 0.002 and 0.02, respectively. With the consideration of quenching constants obtained from fluorescence intensity-based measurements, it can be concluded that (i) fluorescence lifetime does provide more accurate calibrating than intensity does, as revealed by the high correlation coefficient of >0.999 ; (ii) excimers in site B are distributed within a thin shell of the whole dissolved pyrenes because their proportions (f_1 and f_2) are comparable; (iii) the quenching constant of excimers in site B is ten times of that in site A, for both fluorescence intensity- and lifetime-based measurements, suggesting that reducing the diameter of micelle-typed sensors may greatly improve their oxygen sensitivity.

4. Conclusions

In summary, a micelle-typed fluorescent oxygen sensor was facilely constructed by dissolving pyrene molecules into CTAB aqueous solution. The pyrene@micelle sensors were of nanosized dimension, and low concentration of pyrene (e.g., >0.8 mM) was sufficient to render dominant excimer emission. The excimer fluorescence is sensitive to dissolved oxygen with a quenching response of 65%. Both the fluorescence intensity- and lifetime-based oxygen sensitivities were well fitted by a nonlinear Stern-Volmer equation. Based on the fitting parameters, microenvironments of pyrene excimers inside micelles were then classified as two types: one is close to CTAB molecules and easy to access by oxygen; the other is in the core of micelle and difficult to be accessed by oxygen. Therefore, it is expected that the sensitivity of micelle-typed sensors can be further improved if their size is reduced, and

related work is being carried out. Considering the simplicity, sensitivity, and robustness of the pyrene@micelle sensors, they may find applications in industrial or environmental fields.

Conflict of Interests

The authors declare that there is no conflict of interests regarding the publication of this paper.

Acknowledgments

This work was financially supported by the NSFC (Grants 61078069 and 11274038) and the NCET (12-0771).

References

- [1] G.-J. Chee, Y. Nomura, K. Ikebukuro, and I. Karube, "Optical fiber biosensor for the determination of low biochemical oxygen demand," *Biosensors and Bioelectronics*, vol. 15, no. 7-8, pp. 371-376, 2000.
- [2] M. Höckel, K. Schlenger, S. Höckel, B. Aral, U. Schäffer, and P. Vaupel, "Tumor hypoxia in pelvic recurrences of cervical cancer," *International Journal of Cancer*, vol. 79, no. 4, pp. 365-369, 1998.
- [3] X.-D. Wang and O. S. Wolfbeis, "Optical methods for sensing and imaging oxygen: materials, spectroscopies and applications," *Chemical Society Reviews*, vol. 43, no. 10, pp. 3666-3761, 2014.
- [4] D. B. Papkovsky and R. I. Dmitriev, "Biological detection by optical oxygen sensing," *Chemical Society Reviews*, vol. 42, no. 22, pp. 8700-8732, 2013.
- [5] X. Wang, X. Chen, and Z. Xie, "Reversible optical sensor strip for oxygen," *Angewandte Chemie*, vol. 120, no. 39, pp. 7560-7563, 2008.

- [6] X.-D. Wang, R. J. Meier, M. Link, and O. S. Wolfbeis, "Photographing oxygen distribution," *Angewandte Chemie International Edition*, vol. 49, no. 29, pp. 4907–4909, 2010.
- [7] X. H. Wang, H. S. Peng, L. Yang et al., *Angewandte Chemie—International Edition*, vol. 126, pp. 12679–12683, 2014.
- [8] A. V. Kondrashina, R. I. Dmitriev, S. M. Borisov et al., "A phosphorescent nanoparticle-based probe for sensing and imaging of (intra)cellular oxygen in multiple detection modalities," *Advanced Functional Materials*, vol. 22, no. 23, pp. 4931–4939, 2012.
- [9] X.-H. Wang, H.-S. Peng, H. Ding et al., "Biocompatible fluorescent core-shell nanoparticles for ratiometric oxygen sensing," *Journal of Materials Chemistry*, vol. 22, no. 31, pp. 16066–16071, 2012.
- [10] T. Ishiji and M. Kaneko, "Photoluminescence of pyrenebutyric acid incorporated into silicone film as a technique in luminescent oxygen sensing," *The Analyst*, vol. 120, no. 6, pp. 1633–1638, 1995.
- [11] W. Xu, R. Schmidt, M. Whaley et al., "Oxygen sensors based on luminescence quenching: interactions of pyrene with the polymer supports," *Analytical Chemistry*, vol. 67, no. 18, pp. 3172–3180, 1995.
- [12] B. J. Basu and K. S. Rajam, "Comparison of the oxygen sensor performance of some pyrene derivatives in silicone polymer matrix," *Sensors and Actuators, B: Chemical*, vol. 99, no. 2-3, pp. 459–467, 2004.
- [13] L. Búcsiová, P. Hrdlovič, and Š. Chmela, "Spectral characteristics of fluorescence probes based on pyrene in solution and in polymer matrix," *Journal of Photochemistry and Photobiology A: Chemistry*, vol. 143, no. 1, pp. 59–68, 2001.
- [14] Y. Fujiwara, I. Okura, T. Miyashita, and Y. Amao, "Optical oxygen sensor based on fluorescence change of pyrene-1-butyric acid chemisorption film on an anodic oxidation aluminium plate," *Analytica Chimica Acta*, vol. 471, no. 1, pp. 25–32, 2002.
- [15] Y. Fujiwara and Y. Amao, "Optical oxygen sensor based on controlling the excimer formation of pyrene-1-butylic acid chemisorption layer onto nano-porous anodic oxidized aluminium plate by myristic acid," *Sensors and Actuators, B: Chemical*, vol. 89, no. 1-2, pp. 58–61, 2003.
- [16] Y. Fujiwara and Y. Amao, "An oxygen sensor based on the fluorescence quenching of pyrene chemisorbed layer onto alumina plates," *Sensors and Actuators B: Chemical*, vol. 89, no. 1-2, pp. 187–191, 2003.
- [17] M. Amelia, A. Lavie-Cambot, N. D. McClenaghan, and A. Credi, "A ratiometric luminescent oxygen sensor based on a chemically functionalized quantum dot," *Chemical Communications*, vol. 47, no. 1, pp. 325–327, 2011.
- [18] C. E. Agudelo-Morales, R. E. Galian, and J. Pérez-Prieto, "Pyrene-functionalized nanoparticles: two independent sensors, the excimer and the monomer," *Analytical Chemistry*, vol. 84, no. 18, pp. 8083–8087, 2012.
- [19] N. J. Turro and P. L. Kuo, "Pyrene excimer formation in micelles of nonionic detergents and of water-soluble polymers," *Langmuir*, vol. 2, no. 4, pp. 438–442, 1986.
- [20] K. Liu, R. Xing, C. Chen et al., "Peptide-induced hierarchical long-range order and photocatalytic activity of porphyrin assemblies," *Angewandte Chemie*, vol. 127, no. 2, pp. 510–515, 2015.
- [21] F. Zhao, G. Shen, C. Chen et al., "Nanoengineering of stimuli-responsive protein-based biomimetic protocells as versatile drug delivery tools," *Chemistry—A European Journal*, vol. 20, no. 23, pp. 6880–6887, 2014.
- [22] W. Li, M. Zhang, J. Zhang, and Y. Han, "Self-assembly of cetyl trimethylammonium bromide in ethanol-water mixtures," *Frontiers of Chemistry in China*, vol. 1, no. 4, pp. 438–442, 2006.
- [23] X.-H. Wang, H.-S. Peng, Z. Chang et al., "Synthesis of ratiometric fluorescent nanoparticles for sensing oxygen," *Microchimica Acta*, vol. 178, no. 1-2, pp. 147–152, 2012.
- [24] J. N. Demas, B. A. Degraff, and W. Xu, "Modeling of luminescence quenching-based sensors: comparison of multisite and nonlinear gas solubility models," *Analytical Chemistry*, vol. 67, no. 8, pp. 1377–1380, 1995.
- [25] P. Hartmann and W. Trettnak, "Effects of polymer matrices on calibration functions of luminescent oxygen sensors on porphyrin ketone complexes," *Analytical Chemistry*, vol. 68, no. 15, pp. 2615–2620, 1996.
- [26] S. M. Borisov and I. Klimant, "Luminescent nanobeads for optical sensing and imaging of dissolved oxygen," *Microchimica Acta*, vol. 164, no. 1-2, pp. 7–15, 2009.
- [27] C.-S. Chu, T.-W. Sung, and Y.-L. Lo, "Enhanced optical oxygen sensing property based on Pt(II) complex and metal-coated silica nanoparticles embedded in sol-gel matrix," *Sensors and Actuators, B: Chemical*, vol. 185, pp. 287–292, 2013.